NATIONAL INSTITUTE FOR FUSION SCIENCE

Pulsed Power and High-Density Plasma and Applications

Edited by Koichi Takaki and Tetsuo Ozaki

(Received - Jan. 21, 2019)

NIFS-PROC-113

Apr. 02, 2019

Pulsed Power and High-Density Plasma and its Applications

Edited by Koichi Takaki and Tetsuo Ozaki

December 26-27, 2017
National Institute for Fusion Science
Toki, Gifu, Japan

Abstract

The papers appeared in this volume of research report have been presented at the “Symposium on Pulsed Power and High-Density Plasma and its Applications” held by National Institute for Fusion Science. They report the present status and recent progress in experimental and theoretical studies on pulsed power technology and its applications.

Keywords: pulsed power, particle beam, plasma, z-pinch, extreme ultraviolet, x-ray, high power microwave, environment, bio application, agriculture, atmospheric plasma, plasma under water.

Editor’s Preface

The collaborative research symposium on “Pulsed Power and High-Density Plasma and its Applications" was held at National Institute for Fusion Science (NIFS), Toki, on Dec. 26-27, 2017. This symposium was attended by 44 researchers and students from universities, institute and industrial companies. At the symposium, 34 research papers were presented each of them was followed by fruitful discussions. This symposium has provided an excellent environment for information exchange between the researchers and has promoted collaborations between NIFS and universities.

During the symposium, LHD site tour was given by NIFS staffs especially for this symposium. The attendees have obtained an exceptional opportunity to enjoy a close look at the LHD experimental facilities and listen to the in-depth explanations by the NIFS researchers.

I would like to express my sincere thanks to all of the symposium attendees, all of the paper authors, and the staffs of National Institute for Fusion Science.

Koichi Takaki
Iwate University

Tetsuo Ozaki
National Institute for Fusion Science

NIFS 2017 Coordinated Research (Symposium)
Project Title: Pulsed Power and High-Density Plasma and its Applications
Project ID: NIFS17KKGH029
NIFS Contact Person: Dr. Tetsuo Ozaki

List of participants

G. Imada (*Department of Information & Electronics Engineering, Niigata Institute of Technology*)
K. Kanai (*Department of Information & Electronics Engineering, Niigata Institute of Technology*)
S. Sato (*Department of Information & Electronics Engineering, Niigata Institute of Technology*)
K. Takaki (*Iwate University*)
K. Takahashi (*Iwate University*)
Y. Hasegawa (*Iwate University*)
S. Kobayashi (*Iwate University*)
A. Tokuchi (Pulsed Power Japan Lab.)
K. Takayama (*High Energy Accelerator Research Laboratory*)
Taufik (*The Graduate University of Advanced Studies)*
K. Okamura (*High Energy Accelerator Research Laboratory*)
D. Kumamoto (*Nagaoka University of Technology*)
J. Hasegawa (*Institute of Innovative Research, Tokyo Institute of Technology*)
E. Hotta (*Institute of Innovative Research, Tokyo Institute of Technology*)
K. Horioka (*Institute of Innovative Research, Tokyo Institute of Technology*)
T. Itagaki (*Institute of Innovative Research, Tokyo Institute of Technology*)
M. Tsukamoto (*Department of Mechanical Engineering, Tokyo Institute of Technology*)
K. Hashimoto (*Institute of Innovative Research, Tokyo Institute of Technology*)
M. Nishio (*Anan College, National Institute of Technology*)
W. Jiang *(Nagaoka University of Technology*)
T. Sugai *(Nagaoka University of Technology*)
K. Nagao *(Nagaoka University of Technology*)
T. Todoroki *(Nagaoka University of Technology*)
Y. Okada *(Nagaoka University of Technology*)
K. Yahata *(Nagaoka University of Technology*)
T. Rwahila *(Nagaoka University of Technology*)
T. Kikuchi *(Nagaoka University of Technology*)
T. Sasaki *(Nagaoka University of Technology*)
T. Takezaki *(Nagaoka University of Technology*)
S. Kusano *(Nagaoka University of Technology*)
Md. Shahed-Uz-Zaman *(Nagaoka University of Technology*)
N. Takeshita *(Nagaoka University of Technology*)
R. Matsuda *(Nagaoka University of Technology*)
K. Takasugi (*Institute of Quantum Science, Nihon University*)
T. Kawamura (*Department of Physics, School of Science, Tokyo Institute of Technology*)
T. Okui (*Department of Physics, School of Science, Tokyo Institute of Technology*)
S. Katsuki (*Institute of Pulsed Power Science, Kumamoto University*)
T. Kajiwara (*Institute of Pulsed Power Science, Kumamoto University*)
H. Ito (*Graduate school of science and engineering for education, University of Toyama*)
T. Honoki (*Graduate school of science and engineering for education, University of Toyama*)
T. Nakamura (*Graduate school of science and engineering for education, University of Toyama*)

N. Aoki (*Graduate school of science and engineering for education, University of Toyama*)

T. Mitani (*Graduate school of science and engineering for education, University of Toyama*)

T. Ozaki (*National Institute for Fusion Science*)

T. Terazawa (*Energy Support Co.*)

T. Kuno (*NGK Insulators, LTD.*)

CONTENTS

Study of an Injector (Induction Microtron) for Giant Cluster Ion Inertial Fusion Driver (G-CLIF)

Taufik, T. Adachi*, M. Wake*, K. Takayama*

The Graduate University of Advanced Studies

**High Energy Accelerator Research Organization, Accelerator Laboratory*

ABSTRACT

The use of Induction Microtron (IM) as an injector of a two-way multiplex induction synchrotron for the giant cluster ions inertial fusion driver has been studied. The IM is designed to accelerate high charge-state C-60 cluster ions from 10 MeV to 144 MeV. A typical bending magnet with a reverse field in its front and gradient field in the main dipole region, which gives the sufficient enough focusing in the vertical direction, is used. The various intrinsic natures in the transverse orbit beam properties has been manifested. The inherent COD is one of typical ones, which needs to be minimized by optimizing bending magnet design and introducing additional steering magnets. As a result of extensive trial, the dispersion-free on the long straight-section lattice has been achieved, which is crucial to avoid the emittance blow-up due to synchro-beta coupling. The beam with a momentum spread of $\Delta p/p$ = 0.00193 can be well-confined and accelerated by applying 1 kV barrier voltage and 10 kV acceleration induction voltage.

Keywords

Key Words : Induction microtron, injector, giant cluster ion, inertial fusion driver.

1. Introduction

Controlled nuclear fusion is one of the promising energy sources to fulfill the energy demand in the future. Unlike that of the other unsustainable power sources, the fuel for fusion such as D-T reaction is regarded to have no limit. In D-T reaction, the deuteron (D) and tritium (T) react in a high-temperature plasma phase (T≈ 10 keV), yielding a 3.5 MeV helium nucleus and 14.1 MeV fast neutron. The deuterium can be extracted from seawater because 1 part in 5000 of the hydrogen in seawater is deuterium. Meanwhile, tritium is obtained from a breeding process which neutron from fusion reaction captured by a lithium material in a fusion reactor.

Two principal approaches have been being developed to realize this fusion reactor, namely magnetic confinement and inertial confinement. The magnetic confinement system named Tokamak uses a huge magnets such as a toroidal magnet and poloidal magnets for confining the hot D-T plasma. Meanwhile, in the inertial fusion, the D-T capsule is heated by a laser or charged beam. They drive to generate a shockwave that can quickly compress D-T fuel and confine the D-T fusion reaction. The existing studies reports that the inertial fusion reactor has some advantages in the chamber reactor design compare to magnetic confinement fusion. However depositing high energy on the target in a short time is known to become a big challenge in the inertial fusion. [1] A laser has been used for heating the target but still have fatal limitations in efficiency and the final optic that is easily to be defected by a huge power of laser.

The heavy ion beam inertial fusion has apparently advantageous feature compared with the laser beam inertial fusion. Power transfer from the heavy ions beam to the fusion target material is quite clear. This makes it relatively easy to design the fusion target. The heavy ion beam can be non-destructively guided to the

fusion target without damaging on anything on the way. This allows practical and high-rep rate operation of the inertial fusion system. Furthermore, cluster ion have a larger stopping power than heavy ions. This may introduce more flexibility in target design. High charge-state cluster ions have higher acceleration efficiency, in addition to the fact that space-charge effects are notably relaxed. [2]

A two-way multiplex induction synchrotron has been proposed as a diver of the inertial fusion by a collaboration of KEK and some university in Japan. This induction synchrotron accelerates giant cluster ions such as Si-100 or C-60 more than 100 GeV propagating in opposite directions. For beam guiding and acceleration in the two-way multiplex induction synchrotron, the magnetic flux densities and induction acceleration fields are shared by the forward beams and backward beams. Induction Microtrons (IM), a racetrack shaped fixed field induction accelerators is used as an injector of this induction synchrotron.[2] This paper will describe details of notable characteristics of the induction microtron, focusing on the beam orbit dynamics there.

2. Giant Cluster Ion Acceleration

Acceleration of C-60 ions have been demonstrate using 14.5 MV tandem accelerator at IPNO[3], but electrostatic accelerator has limitation in high voltage generation. Acceleration using conventional RF accelerator is not possible due to a bandwidth limitation.[4] Therefore, induction synchrotron is the most likely to accelerate giant cluster ions to obtain high energy. The concept of induction synchrotron for heavy ions acceleration was demonstrated in 2013[5]. Induction synchrotron cannot accelerate C-60 ions from low to high energy, due to too slow revolution time and too big different ramping bending magnet. Preliminary acceleration is needed to accelerate C-60 to medium energy. There are several concepts to accelerate C-60 ions to the medium energy but induction microtron seems to be more realistic concept.[4]

3. The Outline of Induction Microtron

The IM is designed to accelerate C-60 with the charge state of 10 from 10 MeV to 144 MeV. It consists of 4 bending magnets which are configured so that the particle orbit become like a racetrack, as shown in Figure 1. Orbits are separated in the section between

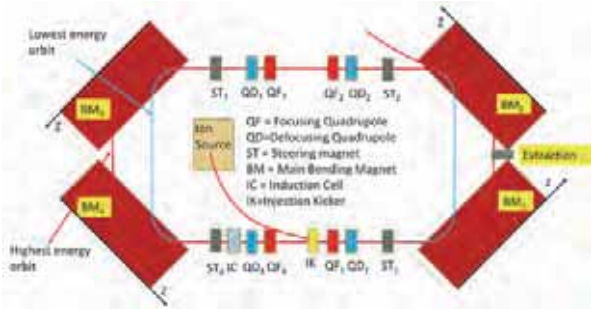

Fig. 1. Layout of the induction microtron.

BM_1 and BM_2, and the section between BM_3 and BM_4 according to the beam energy. On the other hand, all orbits pass through the common straight line without depending on the energy in the sections between BM_2 and BM_3, and BM_4 and BM_1. Quadrupole magnets, steering magnets and an acceleration device are placed in such two straight sections. A 10 kV induction cell is used to accelerate the C-60 ions.

Since the particles enter the bending magnet with an edge angle of 45°, the edge defocusing in the vertical direction becomes quite large. To give a net focusing effect in the vertical direction, the bending magnet is designed to have a reverse field region in the outer gap for the edge angle reduction and the gradient field in the inner gap, as shown in Figure 2. Figure 3 shows the magnetic flux density of the bending magnet.

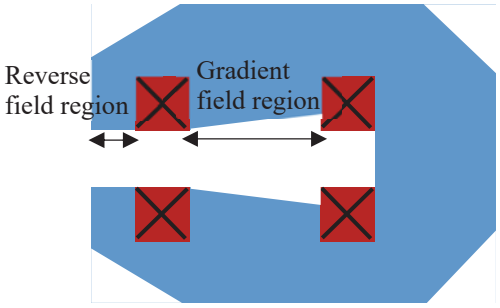

Fig. 2. Schematic of the magnet cross section.

4. Orbit Analysis

4.1 Stability of the transverse motion

For the acceleration without particle loss, it is

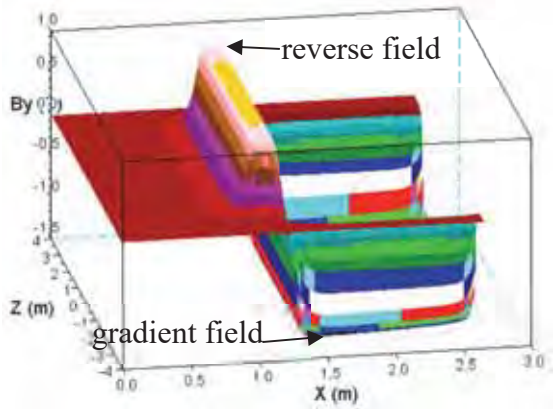

Fig. 3. Distribution of magnetic flux density in the median plane of the bending magnet.

important to ensure the stability of the transverse motion in a ring accelerator. A linear-optics calculation using a transfer matrix is well established for analysis of the transverse motion in a synchrotron.

Unfortunately, the linear-optics cannot be directly applied to the transverse motion in the IM, since the orbit in the bending magnet varies according to the beam energy. Therefore, two approaches are used to analyze the stability of the transverse motion in the IM; particle tracking simulation and linear-optics calculation. Runge-Kutta method is used in the particle tracking simulation by solving the equation of motion. A stable orbit is obtained by optimizing the field gradient of the quadrupole doublet at each turn. Once a one-turn orbit is fixed by the tracking simulation, magnetic field, field gradient and bending radius can be sampled along the orbit. Thus the linear-optics calculation is available to obtain one-turn transfer matrix M. The orbit is stable if the following condition is satisfied.

$$\left|\frac{Tr\mathbf{M}}{2}\right| \le 1$$

From those approaches, the gradient fields of the quadrupole doublet are optimized turn by turn.

4.2 Beta function

In the transverse direction, the ions oscillate against the reference orbit according to the betatron equation Eq. (1).

$$x'' + k(s)x = 0 \qquad (1)$$

where x is transverse coordinate and $k(s)$ is a focusing coefficient as a function of orbit path s. The size of the oscillation amplitude is crucial. It can be given by $(\varepsilon\beta)^{1/2}$ where ε is beam emittance and β is beta-function. ε is related to the beam parameter, while the beta function depends on the focusing component of the lattice. The horizontal beta-function of the IM at injection and extraction energy are shown in Figure 4.

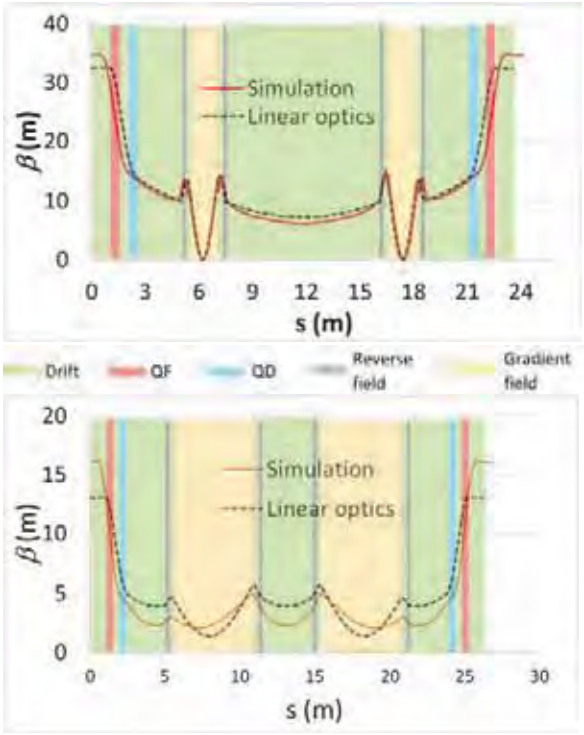

Fig. 4 Horizontal beta-function at injection (upper) and extraction energy (lower).

4.3 Closed Orbit Distortion

An ideal bending magnet is difficult to realize due to finite size of the magnet. The magnetic field difference (ΔB_y) relative to the ideal field generates a Closed Orbit Distortion (COD). As shown in the Figure 5, particle orbits in the bending magnet depend on the energy. Therefore, the field difference ΔB_y at each turn is not the same. This systematic ΔB_y becomes the source of inherent COD in the IM. It is important to design a magnetic field with small ΔB_y in order to reduce the inherent COD.

The ΔB_y makes the right hand side of the Eq. 1 become $-\Delta B_y/B\rho$ and the solution is

$$X_{COD}(s) = \frac{\sqrt{\beta(s)}}{2\sin(\mu/2)} *$$

$$\int_s^{s+C}\left\{-\frac{\Delta B_y(s')}{B\rho}\right\}\sqrt{\beta(s')}\cos\left[\mu/2 - |\Psi(s) -\right.$$

$\Psi(s')|]\, ds'$ (2)

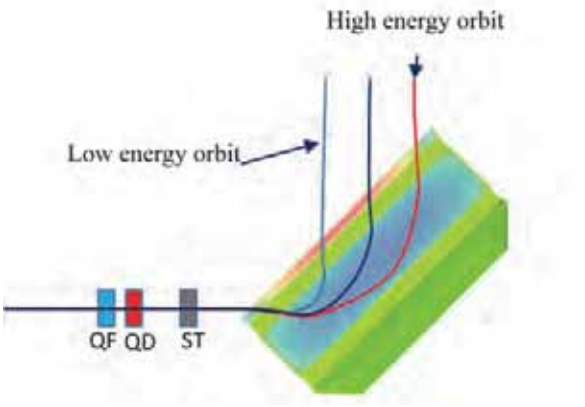

Fig. 5. Particle orbits in the bending magnet of IM.

where $B\rho$ is magnet rigidity, μ is phase advance and Ψ is betatron phase. The COD at injection energy is shown in Figure 6. The COD must be compensated by additional magnetic field of the steering magnet.

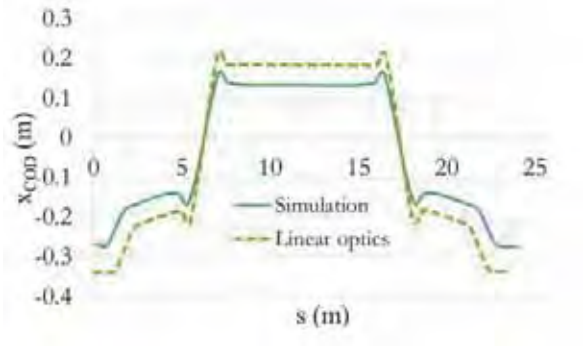

Fig. 6. COD at the injection energy

4.4 Dispersion function

Particles with slightly different momentum (Δp) to the ideal momentum (p) will oscillate with a different center of betatron oscillation (x_{eq}). The shift of x_{eq} influences the beam size of the IM and depends on the bending radius (ρ). The presence of $\Delta p/p$ causes the right hand side of Eq. 1 equal to $(\Delta p/p)/\rho$ and the solution becomes

$$D(s) = \frac{\sqrt{\beta(s)}}{2\sin(\mu/2)} \int_s^{s+C} \left(\frac{1}{\rho(s')}\right) \sqrt{\beta(s')} \cos[\mu/2 - |\Psi(s) - \Psi(s')|]\, ds' \quad (3)$$

where dispersion function $D(s) = x_{eq}/(\Delta p/p)$.

The dispersion function of IM at injection and extraction energy are shown in Figure 7. The dispersion function on the straight-section where the

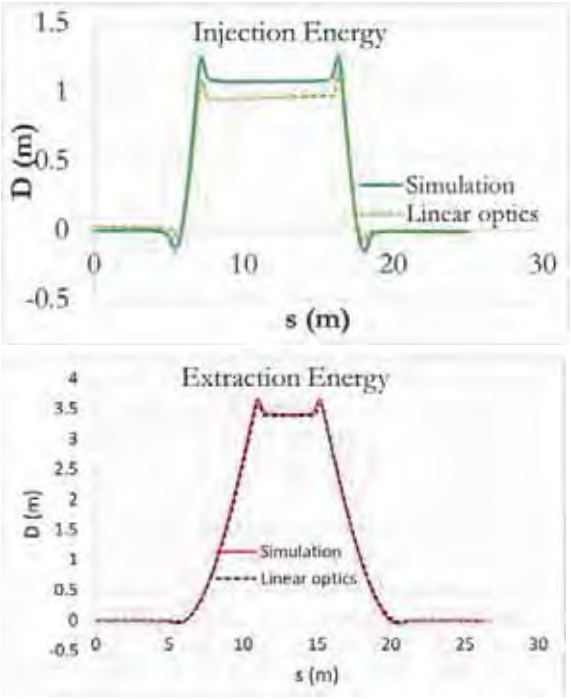

Fig. 7. Dispersion function of IM

induction acceleration device located is almost zero. Emittance blow up caused by synchro-beta coupling [6] can be avoided if the acceleration is done in the dispersion-free region.

4.5 Longitudinal motion

The injected particles in the IM have a small different energy (ΔE) and phase ($\Delta\phi$) to the synchronous particle. This condition affects the particle motion in the longitudinal direction mainly when passing through the acceleration section. The acceleration component of the IM uses an induction acceleration. Unlike an RF acceleration, the induction acceleration uses square voltage and two cells for accelerator voltage (V_{ac}) and barrier voltage (V_{bb}) generation as shown in Figure 8. For confinement,

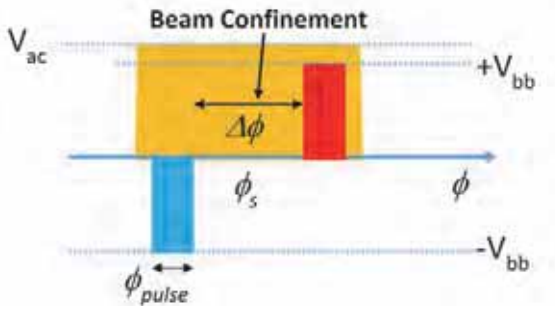

Fig. 8. Induction acceleration coltage.

two-opposite V_{bb} pulses with phase length ϕ_{pulse} are

generated in different phase $\Delta\phi$.

The longitudinal motion of IM is calculated by the following acceleration equation

$$\left.\begin{aligned}(\Delta E)_{n+1} &= (\Delta E)_n + q[V_{bb}(\phi_n) - V_{ac}] \\ \phi_{n+1} &= \phi_n + \frac{2\pi\eta_{n+1}}{(\beta^s_{n+1})^2 E^s_{n+1}}(\Delta E)_{n+1}\end{aligned}\right\} \quad (4)$$

where E^s is synchronous particle energy, n is turn number, q is the charge, β^s is synchronous relativistic beta, η is slippage factor, $(\Delta E)_n = E_n - E^s_n$, $\frac{\Delta p}{p} = \frac{(\Delta E)}{(\beta^s)^2 E^s}$, $\eta_{n+1} = \alpha_{n+1} - \frac{1}{(\gamma^s_{n+1})^2}$, γ^s is synchronous relativistic gamma, and α is momentum compaction factor. Momentum compaction factors of the IM are specific. Unlike a synchrotron which has constant momentum compaction factors, the momentum compaction factors of the IM are increase with particle energy as shown in Figure 9.

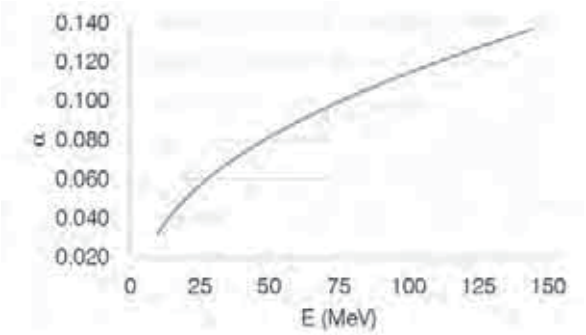

Fig. 9. Momentum compaction factor of IM

Assuming 1 kV V_{bb} is set with ϕ_{pulse} = 12° and $\Delta\phi$ = 24°. A 10 kV V_{ac} is generated in the other induction cell. Injection ions have a normal distribution of $\Delta p/p$ and random distribution of ϕ. By setting V_{bb} = 1 kV, the beam size in the phase space decreases and confines around $\Delta\phi$ at the extraction energy as shown in Figure 10.

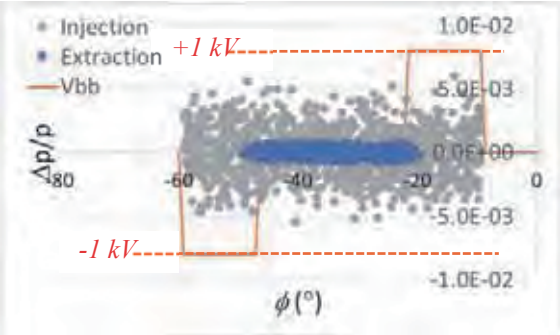

Fig. 10 Longitudinal beam size in the phase space.

Some ions with high $\Delta p/p$ may not be confined during the acceleration process. The unconfined ions will be lost due to facing unstable transverse motion. Figure 11 show the survival rate of the ions when the standard deviation (σ) of the $\Delta p/p$ is varied. Because of decreasing of $\Delta p/p$ at each turn, the ions lost occur only at the early stage of acceleration. At V_{bb} = 1 kV, 100% of the survival rate can be achieve at maximum of σ = 0.00193.

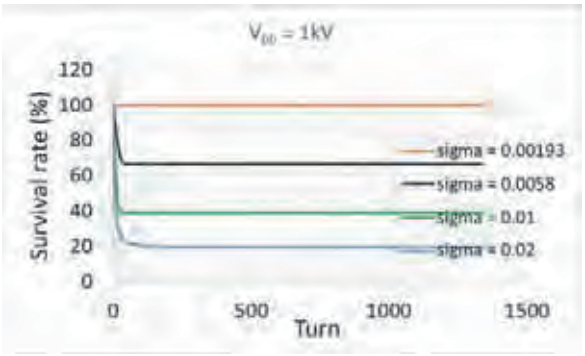

Fig. 11. Survival rate of the ions as function of σ

5. Conclusions

The induction microtron is possible to accelerate giant cluster ion up to the medium energy. An optimized bending magnet design and additional steering magnet is needed to minimize the inherent COD. The dispersion-free on the acceleration device location of the IM will not induce emittance blow up. The longitudinal motion shows that the beam can be confined well at σ = 0.00193.

References

[1] W. M. Sharp et al., “Inertial Fusion Driver by Intense Heavy-Ion Beams”, *Proc. of 2011 Particle accelerator Conference*, PAC'11 OC/ IEEE, pp.1386–1393 (2011).

[2] K. Takayama et al., “A Quantum Beam Driver for The Future Inertial fusion”, in 21st International Symposium on Heavy Ion Fusion, Astana, Kazakhstan, (2016).

[3] P. Attal et al., “ORION project : acceleration of ion clusters and highly charged biomolecules from 10 MeV to 1GeV”, *Nucl. Instr. and Meth.*, **A328**, pp.293–299 (1993).

[4] K. Takayama et al., “Racetrack-shape fixed field induction accelerator for giant cluster ions”, Phys. Rev. ST Accel. Beams, vol. 18, p. 050101, 2015.

[5] K.Takayama et al., “Induction Acceleration of Heavy Ions in the KEK Digital Accelerator: Demonstration of a Fast-Cycling Induction Synchrotron”, Phys. Rev. ST Accel Beams, vol. 17, p. 010101, (2014).

[6] T. Monma et al., “Coherent Synchro-Beta Coupling in the KEK Digital Accelerator”、Proc. of HI-AT2015, MO-PA16 (2016).

Target Design for Giant Cluster Ion Inertial Confinement Fusion

Toru Sasaki, Kazumasa Takahashi, Takashi Kikuchi, Shigeo Kawata*,
Kazuhiko Horioka**, and Ken Takayama***

Nagaoka University of Technology

**Utsunomiya University*

***Tokyo Institute of Technology*

****High Energy Accelerator Research Organization, Accelerator Laboratory*

ABSTRACT

A target design is discussed and the related parameters of cluster-ion-beam inertial confinement fusion (CIF) are estimated in this paper. The particle energy of cluster-ion-beam as Si-100 is determined the range of conventional heavy-ion-beam inertial confinement fusion parameter. Considering stopping power of cluster-ion beam, we estimated the radiator temperature and the heating time. A one-dimensional hydrodynamics simulation of CIF target with determined parameters was demonstrated from the estimated particle energy of cluster-ion-beam as Si-100. The temperature and the density of DT achieve 1 keV and 10^5 kg/m^3 at the maximum compression time, respectively.

Keywords

Cluster-ion-beam inertial-confinement-fusion, Stopping power, Target structure, Radiation temperature, Target hydrodynamics

1. Introduction

In inertial confinement fusion, possible energy drivers include intense lasers[1], heavy-ion beams(HIBs) [2-4], or pulsed power[5]. The features of inertial confinement fusion driven by heavy ion beams are high conversion efficiency from the driver to the target, well-defined deposition energy, and so on. The driver energy in heavy-ion inertial confinement fusion (HIF) is expected to be the order of tenth MJ[2]. However, the particle energy and the pulse width of HIF, which are determined by the stopping power of the target, were up to 10 GeV and 10 ns. Therefore, the extremely high current beams for heavy ion fusion, which is about 100 kA, are required, and the beam parameter becomes space-charge dominated beam [3]. Therefore, we consider reducing the beam current with keeping the driver total energy.

Recently, the inertial confinement fusion driven by the intense cluster ion beams has been proposed [6]. Its driver consists of an induction microtron [7] as an injector, permanent magnet multiplex stacking ring, and two-way multiplex induction synchrotron as a main accelerator. The induction synchrotrons have been experimentally demonstrated [8]. They are capable of accelerating all ion species with arbitrary q/m and velocity. Recently, high-flux cluster ion sources have been proposed and developed. The typical particle flux density at the peak of Si-cluster beams is expected to be 6×10^{15} cluster/s cm^2 [9]. Energy drivers based on the cluster ion beams are expected to reduce the current density. However, the

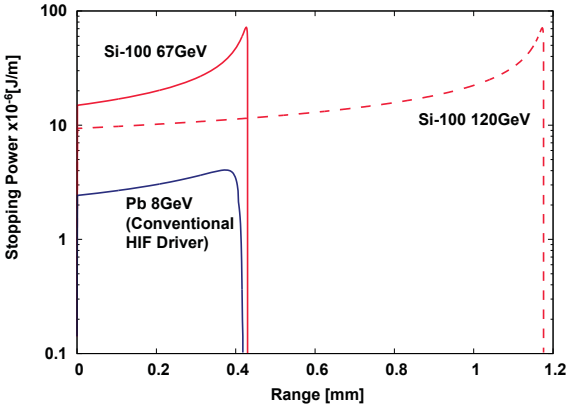

Figure 1 Stopping ranges of several projectiles for aluminum target with the solid density.

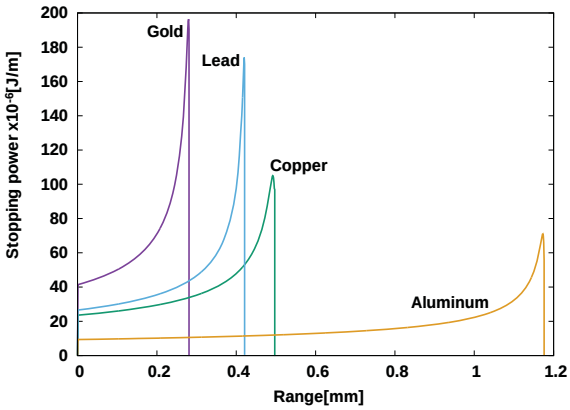

Figure 2 Stopping ranges of Si-100 for several targets at normal temperature with solid density.

non-linear energy deposition on the target is not well-clarified yet [10-12]. We should understand the target dynamics from the energy deposition to the implosion of fuel target.

In this study, the target design and related parameters of cluster-ion-beam inertial confinement fusion (CIF) were estimated. From the estimation, the one-dimensional hydrodynamics simulation of CIF targets was demonstrated.

2. Target design from stopping power of cluster projectile

The particle energy of cluster ion beams for Si-100 provided by KEK is expected to be up to 120 GeV. From the energy, we have estimated the deposition energy and its range.

Figure 1 shows the stopping ranges of several projectiles for the aluminum target with the solid density. The stopping range is estimated from Ref. [11]. To compare the range of cluster projectile, the lead projectile having 8 GeV of particle energy, which is basically considered HIF driver beams, is also showed. This estimation is not contained the non-linear cluster effect. Compared to the range of the lead projectile, that of Si-100 projectile having 120 GeV is too long. To adjust the range of lead projectile, the particle energy of Si-100 projectile is set to be 67.2 GeV as shown in Fig. 1.

From the expected projectile energy, the cluster beam current assuming Z=1 of the charge state and 10 ns of the pulse duration is approximately 15 kA. The result shows that the space-charge effect can be reduced in the comparison of HIF. The scenario of the two-way and multiplex induction synchrotron[6] is supposed to be Z=8 of the charge state. Although the space-charge effect increases, q/m of the cluster ion is relatively small compared to the expecting HIF driver.

Figure 2 shows the stopping ranges of Si-100 for several targets at normal temperature with solid density. The particle energy of Si-100 is 120 GeV. The results show that the deposition energy increases with high-Z and dense target. It suggests that the dense high-Z target becomes a high-energy-density state.

The stopping power of cluster-ion beam has been studied several theoretical estimations with including correlation effect[12]. However, the stopping power in the high velocity range using cluster-ion beam has not been demonstrated. The theoretical estimations and the experimental results for the stopping power are important study for the realization of CIF.

3. Indirect or direct drive inertial confinement fusion

One of the key issues in the ICF target is an irradiation non-uniformity on the target. To avoid the non-uniformity, we select the indirect target. On the other hand, the direct drive ICF target provides an efficient thermo-nuclear fusion gain. In this section, we estimate the requirement parameters both driving method in ICF.

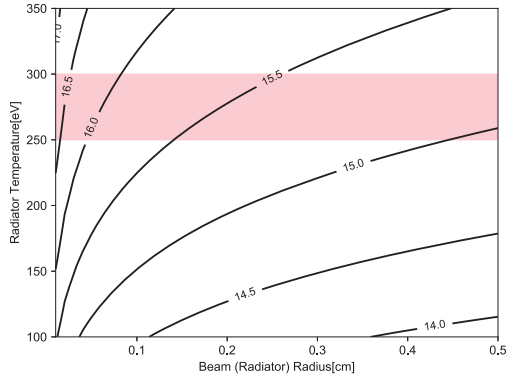

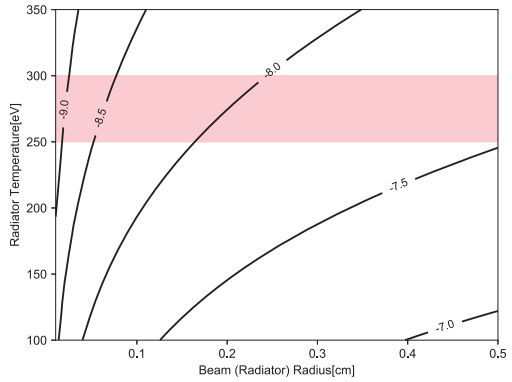

Figure 3 Estimated radiation temperature and heating time of aluminum radiator for indirect target.

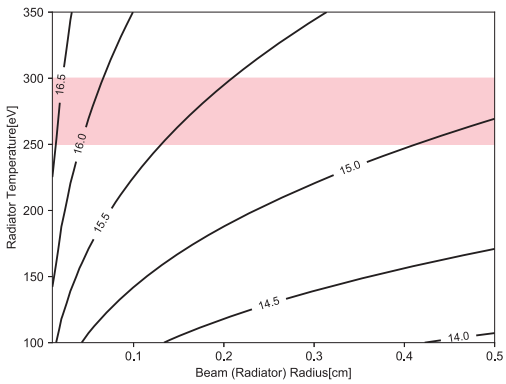

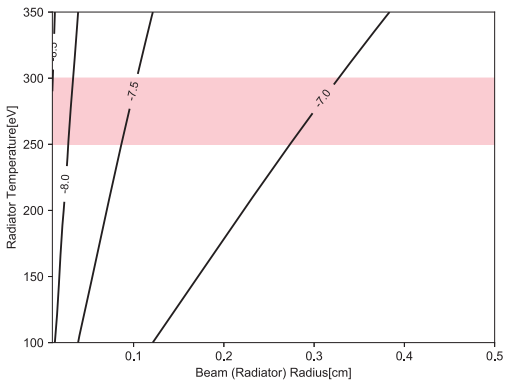

Figure 4 Estimated radiation temperature and heating time of gold radiator for indirect target.

To estimate the requirement specific power and the heating time, we used Ref. [13]. Figure 3 shows an estimated radiation temperature and heating time of aluminum radiator for indirect target. To achieve 300 eV of radiation temperature with several tenth nanoseconds of heating time, the requirement specific power is estimated to be about 10^{16} W/g with 1 mm of beam radius. Figure 4 also shows an estimated radiation temperature and heating time of gold radiator for indirect target. Comparing with these results, the gold radiator is difficult to achieve requirement parameters for the indirect ICF. Generally, the deposition energy mainly dissipates the ionization energy of radiator materials. Thus, the radiator temperature for high-Z materials decreases even if the energy density is high. In the case of using aluminum radiator, the requirement particle number par bunch is 6.67×10^{12} with estimating from the average stopping power. The particle number is expected to provide the scenario using two-way and multiplex induction synchrotron. Although, we should consider the conversion efficiency from the beam to the fuel target [14].

Assuming linear stopping power theory, we demonstrated an implosion dynamics of direct irradiation CIF using a one-dimensional hydrodynamic simulation. The hydrodynamic behavior of CIF target is also important to achieve the implosion. At the first step, we compared the target hydrodynamic behavior driven by HIBs to that driven by CIBs. The hydrodynamic behaviors of target were treated as a one-dimensional spherical-model. The equation of state and the transport properties are used as QEOS[15] and Lee-More model[16], respectively. The target structure and the time evolution of the energy input are respected to Ref. [4]. The particle energy of CIBs is set to be 67.2 GeV.

Figure 5 shows the time-evolution of temperature and density profiles of the target at the irradiating

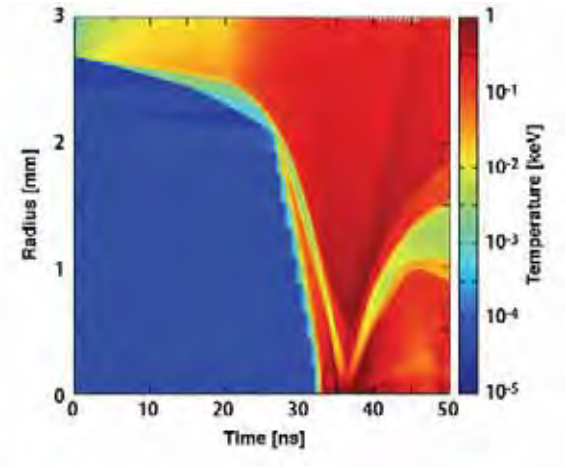

(a) Temperature

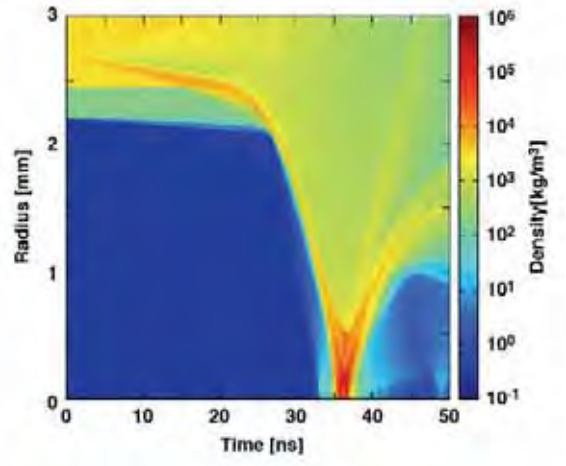

(b) Density

Figure 5 Time-evolution of temperature and density profiles of the target at the irradiating CIBs.

CIBs. The temperature and the density of DT at the maximum compression time achieve 1 keV and 10^5 kg/m^3, respectively. Compared to the hydrodynamic behavior in HIF, that in CIF is almost similar.

4. Conclusions

The target design is discussed and the related parameters of cluster-ion-beam inertial confinement fusion (CIF) are estimated. The particle energy of cluster-ion-beam as Si-100 is determined the range of conventional heavy-ion-beam inertial confinement fusion parameter. Considering stopping power of cluster-ion beam, we estimated the radiator temperature and the heating time. A one-dimensional hydrodynamics simulation of CIF target with determined parameters was demonstrated from the estimated particle energy of cluster-ion-beam as Si-100. The temperature and the density of DT achieve 1 keV and 10^5 kg/m^3 at the maximum compression time, respectively. We will consider the nonlinear effect of the stopping power to optimize the target.

Acknowledgment

This work was partly supported by JSPS KAKENHI Grant Number 17K19091.

References

[1] R. S. Craxton, *et. al.*, Phys. Plasmas, **22**, 110501 (2015).
[2] K. Horioka, *et. al.*, Nucl. Instrum. Methods Phys. Res. A, **606**, p.1 (2009).
[3] T. Kikuchi, *et. al.*, Laser and Particle Beams, **20**, pp. 589–593 (2002).
[4] T. Someya, *et. al.*, Laser and Particle Beams, **24**, 359-369 (2006).
[5] A. B. Sefkow, *et. al.*, Phys. Plasmas, **21**, 072711 (2014).
[6] K. Takayama and K. Horioka, presented at HIF2016 (2016).
[7] K. Takayama, *et. al.*, Phys. Rev. Accel. Beams, **18**, 050101 (2015).
[8] K. Takayama, *et. al.*, Phys, Rev. Lett., **98**, 054801 (2007).
[9] Y. K. Bae, *et. al.*, Phys. Rev. A, **51**, R1742 (1995).
[10] C. Deutsch and N. A. Tahir, Phys. Fluids B, **4**, 3735 (1992).
[11] T. A. Mehlhorn, J. Appl. Phys., **52**, 6522 (1981).
[12] M. Vicanek, *et al*, Phys. Rev. A, **46**, 5745 (1992).
[13] M. Murakami, *et. al.*, J. X-ray Sci. Tec., **2**, 127 (1990).
[14] R. Ramis, *et. al.*, Nucl. Instrum. Methods Phys. Res. A, **A415**, 93 (1998)
[15] R. M. More, et. al.: Phys. Fluids, **31**, 3059 (1988).

[16] Y. T. Lee and R. M. More: Phys. Fluids, **27**, 1273 (1984).

Numerical Analysis of Particle Dynamics in a Linear Inertial Electrostatic Confinement Fusion Device

Jun Hasegawa, Kohei Okutomo, Tomonobu Itagaki, Eiki Hota, Kei Takakura, and Toshiyuki Kohno

Institute of Innovative Research, Tokyo Institute of Technology

ABSTRACT

This paper reports results of numerical analyses on spatial and velocity distributions of fast hydrogen atoms produced by charge-exchange reactions in a linear IEC device. We developed a one-dimensional numerical model based on the Monte Carlo method to predict spectral shapes of Balmer-α emission from a high-voltage glow-discharge plasma. The model was partly successful in reproducing the experimentally observed Ha spectra and neutron production rates. We also examined the dependencies of fusion reaction rates on discharge voltage and background gas pressure. This newly developed model is useful to optimize the design of the IEC devices.

Keywords

Inertial electrostatic confinement, D-D fusion, neutron source, Monte Carlo simulation

1. Introduction

In the inertial electrostatic confinement (IEC) fusion device, deuterium ions produced by glow discharge are accelerated toward a high-voltage cathode and electrostatically confined in a negative potential well. The recirculating motion of the deuterium ions is expected to enhance fusion reaction rate between deuterons, thus making the IEC device an attractive candidate for compact neutron generators. After a pioneering work by Miley [1], various types of IEC neutron sources have been developed [2-4]. Neutron production rates (NPR) more than 10^8 n/s have already been achieved in these previous studies.

On the other hand, the actual behaviors of deuterium particles in the IEC device are very complicated because of huge amount of collisions between the particles accompanied by momentum transfer, charge exchange, ionization, dissociation and so on. Particularly, interactions between fast particles (D, D^+, D_2, D_2^+, and D_3^+) and background gas molecules (D_2) determines the velocity distributions of the deuterium particles causing D-D fusion reactions. The cross section of D-D fusion reaction strongly depends on particle velocity in an energy range less than a few hundred keV. Thus, for optimizing the design of the IEC device, it is important to understand correlations between the operational parameters of the IEC device and the velocity distributions of the fast particles that potentially cause fusion reactions.

The purpose of this study is to develop a one-dimensional numerical model including various collisions and reactions between fast ions/atoms and background neutral molecules, and to investigate the dependence of the fusion reaction rate on the discharge parameters. To check the validity of the model, we compare calculated Hα spectra with experimentally observed ones. We evaluate also fusion reaction rates under various discharge conditions.

2. Experimental Setup

Figure 1 shows a cross-sectional view of the linear IEC device developed as a new compact neutron source. The overall structure of the device is axisymmetric. A hollow cathode and two facing anodes made of stainless steel are arranged coaxially on the center axis with gap lengths of 115 mm. The cathode has an inner diameter of 60 mm and a length of 100 mm. The anode consists of coaxially arranged

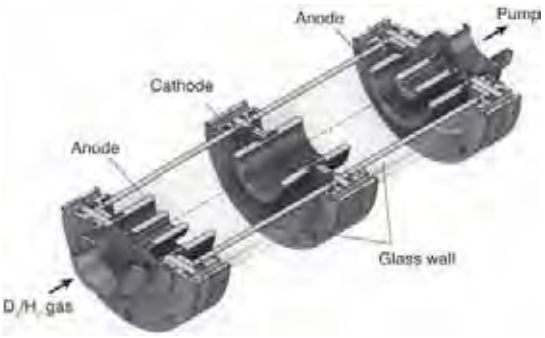

Fig. 1. A cross-sectional view of the developed linear IEC device.

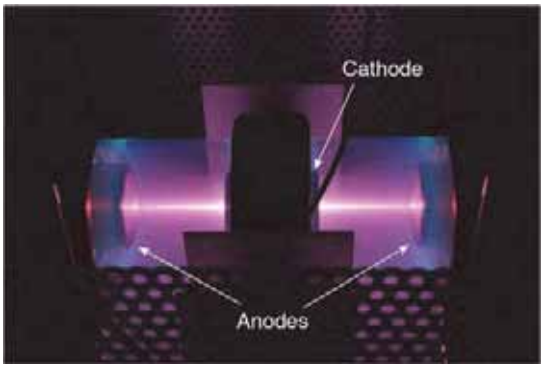

Fig. 2. A typical glow discharge pattern observed in the IEC device. The discharge voltage and current are, respectively, 18 kV and 6 mA. The working gas is hydrogen.

two cylinders having inner diameters of 20 mm and 75 mm. The electrode thickness is 10 mm. The side walls are 8-mm-thick glass tubes having an inner diameter of 134 mm.

Fuel gas is supplied from one end of the device through a solenoid valve (≤10 sccm) and evacuated by a turbo molecular pump from the other end of the device. The pumping speed is limited by a manual valve located before the pump. The gas pressure is maintained to be ~1 Pa by controlling the solenoid valve with a feedback signal from a diaphragm pressure gauge.

In the present study, the cathode was negatively biased up to –30 kV by a regulated high-voltage power supply to induce high-voltage glow discharge in hydrogen gas. The power supply was operated in a constant current mode and the discharge voltage was indirectly controlled by changing the hydrogen gas pressure. A typical discharge pattern observed is shown in Fig. 2. A bright plasma column was formed along the center axis of the device.

We performed a spectroscopic measurement of hydrogen Balmer series emission from the discharge plasma using a 50-cm monochromator (grating: 600 cm^{-1}) combined with a high-resolution EMCCD camera (pixel size: 16 μm×16 μm). The light emitted from the region inside the hollow cathode was extracted through the anode center hole and focused by a ø30-mm plano-convex lens (f = 300 mm) onto the inlet of an optical fiber connected to the spectrometer. The wavelength resolution of this spectroscopy system is calculated to be ~0.045 nm/px if all aberrations of the optics are ignored.

3. Numerical model

A 1D numerical model based on the Monte Carlo (MC) method was developed to obtain the distribution functions of fast particles $f_i(x, v)$ in the linear IEC device. Here, x and v are, respectively, the position and velocity of hydrogen atoms when they cause Hα emission after charge-exchange reactions with background deuterium/hydrogen molecules. The

Table 1. Reaction processes considered in the 1D numerical model.

Projectiles	Reactions
H^+	$H^+ + H_2 \rightarrow$ fast H
	$H^+ + H_2 \rightarrow H\alpha$
	$H^+ + H_2 \rightarrow$ momentum transfer
D^+	D-D fusion
H_2^+	$H_2^+ + H_2 \rightarrow H_3^+ + H$
	$H_2^+ + H_2 \rightarrow$ slow H_2^+
	$H_2^+ + H_2 \rightarrow$ fast H^+
	$H_2^+ + H_2 \rightarrow H\alpha$
D_2^+	D-D fusion
H_3^+	$H_3^+ + H_2 \rightarrow$ fast H^+
	$H_3^+ + H_2 \rightarrow$ fast H_2^+
	$H_3^+ + H_2 \rightarrow$ fast H
	$H_3^+ + H_2 \rightarrow$ fast H_2
	$H_3^+ + H_2 \rightarrow H\alpha$
	$H_3^+ + H_2 \rightarrow$ momentum transfer
D_3^+	D-D fusion
H	$H + H_2 \rightarrow$ slow H_2^+
	$H + H_2 \rightarrow$ fast H^+
	$H + H_2 \rightarrow H\alpha$
	$H + H_2 \rightarrow$ momentum transfer
D	D-D fusion
H_2	$H_2 + H_2 \rightarrow$ fast H_2^+
	$H_2 + H_2 \rightarrow$ fast H^+
	$H_2 + H_2 \rightarrow H\alpha$
	$H_2 + H_2 \rightarrow$ momentum transfer
D_2	D-D fusion

suffix *i* denotes the species of parent particles such as H^+, H_2^+, H_3^+, H, and H_2. All reactions considered in this model are listed in Table 1. To calculate the probabilities of these reactions except for fusion reactions, we used hydrogen cross section data given by Tabata *et al.*[5] Among these reactions in the table, the followings lead to the emission of Balmer Hα:

$$H^+ + H_2 \rightarrow H(n=3) + ... \quad (1)$$
$$H_2^+ + H_2 \rightarrow H(n=3) + ... \quad (2)$$
$$H_3^+ + H_2 \rightarrow H(n=3) + ... \quad (3)$$
$$H + H_2 \rightarrow H(n=3) + ... \quad (4)$$
$$H_2 + H_2 \rightarrow H(n=3) + ... \quad (5)$$

By reactions (2) and (3), excited hydrogen atoms are produced through the dissociation of fast molecules (H_2 and H_3). Thus, they have a half or a third of the kinetic energy that the parent molecular ions gain in the electrostatic field. Fast neutral atoms (H) and molecules (H_2), which are produced by charge exchange reactions between ions and background molecules, also causes Hα emission through the reactions (4) and (5). In the case of deuterium gas discharge, the same cross section data was used for deuterium particles having equivalent velocities. In addition, D-D fusion reactions were considered using an empirical formula given by Ragheb [6]. Since fusion cross sections are much smaller than those for the other atomic processes, they were artificially enhanced ($\times 10^8$) in this model to obtain a sufficient number of fusion reactions within a practical calculation time.

The electrostatic potential calculated in advance by using COMSOL Multiphysics® was imported to the MC code. Because the model treated a weakly ionized plasma, the Debye shielding was ignored. Positions and velocities of a particle were advanced by the leap-frog method and recorded in each time step until the particle escapes from the calculation region. By accumulating 10^7 trials and analyzing the particle record, we obtained distribution functions related to specific events such as Hα emission and D-D fusion reaction.

3. Results and Discussion

3.1 Characteristics of basic IECF setup

Figure 3 shows a typical Hα spectrum observed with a glow discharge of 30 kV, 10 mA, and 0.57 Pa. In addition to a sharp central peak, broad red- and blue-shifted peaks due to the "beam" components of hydrogen atoms are separately observed on both sides of the central peak. Clearly, these side peaks are composed of Hα emissions originating from different ion species. The highest energy evaluated from the far edge of the side peaks well coincides with the maximum acceleration energy of H^+ ions.

Calculated spatial and velocity distributions of fast hydrogen atoms that finally cause Hα emissions are shown in Fig. 4. In this calculation, 10^7 initial ions were uniformly distributed in the discharge gap. From the cross sections of electron impact ionization of H_2, the initial density ratio of H^+ to H_2^+ was determined to be 1:20. The solid curves express total Hα emission and the other curves show the contributions of various parent ions and neutrals. The spatial distributions show that Hα emission is the strongest in the hollow cathode (Fig. 4a), which is almost consistent with the experimental observation in Fig. 2. Hα emissions originating from ions (H^+ and H_2^+) have clear peaks, but those from neutrals (H and H_2) are almost position independent. These results can be understood by the energy dependence of Hα emission cross sections.

Meanwhile, the velocity distributions show more complex features. From this result, one can see the contribution of each parent particle species to the total Hα emission quantitatively. Figure 5 compares the numerically predicted Hα spectrum with the observed one. Although the relatively high energy parts of the

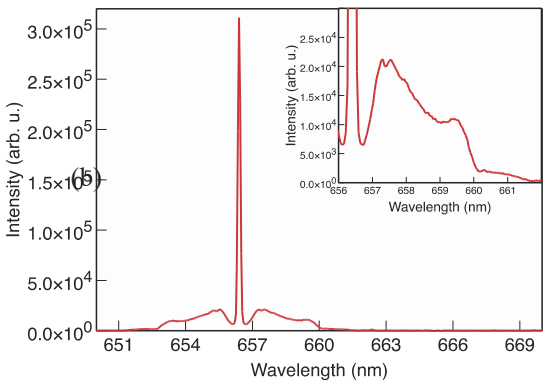

Fig. 3. A typical Hα spectrum observed under a discharge condition of 30 kV, 10 mA, and 0.57 Pa.

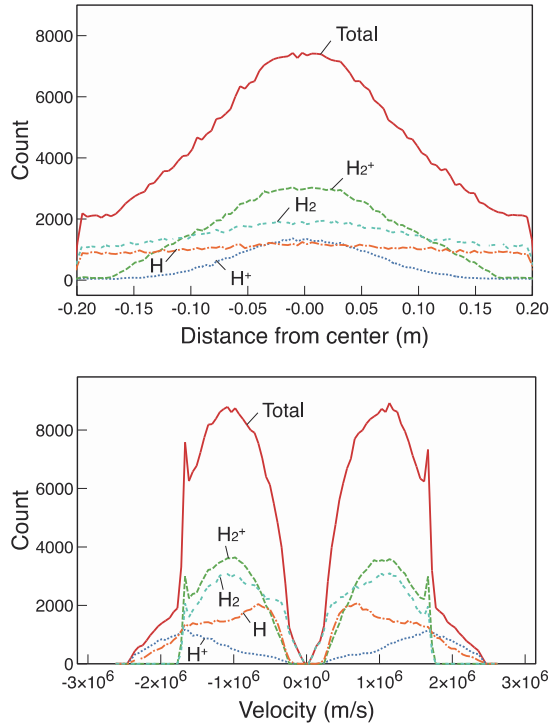

Fig. 4. Calculated spatial (upper) and velocity (lower) distributions of hydrogen atoms that finally cause Hα emissions.

Doppler-shifted components are well reproduced by the MC calculation, there exist large discrepancies between the experiment and the MC calculation. This is probably because the uniform spatial distribution of the initial ions was incorrect. The ion impact ionization (β effect), which is not taken into account in the present MC code, may contribute to the generation of the initial ions much more than expected.

Figure 6 shows the dependencies of the number of

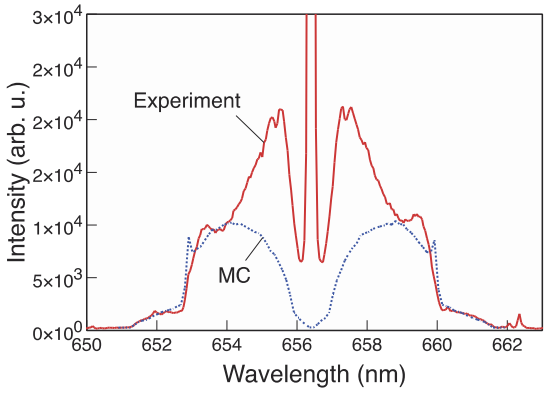

Fig. 5. Comparison between a numerically predicted Hα spectrum and an experimentally obtained one.

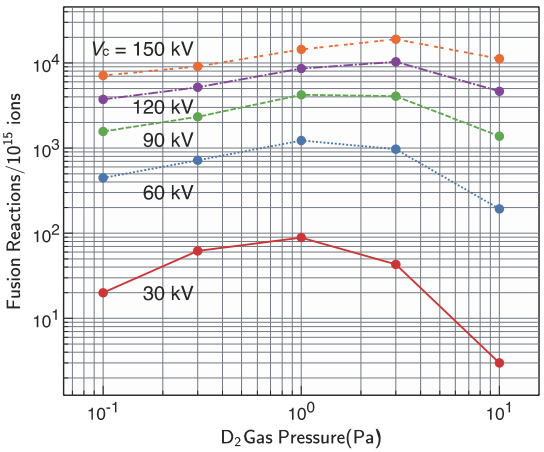

Fig. 6. Dependencies of the number of D-D fusion reactions on discharge voltage and background gas pressure.

fusion reactions on the discharge voltage and the background deuterium gas pressure. One can see that the number of the D-D fusion reactions drastically increases with increasing the discharge voltage. Meanwhile, there is an optimal gas pressure that maximizes the fusion reactions in each discharge condition with fixed cathode voltage. The optimal gas pressure slightly increases from 1 Pa to 3 Pa with increasing discharge voltages from 30 kV to 150 kV, indicating that smaller gap distances are more preferable when we operate the IEC device with higher discharge voltage.

In Fig. 6, the MC calculation predicts that ~4.2×10^{3} neutrons can be generated by 10^{15} initial ions under a discharge voltage of 90 kV. When the discharge current is 10 mA, we can evaluate the ion production rate to be 10^{-2} [A]/1.6×10^{-19} [C]≃6.3×10^{16} [s^{-1}]. Thus, the NPR in the above discharge condition is estimated to be $4.2\times10^{3}/10^{15}\times6.3\times10^{3} \simeq 2.6\times10^{5}$ n/s. This is smaller than the NPR obtained in our experiment using the linear IEC device by a factor of about 4. In order to obtain more reliable data, it is necessary to improve the developed numerical model, but it is probably useful for examining the scaling rule of NPR.

4. Conclusions

We developed a 1D numerical model based on the MC scheme to predict the spatial and velocity distributions of Hα emitting fast hydrogen atoms

generated from various ion species in IEC devices. The model was partly successful in reproducing the experimentally observed Hα emission spectra and neutron production rates. Thus, this numerical approach will be useful for optimizing the design of IEC devices if its accuracy is more improved. A 3D MC code is under construction, which takes account of also secondary particles generated by various collisional processes in the IEC discharge plasma.

References

[1] G. H. MILEY *et al.*, "Inertial-Electrostatic Confinement Neutron/Proton Source", *Proc. 3rd Int. Conf. on Dense Z-pinches*, AIP Press, pp.675–688 (1994).

[2] J. F. SANTARIUS, *et al.*, "Overview of University of Wisconsin Inertial-Electrostatic Confinement Fusion Research", *Fusion Science and Technology*, **47**, 4, pp. 1238-1244 (2005).

[3] K. YOSHIKAWA, *et al.*, "Research and Development of Landmine Detection System by a Compact Fusion Neutron Source", *Fusion Science and Technology*, **47**, 4, pp. 1224-1228 (2005).

[4] K. YAMAUCHI, *et al.*, "Performance of neutron/proton source based on ion-source-assisted cylindrical radially convergent beam fusion", *IEEJ Transactions on Fundamentals and Materials*, **126**, 11, pp.1177-1182 (2006).

[5] T. TABATA and T. SHIRAI, "Analytic cross sections for collisions of H^+, H_2^+, H_3^+, H, H_2, and H^- with hydrogen molecules," *Atomic Data and Nuclear Data Tables*, **76**, 1, pp. 1–25 (2000).

[6] M. RAGHEB, "Fusion Concepts", 2016, http://mragheb.com/NPRE%20402%20ME%20405%20Nuclear%20Power%20Engineering/Fusion%20Concepts.pdf.

Spectroscopic analysis of Linear shaped Inertial Electrostatic Confinement Fusion (IECF) device

Tomonobu Itagaki, Kohei Okutomo, Jun Hasegawa,
Eiki Hotta, Kei Takakura, Toshiyuki Kohno

Tokyo Institute of Technology

ABSTRACT

Inertial Electrostatic Confinement Fusion (IECF) is a nuclear fusion scheme, which electrically confines and accelerates glow-discharge-generated deuterium ions, and causes fusion reactions. This scheme is expected to be applied to compact, less expensive neutron sources. We developed a linear-shaped IECF device, which is advantageous for high power operation to increase neutron production rate. We analyzed the particle motions from Doppler-shifted Hα spectra in discharge experiments using hydrogen gas instead of deuterium gas.

Keywords

inertial electrostatic confinement fusion, neutron source, spectroscopy, plasma, glow discharge,

1. Introduction

The original concept of Inertial Electrostatic Confinement Fusion (IECF) was proposed by P. T Farnsworth[1]. After Miley studied an IECF device as a neutron source [2], and various types of IECF devices have been researched[3]. In typical IECF devices, a high voltage (typically from several tens to a hundred kV) is applied to a grid cathode at the center of the grounded vacuum anode chamber. Deuterium ions generated by glow discharge in low pressure (about 1 Pa) deuterium gas are accelerated toward the cathode and cause nuclear fusion reactions. These ions are confined in an electrostatic potential well formed between the electrodes.

Recently IECF devices are expected as neutron sources for landmine detection[7], SNM (Special Nuclear Material) inspection, and so on, since they are compact enough to carry and able to produce neutrons without radioisotopes. Figure 2 shows various applications of neutron sources depending on neutron production rate (NPR). Neutron sources for portable inspector need to provide NPRs about 10^9 n/s, but there remains considerable effort to reach such NPRs, since the order of NPR reported in many studies on portable IECF devices are about 10^6 to 10^7 n/s [8, 9].

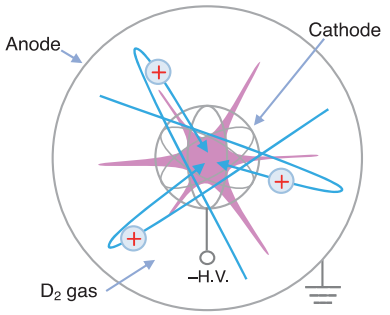

Fig. 1. Principle of IECF devices.

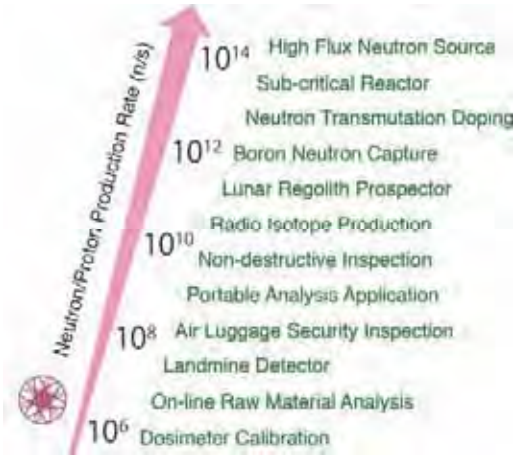

Fig. 2. Neutron source applications in various levels of NPR.

2. Discharge parameters related to NPR

Discharge current, voltage, and gas pressure strongly affect the NPR of IECF devices. In most cases, the neutron production in IECF devices is considered to be dominated by the fusion reactions between accelerated ions and background neutral particles from the experimental fact that the NPR is proportional to the discharge current.

When we assume monoenergetic ion beams, the NPR is given by:

$$NPR = \sigma(E) v n_b n_0,$$

where E is ion energy and $\sigma(E)$ is fusion cross section, v is ion velocity, and n_b and n_0 are the number densities of ion beam and background deuterium gas, respectively.

The simplest way to increase the NPR is to increase the discharge current, which means the increase of ion flux vn_b. Increasing applied voltage increases the ion velocity v and the fusion cross section $\sigma(E)$. The background particle number density n_0 is directly connected to the gas pressure.

Increasing current and voltage results in electrode heating. Particularly, the grid cathode is difficult to be cooled in the spherical IEC devices. In addition, higher voltage operation needs lower target gas density (background gas pressure). So, it is necessary to find the condition that maximize the NPR, but it is hard to determine the optimal condition theoretically, since the particle motions in the IECF devices are very complex.

3. Linear type IECF device

We developed a linear-type IECF device, which is suitable for cooling the electrodes during high power operation. As shown in Fig. 3(a), this IECF device is composed of a hollow cathode and two cylindrical anodes, which are coaxially arranged in an alumina tube. The exposed electrodes enable us to cool them directly. Further, this configuration also simplifies the design of high voltage isolation against arc discharge between the electrodes because a high voltage feedthrough is not necessary.

For spectroscopic measurement, we also built an IECF device having the side insulating walls made of glass tube as shown in Fig. 3(b).

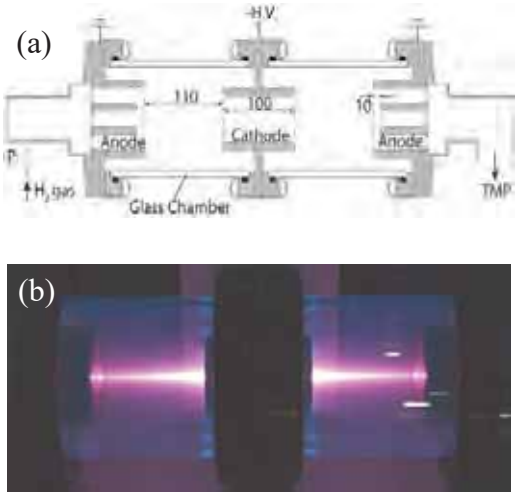

Fig. 3. (a) Schematic of linear shaped IECF device. (b) Glow discharge plasma during operation (30 kV, 10 mA).

4. Particle motion analysis from Doppler shifted Hα spectrum

In IECF devices, charge exchange reactions have an important role. These reactions make accelerated ions to fast neutral particles. As shown in the following formulae, the velocity of the produced fast neutral particle is equal to that of its parent ion.

- $H^+(E) + H_2 \rightarrow H^*(E) + H_2^+$
- $H_2^+(E) + H_2 \rightarrow H^*(E/2) + H + H_2^+$
- $H_3^+(E) + H_2 \rightarrow H^*(E/3) + H_2 + H_2^+$

Here, E denotes the kinetic energy of the parent ion. From the Doppler shift of the light emitted from the neutral particle, we can evaluate the velocity of the parent ion. Thus, we examined indirectly the ion velocity distribution in the IECF device by observing Doppler shifted Hα spectra from discharge plasma.

Figure 4 shows the configuration of the spectroscopic measurement. The measurement was performed from two directions. In case 1, the light emitted from the region inside the cathode was collected by a lens located on the center axis through the side viewport. In case 2, the light was observed through the glass wall from the direction of the line of sight inclined 60 degrees to the equipment axis.

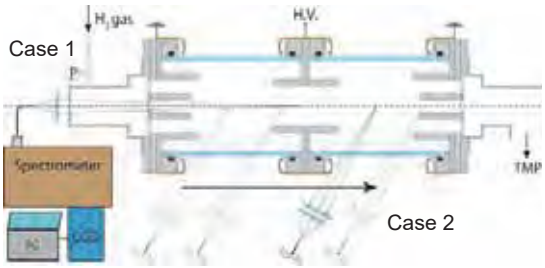

Fig. 4. Experimental setup for spectroscopic measurement.

4.1 Hα spectra from the cathode center

Figure 5 shows Hα spectra measured at the cathode center under various discharge conditions. Figure 6 enlarges the righthand side of the Hα spectra. Each Doppler-shift consists of a few peaks, which are clearly separated from the original peak of Hα. The Doppler-shift components of the spectra have shoulders where the intensities decrease sharply and gentle tails outside the shoulders.

Figure 7 shows the spectra plotted with respect to the kinetic energies of H and H_2 calculated from the velocities of Hα-emitting hydrogen atoms. The ends of the shoulders and the tails of the spectra coincide with the maximum kinetic energies of H_2^+ and H^+ ions determined by the discharge voltage, respectively. This result shows that there are multiple species of parent ions at least H^+ and H_2^+ in the device during discharge, and the spectrum is the convolution of components from that the fast neutral particles originating from different parent particles.

Figure 8 shows a typical result of curve fitting of the Hα spectrum with Gaussian functions. As shown in the figure, four Gaussian curves well reproduce the spectrum; the center peak located at the original Hα position corresponds to the thermal component, and the others correspond to the Doppler-shift components. From this analysis, we evaluated two quantities by using the fitted Gaussian curves; one is the ratio of the height of the two Gaussian peaks (F2/F1), and the other is the ratio of the area of the thermal component to the sum of the area of the fast (Doppler-shift) components. Each Gaussian curve of the Doppler-shift component is not related to the species of parent ions, so its area is not meaningful quantitatively.

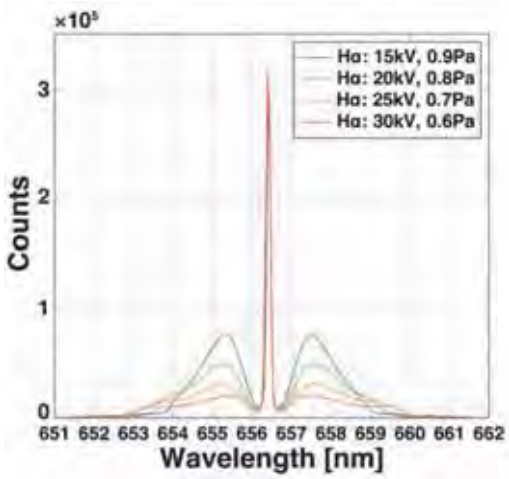

Fig. 5. Hα spectra measured from the axial direction (case 1 of Fig. 4).

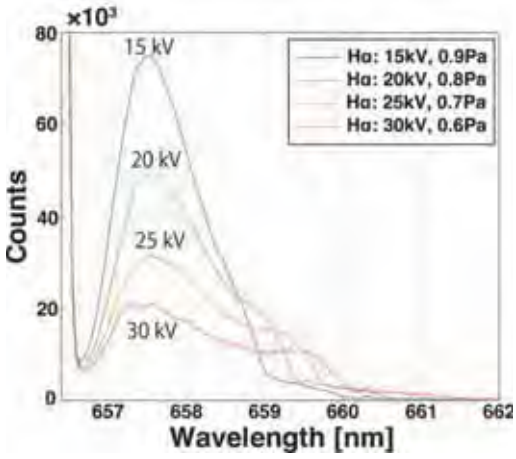

Fig. 6. An enlarged view of the red shift components of the Hα spectrum.

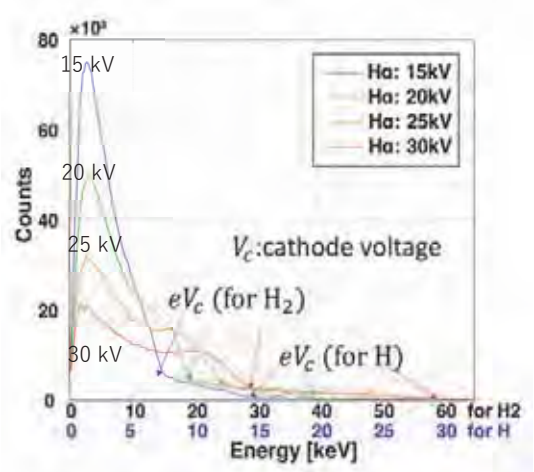

Fig. 7. Hα spectra plotted with respect to the kinetic energies of parent ions.

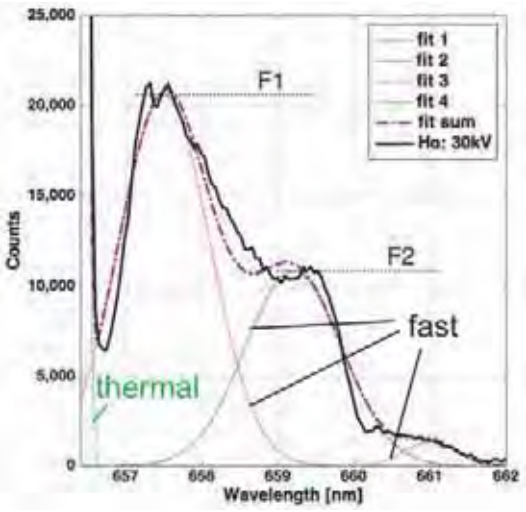

Fig. 8. Fitting of the Hα spectrum with Gaussian curves.

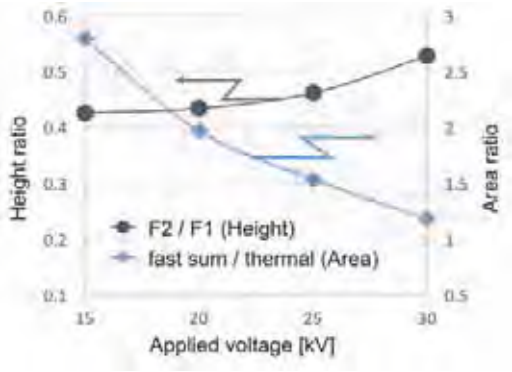

Fig. 9. Analysis by Gaussian fitting.

From Fig. 9, one can see that the ratio F2/F1 gradually increases as the applied voltage increases, which means that H_2^+ ions are more effectively accelerated by the potential drop between the electrodes. The decreasing gas pressure as the voltage rises also may contributed to the increase of F2/F1 because of increased mean free pass of ions.

On the other hand, the areal ratio of the Doppler-shift component to the thermal one decreases significantly as the voltage rises. This may be due to the increase of the mean free path of electrons, which decreases electron impact ionization and ion generation in the discharge plasma.

4.2 Relationship between spectrum intensity and axial position

Figure 10 shows a typical Hα spectrum measured from directions of 60 degrees at three different

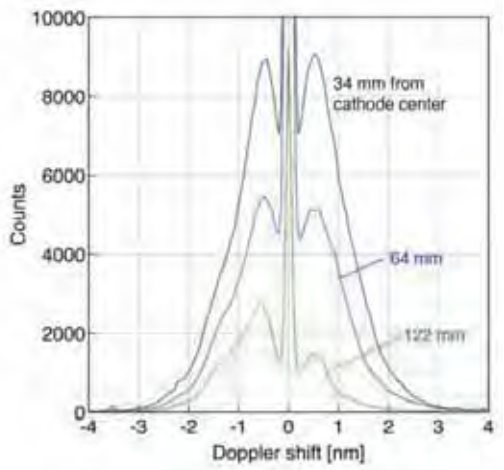

Fig. 10. Typical Hα spectra observed at different axial positions (case 2 in Fig. 4).

positions on the axis. The spectrum shape changes depending on the distance from the cathode. The Hα line spectrum near the cathode is intense and symmetric. When the observation point moves away from the cathode, the spectrum becomes asymmetric, indicating that the amount of fast neutrals flowing out of the cathode is larger than those towards the cathode.

Figure. 11(a) plots the areas of the thermal and Doppler-shift components of the spectrum separately as the function of distance from the cathode. The boundaries between the components are defined as shown in Fig. 11(b). The intense light emission from the region near the cathode means that a lot of charge exchange reactions occur there.

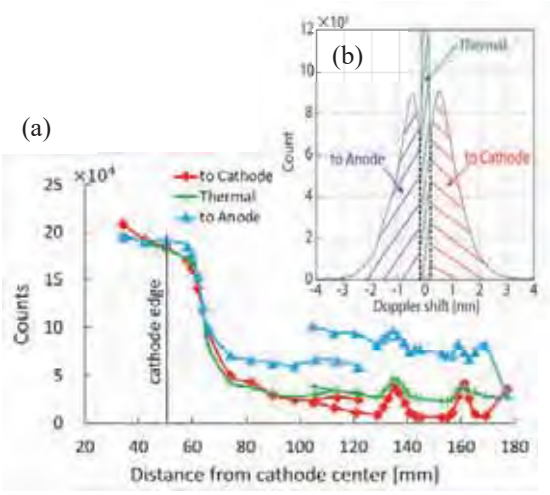

Fig. 11. (a) Light emission intensities vs. axial position. (b) Definition of thermal and Doppler-shift components.

5. Conclusions

We developed a linear type inertial electrostatic confinement fusion device as a compact and radioisotope free neutron source. Its linearly arranged electrodes enable us to efficiently cool them directly with improved withstand voltage. So, it is suitable for high-power operation of the IECF device, which needs to improve the neutron production rate.

We analyzed particle motions in the device spectroscopically by observing Doppler shifted Hα spectrum. The observed Hα spectra indicated that multiple ion species at least H^+ and H_2^+, coexist in the device. We also found that a lot of fast neutral particles generated inside cathode. Their collision with background thermal particles has considerable contribution to the spectrum. Decomposition of these complex components is a future task.

References

[1] P.T. Farnsworth “Electric Discharge Device for Producing Interactions Between Nuclei”, U.S. Patent, No. 3, 258, 402 (1966).

[2] G. H. Miley, et al. “Inertial-Electrostatic Confinement Neutron/Proton Source”, Third international conference on dense 2-pinches, AIP conference proceedings, vol 299, pp.675–689

[3] George.H.Miley, S. Krupakar Murali. (2014). “Inertial Electrostatic Confinement Fusion”, Springer.

[4] T.A. Thorson, et al. “Fusion reactivity characterization of a spherically convergent ion focus”, Nuclear Fusion, Vol. 38, No. 4, (1998) pp.495-507

[5] John Hedditch, et al. “Fusion energy in an inertial electrostatic confinement device using a magnetically shielded grid”, Phys. Plasmas 22, 102705 (2015)

[6] “High-Energy Electron Confinement in a Magnetic Cusp Configuration”, Phys. Rev. X 5, 021024 (2015)

[7] Kiyoshi Yoshikawa et al. “Research and development of a compact discharge-driven D–D fusion neutron source for explosive detection”, Nucl. Instr. and Meth. in Phys. Res. B 261 (2007) pp.299–302

[8] Kiyoshi Yoshikawa, et al. “Current Status of Inertial Electrostatic Confinement Fusion research”, J. Plasma Fusion Res. Vol.83, No.10 (2007) pp.795-811. (in Japanese)

[9] Kiyoshi. Yoshikawa, et al, “Current Status of IEC (Inertial Electrostatic Confinement) Fusion Neutron/Proton Source Study”, 17th Summer Seminar on Fusion Reactor Technology (2001).

Control of laser produced plasma flow by magnetic nozzle

M. Tsukamoto, H. Fujii, J. Hasegawa, K. Horioka

Department of Mechanical Engineering, Tokyo Institute of Technology

ABSTRACT

Ion current density of laser produced plasma modulated by a magnetic nozzle was measured in order to investigate the possibility of plasma flux control for laser ion sources. We found that the enhancement ratio of the plasma ion flux changes depending on the position and the magnetic field strength of the magnetic nozzle.

Keywords

Heavy ion fusion, laser ion source, laser-ablation, high-density plasma flow, magnetic nozzle

1. Introduction

To accelerate and transport heavy ion beams to high energy enough to implode and ignite a fuel target of Heavy Ion Fusion (HIF), we need to adopt an ion sources that can provide high-current and low-emittance ion beams at the injection section of the driver accelerator. The laser ion source has the potential to supply an ion beam with high current and low emittance because the source plasma is initially produced by laser with a small size and particle orbit becomes ballistic during rapid expansion of the plasma into vacuum. On the other hand, the laser ion source has a problem that ion flux reduces largely with distance from the laser target because of three-dimensional plasma expansion.

To make the best use of characteristics of the laser ion source and resolve the problem of ion flux reduction, control of plasma by magnetic field has been proposed. Harilal *et al*. observed confinement of laser produced plasma by a transverse magnetic field (magnetic nozzle) [1]. Okamura *et al*. conducted transport and confinement of laser produced plasma by a solenoid magnetic field, but control of the directivity of plasma ions has been an issue [2]. We aim to realize ion beam extraction with high flux and low emittance by forming a high intensity magnetic nozzle near the target and controlling the directivity of laser-produced plasma by magnetic nozzle. There are two mechanisms by which the magnetic nozzle acts on the plasma. One is the plasma compression effect caused by the magnetic pressure. The induced $\boldsymbol{j} \times \mathbf{B}$ force suppresses the transverse expansion of entire plasma and maintains high ion flux. The other one is ion focusing due to an electrostatic field caused by charge separation. In a magnetic field, electrons are focused by the magnetic lens effect, and also ions are focused by the electrostatic field induced by charge separation. This mechanism is called collective focusing [3]. The supply of plasma ion flux is influenced by these two focusing effects dependent on magnetic field strength. Thus, it is an important issue to find the optimum strength and configuration of the applied magnetic field.

In this study, we measured the ion current density under various strengths and positions of the magnetic nozzle, which enables us to evaluate the ion focusing effects by magnetic pressure and collective focusing.

2. Experimental Setup

The schematic diagram of the experimental setup is given in Fig. 1. The experimental apparatus was composed of a plasma production chamber, a drift chamber, a magnetic nozzle coil, and a KrF excimer laser. The plasma production chamber was evacuated to about 10^{-5} Pa by a turbo molecular pump and an oil sealed rotary pump. To produce an ablation plasma, we

used the KrF excimer laser (wavelength: 248 nm, pulse width (FWHM): 30 ns, maximum pulse energy: 300 mJ). The laser was focused with a plano-convex lens through an optical window onto a plane copper target with an incident angle of 30 degrees. The laser target was mounted on an automatic XY-axis stage to change the position of the target without breaking vacuum. This enabled us to change the laser irradiation position on the target every 10-20 shots to avoid the irreproducibility of the produced plasma due to target surface deformation by successive laser irradiation at the same position. A solenoid coil for the magnetic nozzle was located near the target. It was excited by a pulse current of 1.8 kA peak from a LCR circuit. The coil applied a magnetic field of 550 mT at maximum to the expanding plasma. The excitation current was changed by the charging voltage of the capacitor. In this study, the coil was located at three different distances from the target of 1.5 mm, 3 mm, and 5 mm. For the design of the magnetic nozzle, we calculated the shape of the magnetic field by COMSOL Multiphysics®. Figure 2 shows the calculated magnetic field distribution when a pulse current of 1.8 kA was applied to the coil 15 μs after the triggering of the excitation circuit. The ion flux of the laser produced plasma after expansion through the magnetic nozzle was measured by using a Faraday cup (FC) installed in the drift chamber. The FC was mounted on a linear feedthrough with a stroke of 254 mm and covered with an aluminum cage having an aperture of φ 5 mm. The FC was located at various positions 80-627 mm downstream from the laser target. Ions were extracted by a bias voltage of -50 V between the cage and the cup and detected with an oscilloscope.

3. Results and Discussion

The dependence of the plasma ion flux on the distance in the z direction without magnetic field was first investigated. Figure 3 shows ion flux waveforms measured at FC positions of 433-633 mm downstream from the laser target. As shown in Fig. 3, the pulse widths of the ion flux increase with increasing the distance, indicating that the plasma flow expanded sufficiently to extract ion beams with pulse lengths

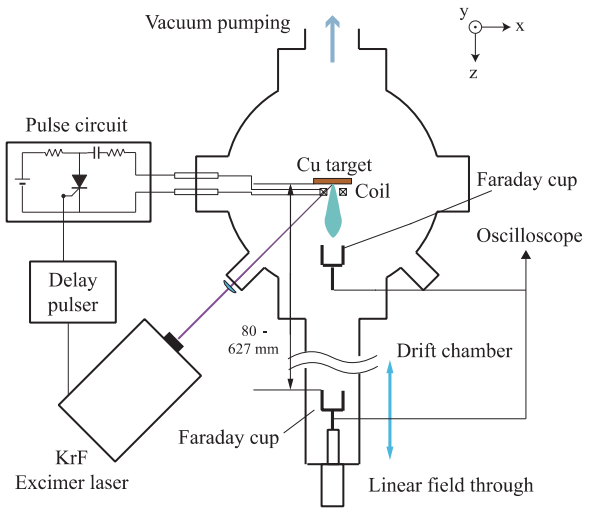

Fig. 1. Schematic diagram of experimental apparatus.

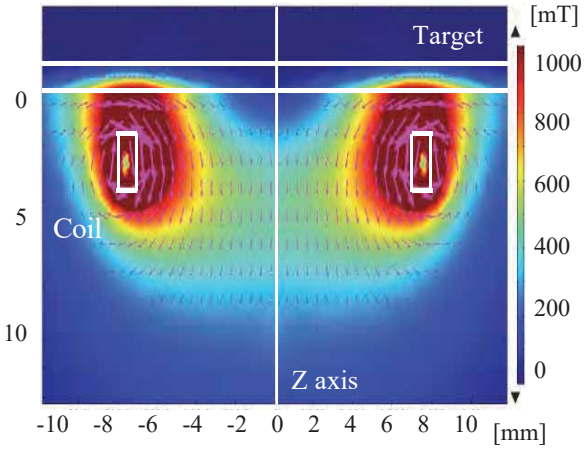

Fig. 2. A snapshot of magnetic field distribution 15 μs after the onset of the excitation current. with a coil position of 1.5 mm and a pulse current of 1.8 kA.

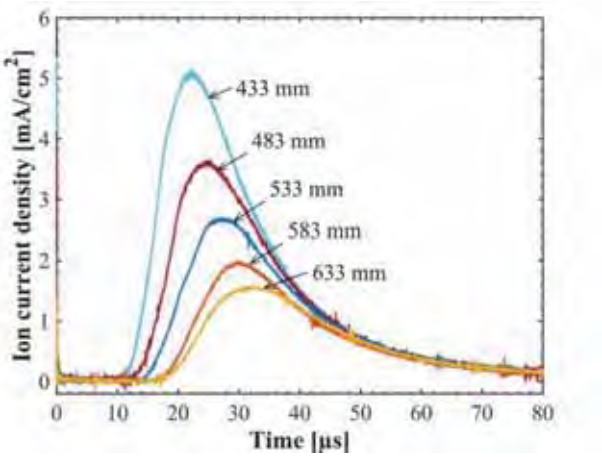

Fig. 3. Dependence of the ion flux on the distance in the z direction without magnetic field.

larger than several tens of microseconds.

The dependence of plasma ion flux on the distance

in the z direction was investigated with pulsed magnetic field induced by a solenoid. The ion flux increased when the magnetic field was applied. The result indicates that the laser produced plasma flowing through the magnetic nozzle is confined and compressed by the magnetic pressure, suppressing the three-dimensional expansion of the plasma. Figure 4 shows the dependence of the ion current density on the strength of magnetic field. The ion flux was observed 80 mm downstream from the target. The ion current density increased with the increase of the magnetic field. A second peak was observed in the current waveforms with magnetic flux densities more than 260 mT. This indicates that ions in the peripheral part of the plasma plume were focused by the effect of collective focusing. On the other hand, only the first peak was observed at FC positions larger than 433 mm (Fig. 4).

In order to discuss the influence of plasma compression effect on the ion flux, ion flux measurements were performed at three different positions of the solenoid magnetic field. In advance to the experiment, the z-axis center magnetic flux density distribution was calculated for three different positions of the solenoid magnetic field by using the COMSOL Multiphysics®. A magnetic flux density of 550 mT can be induced by a peak current of about 1.8 kA when the coil is located 5 mm from the target. On the other hand, as shown in Fig. 5, the maximum magnetic flux density is limited to be about 350 mT with a coil position of 1.5 mm. Under these magnetic field conditions, we investigated the enhancement ratio of the ion flux as shown in Fig. 6. As the strength of magnetic field increased, the ion flux increased due to the plasma compression effect. By applying solenoid magnetic fields around 300 mT, the ion flux increased by a factor of 4.5 compared with no magnetic field cases. However, the enhancement ratio of the ion flux decreased under magnetic flux densities more than 420 mT. In addition, the enhancement ratio was almost independent of the solenoid position under the same magnetic fields. These results are discussed more in detail below.

First, the decrease of the ion flux under strong

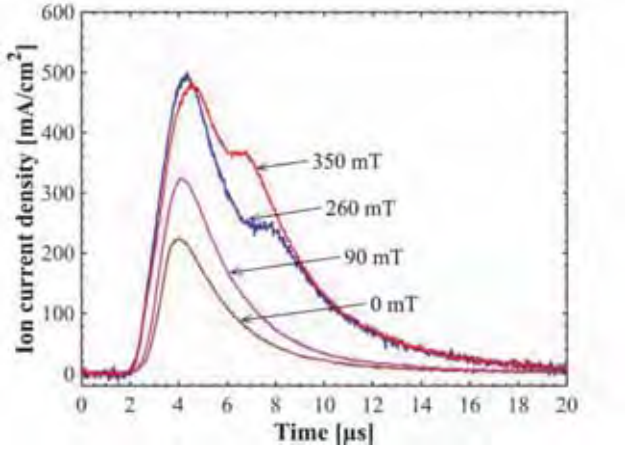

Fig. 4. Dependence of the ion flux on magnetic field strength observed 80 mm downstream from the target.

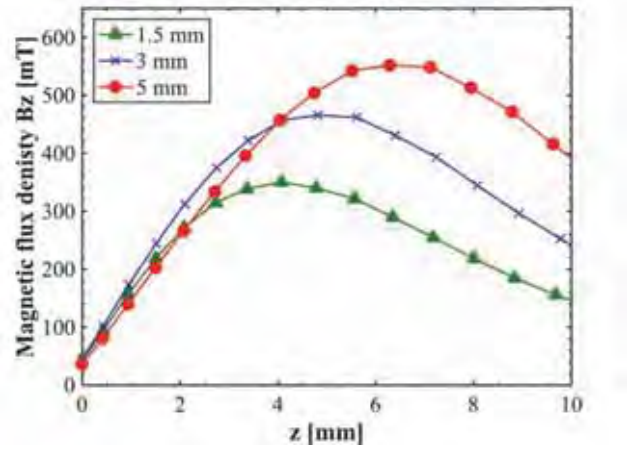

Fig. 5. Calculated magnetic flux density distributions along z axis for three different positions of solenoid.

magnetic fields may be attributed to the excessive ion focusing caused by the collective focusing effect. Then, the ion trajectories become diverging. According to our simulation results using the Hybrid PIC method, the slower particles passing near the coil, that is, the peripheral particles in the plasma plume are more strongly converged, and the trajectories of those ion are excessively modulated in the transverse direction [4].

Second, to explain why the position of the solenoid has less influence on the enhancement ratio of the ion flux, it is necessary to consider the magnetic pressure acting on plasma. The $\boldsymbol{j} \times \mathbf{B}$ force applied to the plasma is almost independent of the solenoid position as shown in Fig. 5, indicating that the magnetic pressure is almost the same in all cases with different solenoid positions. We consider that this is why ion

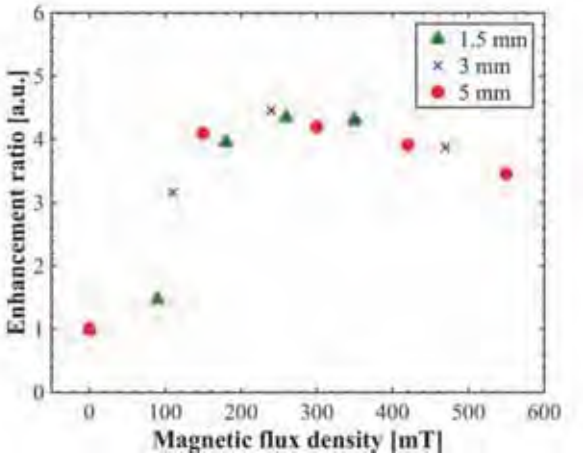

Fig. 6. Enhancement ratio of ion flux observed under three different solenoid magnetic fields. Faraday cup position is 433 mm downstream from the target.

current densities observed in Fig. 6 does not depend on the solenoid position.

4. Conclusions

In this study, to clarify the optimum condition of the solenoid magnetic field distribution that maximizes the compression effect of the laser produced plasma, the solenoid position dependence of the magnetic nozzle effect was investigated by observing plasma ion flux under different magnetic field conditions. The results show that the enhancement of the ion flux does not depend the solenoid position so much and excessive ion focusing was observed under strong magnetic fields. It is necessary to discuss ion behavior more in detail by measuring the angle dependence of plasma ion flux near the target and measuring emittance of extracted ion beams.

References

[1] S. S. Harilal et al., "Confinement and dynamics of laser-produced plasma expanding across a transverse magnetic field", *Phys. Rev.*, E **69**, 026413 (2004).

[2] M. Okamura et al., "Magnetic plasma confinement for laser ion source", *Rev. Sci. Instrum.*, **81**, 02A510 (2010).

[3] S. Robertson., "Collective focusing of an intense ion beam", *Phys. Rev. Lett.*, **48**, pp.141-151 (1982).

[4] H. Fujii, "Effect of the axial magnetic field on ion momentum distribution of laser induced plasma", master thesis (2017).

Spectral Shift of Kα-lines by Multipleionization from Hot Plasma Produced by a Heavy Ion Beam

Takayuki Okui, and Tohru Kawamura

Department of Physics, School of Science, Tokyo Institute of Technology

ABSTRACT

In hot plasma creation by heavy-ion-beam irradiation, K-shell ionization of target atoms is accompanied by outer-shell ionization by ion impacts. This process is called multipleionization. In the case that multipleionization by incident heavy ions is comparable to single ionization by plasma electrons, an ionization degree of target atoms is enhanced, giving misleading estimation of plasma temperature if the processes are not considered in plasma diagnostics. In this study, Kα spectra are calculated with and without the multipleionization by solving population kinetics under collisional radiative equilibrium (CRE), and plasma conditions where the multipleionization has a large contribution are clarified.

Keywords

Kα spectroscopy, heavy-ion-beam irradiation, multipleionization, population kinetics

1. Introduction

Kα spectroscopy is one of useful diagnostics to estimate density and/or temperature of plasma generated by a heavy ion beam. Kα line is emitted when a K-shell electron is ionized by ion impacts, and a charge state of the Kα line is mainly determined by outer-shell ionization by electron impacts. The plasma conditions can be deduced according to the charge states of the spectra. In hot plasma creation by heavy-ion-beam irradiation, K-shell ionization of target atoms is accompanied by outer-shell ionization by ion impacts. This process is called multipleionization. In the case that multipleionization processes by heavy ions are comparable to single ionization by plasma electrons, an ionization degree of target atoms is enhanced, and plasma temperature estimated with Kα spectra can be lower compared with the case that the processes are neglected.

In a previous study [1], a demonstration of Kα lines from low charge chlorine with M-shell electrons, which are associated with Cl^{+}-Cl^{7+}, was examined for cold dense C_2H_3Cl plasma diagnostics by numerical simulation. In the study, plasma ion density is assumed to be solid (~10^{23} cm^{-3}). Therefore, even if the multipleionization related with M-shell is occurred to chlorine by an incident ion beam, because of high density electrons up to ~10^{23} cm^{-3}, the M-shell ionization is governed by surrounding plasma electrons, and the effects of multipleionization on Kα spectra may not stand out.

In this study, we will widely discuss plasma conditions where the multipleionization processes have an obvious contribution to Kα spectra by numerical simulation.

2. Cross Sections of Multipleionization Processes

If the multipleionization is treated as simultaneous independent single ionizations of binding electrons, the probability can be expressed by single electron ionization probabilities. Assuming that all the electrons in same shell are ionized with same probability, a cross section for ionizing a single K-shell electron, n_L L-shell electrons, n_M M-shell electrons, … and n_J J-shell electrons has a binomial distribution [2]:

$$\sigma_{1\mathrm{K},n_\mathrm{L}\mathrm{L},n_\mathrm{M}\mathrm{M},\ldots,n_\mathrm{J}\mathrm{J}} = \sigma_\mathrm{K} \binom{N_\mathrm{L}}{n_\mathrm{L}} P_\mathrm{L}^{n_\mathrm{L}} (1-P_\mathrm{L})^{N_\mathrm{L}-n_\mathrm{L}} \times \binom{N_\mathrm{M}}{n_\mathrm{M}} P_\mathrm{M}^{n_\mathrm{M}} (1-P_\mathrm{M})^{N_\mathrm{M}-n_\mathrm{M}} \times \ldots \binom{N_\mathrm{J}}{n_\mathrm{J}} P_\mathrm{J}^{n_\mathrm{J}} (1-P_\mathrm{J})^{N_\mathrm{J}-n_\mathrm{J}}, \quad (1)$$

where σ_K represents a cross section of K-shell ionization. N_L, N_M, … , N_J and P_L, P_M, … , P_J stand for number of L-, M-, … , J-shell electrons and single L-, M-, … , J-shell ionization probability, respectively.

Hereafter, we denote Kα x-rays from atomic states with *m* K-shell vacancies and *n* L-shell vacancies as $\mathrm{K}^m\mathrm{L}^n$ x-rays. In a study by Awaya *et al.* [3], KL^n x-ray intensities from Ti by N-ion impacts were measured and they found that the corresponding experimental KL^n spectra can be explained by the binomial expression shown above.

In this study, the multipleionization processes for a single K-shell electron and up to seven M-shell electrons are considered. Following Eq. (1), cross sections of these processes can be expressed as

$$\sigma_{\mathrm{K},n\mathrm{M}} = \sigma_\mathrm{K} \binom{N_\mathrm{M}}{n} P_\mathrm{M}^{n} (1-P_\mathrm{M})^{N_\mathrm{M}-n} \quad . \quad (2)$$

3. Population Kinetics and Spectral Synthesis

K- or L-shell vacant states are mainly created through inner-shell ionization by heavy ion impacts. In population kinetics calculation, such non-radiative processes as KLL-, KLM-, KMM- and LMM-Auger transitions are considered [4] to estimate net Kα emission. The LMM transitions are for L-shell vacant states.

Population of each state is calculated by solving a rate equation under a collisional radiative equilibrium (CRE) condition. The cross sections of K- and L-shell ionizations by ion impacts are calculated by Rice *et al.* [5] and Hansteen *et al.* [6], respectively. In the calculation of spectral line-shapes, the profiles are convolved by electron impact broadening with a semi-classical expression [7], natural and Doppler broadenings assuming that ion temperature is equal to electron temperature. Calculation of Kα transitions is performed with the use of GRASP92 and RATIP codes [8,9]. These codes are based on a multi-configuration Dirac-Fock (MCDF) method.

4. Calculation Results and Discussion

4.1 Calculation Conditions

In the calculation, target atoms are chlorine in C_2H_3Cl plasma, and it is assumed that an incident ion-beam is a C^{6+} beam, of which beam current density is 3 kA/cm^2, and mean particle energy is 30 MeV with the energy spread of 10% of the mean energy described by Maxwell distribution. The spectra are calculated with and without the multipleionization.

4.2 Spectral Deformation by Multipleionization

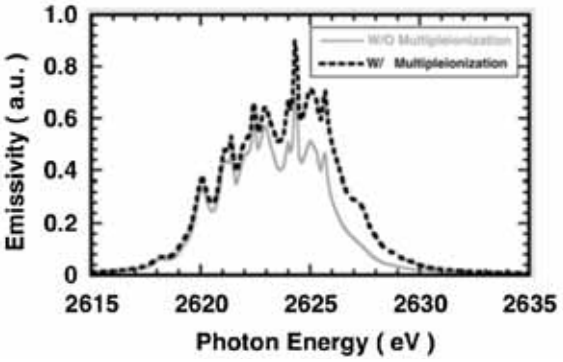

Fig. 1 Calculated Cl-Kα spectra from C_2H_5Cl plasma at ion density $\rho_\mathrm{ion} \approx 8.1 \times 10^{12}$ cm^{-3} (corresponding to solid density $\times 10^{-10}$) at electron temperature T_e = 10 eV with and without multipleionization.

Fig. 1 shows the spectral line-shapes at ion density $\rho_\mathrm{ion} \approx 8.1 \times 10^{12}$ cm^{-3} (corresponding to solid density $\times 10^{-10}$) and electron temperature T_e = 10 eV. With multipleionization, it is clear that Kα lines at photon energy around 2625 eV are enhanced compared with those without multipleionization. According to Ref. [1], Kα lines from $Cl^{2\text{-}4+}$ have peaks around 2625 eV. The enhancement may be due to such charge states of the Kα lines.

The dependence of ion density on spectral line-shapes at electron temperatures T_e = 10 eV and

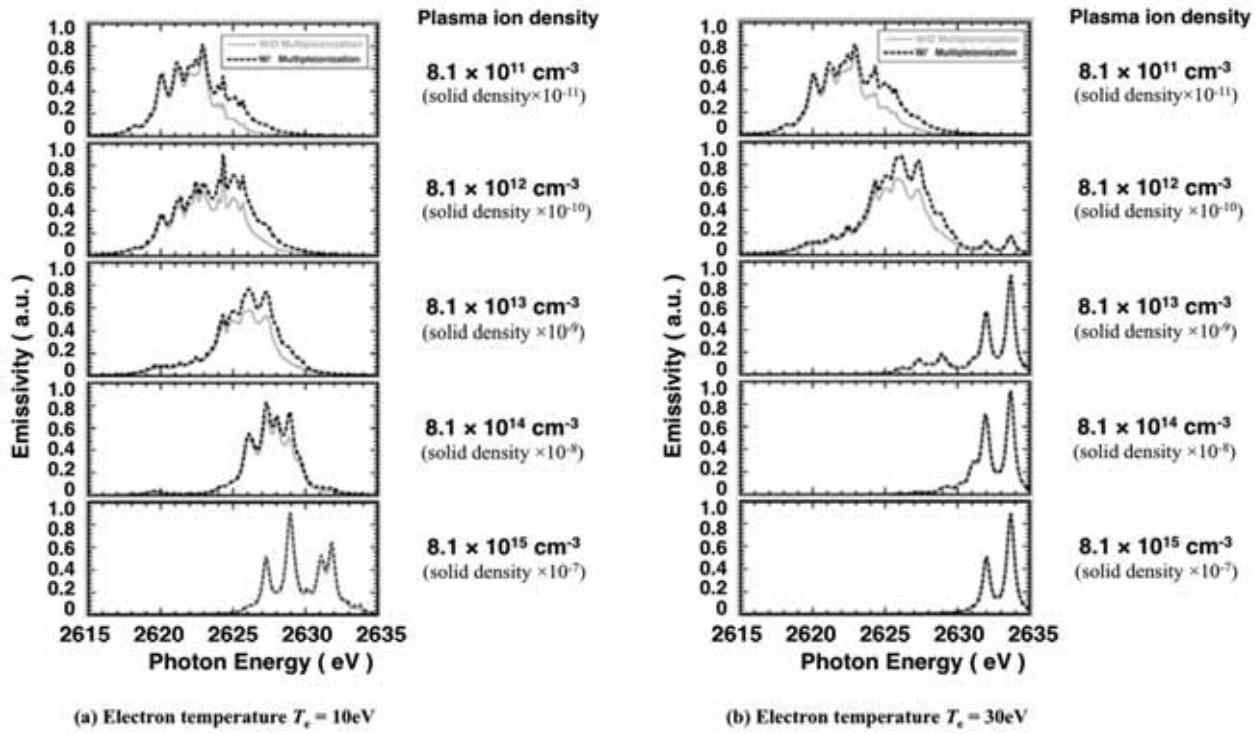

Fig. 2 Calculated Cl-Kα spectra from C_2H_5Cl plasma at electron temperatures (a) T_e = 10 eV and (b) T_e = 30 eV. Solid lines stand for Kα lines with multipleionization, and broken lines stand for those without multipleionization.

30 eV are presented in Fig. 2. We can see that the effects of multipleionization increase as plasma ion density decreases. In the case at electron temperature T_e = 10 eV (Fig. 2 (a)), the multipleionization has an obvious contribution to the line-shape below the ion density of ~10^{14} cm^{-3} (solid density × 10^{-9}), and below the ion density of ~10^{13} cm^{-3} (solid density × 10^{-10}) at T_e = 30 eV (Fig. 2 (b)). These densities are near the incident beam density ρ_{inc} (~10^{12} cm^{-3}). It can be said that the effects of the multipleionization are indispensable when the plasma electron density (roughly equal to plasma ion density in those cases) is near or less than a beam density because multipleionization can compete with outer-shell ionization by electron impacts.

In Fig. 2 (b) (T_e = 30 eV), Kα lines are shifted to a higher energy side compared with those in Fig. 2 (a) (T_e = 10 eV). Generally, an average charge state of target ions is enhanced as plasma temperature increases. The spectral shift is due to such enhancement of an average charge state. In Fig. 2 (b), Kα lines at the ion density $\rho_{ion} > 8.1 \times 10^{13}$ cm^{-3} have peaks around 2630-2635 eV. Such lines are from Cl^{5+}-Cl^{7+} ions [1]. In such temperature and density where the average charge state of target ions is near seven, the number of M-shell electrons of chlorine becomes small, and the multipleionization processes associated L-shell electrons have to be considered.

5. Conclusion

To examine a contribution of the multipleionization associated M-shell electrons to the Cl-Kα lines, the calculations of population kinetics and the Kα spectral synthesis were done under a collisional radiative equilibrium (CRE) condition. With the multipleionization, the Kα lines at a higher energy side are enhanced when the plasma electron density is near a beam ion density.

References

[1] T. Kawamura, K. Horioka and F. Koike, *Laser Part. Beams* **29**, 135 (2011).

[2] J. H. McGuire and P. Richard, *Phys. Rev. A* **8**, 1374 (1973).

[3] Y. Awaya, T. Kambara and Y. Kanai, *Int. J. Mass Spec.* **192**, 49 (1999).

[4] S. Fritzsche, *Phys. Scr.* **T41**, 45 (1992).

[5] R. Rice, G. Basbas, and F. D. McDaniel, *Atomic Data Nucl. Data Tables* **20**, 503 (1975).

[6] J. M. Hansteen, O. M. Johnsen, and L. Kocbach, *Atomic Data Nucl. Data Tables* **15**, 503 (1975).

[7] H. Griem, M. Blaha, and P. C. Kepple, *Phys. Rev. A* **41**, 5600 (1990).

[8] F. A. Parpia, C. Froese Fischer, and I. P. Grant, *Comput. Phys. Commun*. **94**, 249 (1996).

[9] S. Fritzsche, *J. Electr. Spec. Rel. Phenom.* **114-116**, 1155 (2001).

Parameter evaluation of pulsed-power-driven plasma flow using ion current measurement

Taichi Takezaki, Keita Kakinuma, Yutaro Hatakeyama,
Kazumasa Takahashi, Toru Sasaki, and Takashi Kikuchi

Nagaoka University of Technology
Kamitomioka 1603-1, Nagaoka Niigata 940-2188, Japan

ABSTRACT

To evaluate the ion number density of a fast plasma flow generated by a tapered cone plasma focus device, an ion current was measured by using a Faraday cup. The arrival time observed by the Faraday cup is agreement with the estimated arrival time from the streak image. The ion number density was estimated to be 10^{17} m^{-3} from the current peak and the flow velocity. The behavior of the current waveform for the change of the biased voltage indicated that the suppressor voltage was the shielded by the electron potential.

Keywords

Plasma focus device, plasma flow, ion current measurement

1. Introduction

To elucidate the generation processes of high-energy particles in the outer space, understanding interactions between fast plasma flows and electromagnetic fields is required in non-relativistic region. Cosmic rays (CRs) are high-energy particles traveling through the outer space. CRs have the extremely high energy reaching 10^{20} eV, and the non-thermal energy distribution with a power-law spectrum [1]. The particle acceleration processes of CRs are driven by passing through collisionless shocks such as supernova shocks [2-4]. Diffusive shock acceleration (DSA) has explained the statistical acceleration as a non-thermal energy distribution of CRs due to the reflection of charged particles by the induced electromagnetic turbulence around shocks [5-6]. However, to accelerate charged particles by DSA, charged particles obtain the initial energy to get over the potential of the shock transition region for entering DSA [7-9]. Therefore, another particle acceleration mechanisms of charged particles in non-relativistic region has been predicted.

Laboratory scale experiments provides “in-situ” observation of the interaction of fast plasma flow with electromagnetic fields in non-relativistic region [10-19]. We have proposed a tapered cone plasma focus device (TCPFD) for laboratory astrophysics using a pulsed-power discharge [20-21]. The TCPFD produces a fast plasma flow with the quasi-one-dimensional behavior for the easy comparison to numerical simulations. A hybrid particle-in-cell simulation showed the particle acceleration phenomena for the plasma flow generated by the TCPFD [21]. The acceleration mechanisms are predicted the interaction of the one-dimensional fast plasma flow and the external perpendicular magnetic field. To understand the particle acceleration phenomena, both the collisionless condition of the ion-ion collision and the pressure balance between the plasma flow and the magnetic pressure are satisfied. In other words, the plasma flow requires the high kinetic pressure compared with the magnetic pressure, as well as of the low density for satisfying the collisionless condition. Therefore, for applying the suitable magnetic field, the evaluation of the ion number density of the plasma flow is measured.

In this study, to measure the plasma parameter of

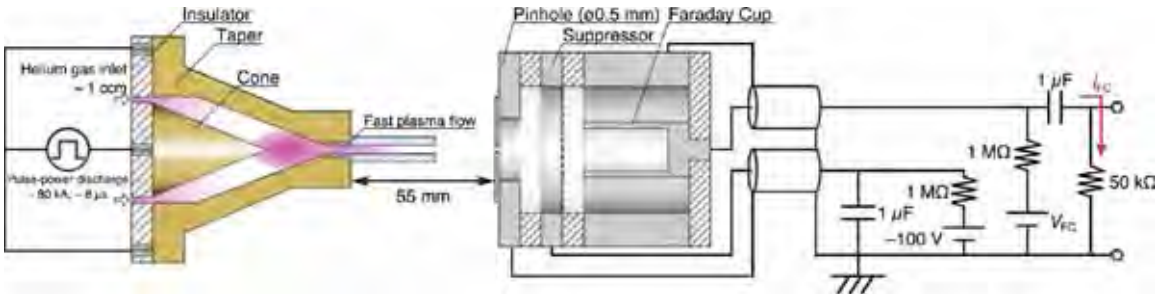

Fig. 1 Schematic image of the TCPFD and the setup for the ion current measurement.

the plasma flow generated by the TCPFD, the ion flow was measured by using a streak camera and a Faraday cup.

2. Experimental Setup

Figure 1 shows a schematic image of the TCPFD and the setup for measuring the ion current waveform using a Faraday cup. The TCPFD consists of an outer tapered electrode, an inner cone electrode, an insulator, and a guiding acrylic tube. The plasma generated by the TCPFD flows into the acrylic tube with a one-dimensional behavior [20-21]. The peak of the discharge current was –80 kA, and the discharge period was 8 μs. Helium gas was supplied between the electrodes with the flow rate of 1 sccm, and the initial pressure of the vacuum chamber was 0.05 Pa.

The Faraday cup were placed at d = 55 mm from the connection point of the tapered electrode and the acrylic tube for measuring the ion current. The Faraday cup consists of an aperture (the diameter of Ø0.5 mm), a meshed suppressor biased at –100 V for reflecting electrons (the opening size of 0.5 mm, the beam transmission of 71 %), and a cup detector. The cup detector was also biased at the positive voltage V_{FC} for evaluating the ion energy. To avoid the dropping voltage at the suppressor and the cup detector, the capacitor provides the charge for keeping the voltages. We observed the change of the current waveform I_{FC} by varying V_{FC}.

3. Results and Discussions

Figure 2 shows the typical streak image of the optical emission of the generated plasma flow. The dotted line indicates the tilt of the optical emission of the plasma. The tilt of the optical emission of the plasma corresponds to the flow velocity. The flow velocity U is estimated to be 27 km/s.

Figure 3 shows the current waveform measured by the Faraday cup. The biased voltage of the cup detector varied in (a) V_{FC} = 0 V, (b) V_{FC} = 5 V, and (c) V_{FC} = 10 V, respectively. The variation of the current waveform starts from 4 ~ 5 μs. The arrival time of the plasma flow to the Faraday cup t_{dec} is estimated as below:

$$t_{dec} = t_{st} + \frac{d}{U} \tag{1}$$

where t_{st} is the start time of the plasma flow. The arrival time is estimated to be t_{dec} ~ 4.7 μs with d = 55 mm, t_{st} ~ 2.7 μs, U ~ 27 km/s, from the streak image. The arrival time of the current fluctuation from the Faraday cup signal agreed with the estimated arrival time of the plasma flow from the streak camera. The result indicates that the measured current corresponds to the plasma flow.

The ion number density is estimated from the measured current waveform. Figure 3(a) shows the maximum ion current peak from the plasma flow because, ideally, most of the electrons are reflected due to the suppressor with –100 V, and all of ions reach to the detector without the positive potential. The positive peak of the measured current shown in Fig. 3(a) is I_{peak} ~ 0.24 mA. The ion number density n_i is estimated as below:

$$n_i = \frac{I_{peak}}{ZeUS} \tag{2}$$

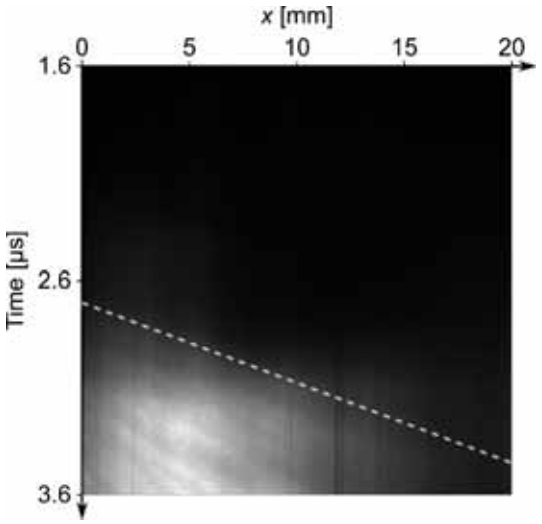

Fig. 2 Typical streak image of the plasma flow.

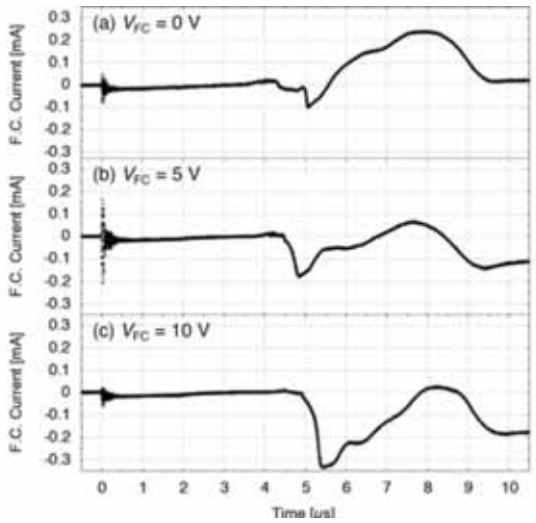

Fig. 3 Current waveform measured by the Faraday cup. The biased voltage of the cup detector V_{FC} is (a) 0 V, (b) 5 V, and (c) 10 V.

where, Z is the ionization degree of the ion, e is the elementary charge, S is the cross section of the aperture of ø0.5 mm. Assuming $Z = 1$, we obtain $n_i \sim 2.8\times10^{17}$ m^{-3}.

Figure 3 showed the decrease of the peak of the current with the increase of the biased voltage of the cup detector. The Debye length λ_D is estimated as below:

$$\lambda_D = \sqrt{\frac{\varepsilon_0 k_B T_e}{e^2 n_e}} \quad (3)$$

where, ε_0 is the permittivity in the vacuum, k_B is the Boltzmann constant, T_e is the electron temperature, and n_e is the electron number density. The electron number density and the electron temperature are assumed to be $n_e = 10^{17}$ m^{-3}, $T_e = 5$ eV [21], respectively. Thus, the Debye length is estimated to be $\lambda_D \sim 53$ μm. The estimated Debye length is shorter than the opening size of the aperture and the suppressor. It means that the negative potential of the suppressor is not able to reflect all of electrons from the plasma flow.

4. Conclusions

We have measured the ion current waveform from the plasma flow generated by the TCPFD. The agreement of the time of the current fluctuation and the estimated arrival time indicated that the measured ion current waveform is the signal from the plasma flow. The ion number density was estimated to be 10^{17} m^{-3} from the current peak and the flow velocity. However, the behavior of the current waveform for the change of the biased voltage indicated the Debye shield of the suppressor voltage for the electrons. Therefore, to exclude the electron flux reaching to the detector, the choice of the opening size of the aperture and the meshed suppressor should be smaller than the Debye length.

We will evaluate the ion energy distribution function using a retarding potential analyzer for investigating the particle acceleration mechanism due to the interaction of the fast plasma flow and the perpendicular magnetic field.

References

[1] S. P. Swordy, “The energy spectra and anisotropies of cosmic rays”, Space Sci. Rev. **99**, 85, 2001.

[2] W. I. Axford, E. Leer, and J. F. McKenzie, “The structure of cosmic ray shocks”, Astron. Astrophys. **111**, 317, 1982.

[3] L. A. Fisk, “On the acceleration of energetic particles in the interplanetary medium”, J. Geophys. Res. **81**, 4641, 1976.

[4] M. A. Lee, “The association of energetic particles

and shocks in heliosphere", Rev. Geophys. Space Phys. **21**, 324, 1983.

[5] A. R. Bell, "The acceleration of cosmic rays in shock fronts - I", Mon. Not. R. Astron. Soc. **182**, 147, 1978.

[6] R. D. Blandford, and J. P. Ostriker, "Particle acceleration by astrophysical shocks", Astrophys. J. **221**, L29, 1978.

[7] G. P. Zank, W. K. M. Rice, J. A. Le Roux, and W. H. Matthaeus, "The injection problem for anomalous cosmic rays", Astrophys. J. **556**, 494, 2001.

[8] Y. Ohira, "Cosmic ray acceleration mechanism", JPS Conf. Proc. **15**, 011002, 2017.

[9] Y. Matsumoto, T. Amano, T. N. Kato, M. Hoshino, "Electron surfing and drift accelerations in a Weibel-dominated high-much-number shock", Phys. Rev. Lett. **119**, 105101, 2017.

[10] R. P. Drake, "The design of laboratory experiments to produce collisionless shocks of cosmic relevance", Phys. Plasmas **7**, 4690, 2000.

[11] D. D. Ryutov, B. A. Remington, H. F. Robey, and R. P. Drake, "Magnetohydrodynamic scaling: From Astrophysics to the laboratory", Phys. Plasmas **8**, 1804, 2001.

[12] A. Stockem, F. Fiuza, A. Bret, R. Fonseca, and L. Silva, "Exploring the nature of collisionless shocks under laboratory conditions", Sci. Rep. **4**, 3934, 2014.

[13] A. Bell, P. Choi, A. Dangor, O. Willi, D. Bassett, and C. Hooker, "Collisionless shock in a laser-produced ablating plasma", Phys. Rev. A **38**, 1363, 1988.

[14] C. Courtois, R. Grundy, A. Ash, D. Chambers, N. Woolsey, *et al*., "Experiment on collisionless plasma interaction with applications to supernova remnant physics", Phys. Plasmas **11**, 3386, 2004.

[15] K. Kondo, M. Nakajima, T. Kawamura, and K. Horioka, "Compact pulse power device for generation of one-dimensional strong shock waves", Rev. Sci. Instrum. **77**, 036104, 2006.

[16] Y. Kuramitsu, Y. Sakawa, T. Morita, C. Gregory, J. Waugh, *et al*., "Time evolution of collisionless shock in counterstreaming laser-produced plasmas", Phys. Rev. Lett. **106**, 175002, 2011.

[17] K. Adachi, M. Nakajima, T. Kawamura, J. Hasegawa, and K. Horioka, "A table-top pulsed power device for counter-streaming plasma experiments", IEEJ Trans. Fundm. Mater. **135**, 366, 2015.

[18] T. Morita, Y. Sakawa, Y. Kuramitsu, S. Dono, H. Aoki, *et al*., "Characterization of electrostatic shock in laser-produced optically-thin plasma flows using optical diagnostics" Phys. Plasmas **24**, 072701, 2017.

[19] J. S. Ross, D. P. Higginson, D. Ryutov, F. Fiuza, R. Hatarik, *et al*., "Transition from collisional to collisionless regimes in interpenetrating plasma flows on the national ignition facility", Phys. Rev. Lett. **118**, 185003, 2017.

[20] T. Sasaki, H. Kinase, T. Takezaki, K. Takahashi, T. Kikuchi, *et al*., "Laboratory scale experiments for collisionless shock generated by taper-cone-shaped plasma focus device" JPS Conf. Proc. **1**, 015096, 2014.

[21] T. Takezaki, K. Takahashi, T. Sasaki, T. Kikuchi, and N. Harada, "Accelerated ions from pulsed-power-driven fast plasma flow in perpendicular magnetic field", Phys. Plasmas **23**, 062904, 2016.

Energy Evaluation of Pulsed Heavy Ion Beam Accelerated in 1-stage gap of Bipolar Pulse Accelerator

Tarou Honoki, Masashi Terada, Hiroaki Ito

Graduate school of science and engineering for education , University of Toyama, Toyama 930-8555, Japan

ABSTRACT

We have developed a prototype of bipolar pulse accelerator (BPA), which can generate an intense pulsed ion beam with higher purity than the conventional ion diode. The BPA is operated with the bipolar pulse voltage and is a two-stage electrostatic accelerator. A coaxial gas puff plasma gun was used as an ion source, which was installed inside the grounded anode. We found that the ion beam was successfully accelerated in the 1st and 2nd gaps by applying the bipolar pulsed voltage to the drift tube. However, the evaluation of the ion energy via time of flight is not enough to demonstrate the principle of the BPA. Therefore, in order to evaluate the characteristics of the accelerated ion beam, we used a solid track detector (CR-39) with multi-step etching technique. In this study, we evaluated the ion energy by measuring ion range in CR-39. The energy of the nitrogen ion was estimated to be 94±42 keV.

Keywords

Intense Pulsed Heavy Ion Beam, Bipolar Pulse Accelerator; Magnetically Insulated Ion Diode, Plasma Gun

1. Introduction

Pulsed heavy ion beam (PHIB) is generated by using a high voltage and high power pulse generation technique called pulse power technology. The PHIB is applied to the surface treatment technology such as ion implantation and annealing [1-5]. In particular, it is expected that puled ion implantation can be applied to a next generation semiconductor materials including such as silicon carbide (SiC) and diamond. Furthermore, the pulsed nitrogen ion beam which is an n-type dopant is required to have an energy of ~200 keV, an ion current density of ~50 A/cm^2 and a pulse duration of ~100 ns.

A number of PHIB sources have been developed so far for the requirements of research and industrial application [6,7]. The producible ion species, however, is limited to the material of electrode (anode), since the anode plasma is produced by a high-voltage flashover and an electron bombardment to the anode surface. In addition, the purity of the PHIB is usually deteriorated by absorbed matter on the anode surface and residual gas molecules in the diode chamber [8]. Therefore, the conventional PHIB is not suitable for various applications to material processes.

It is very important for the application of PHIBs to the semiconductor implantation to develop the PHIB technology to generate high-purity ion beams with useful ion species for donor and acceptor in SiC such as nitrogen, phosphorous, boron and aluminum. In order to improve the purity of the intense pulsed ion beam, we have developed a prototype of a new accelerator named “bipolar pulse accelerator (BPA)” [9, 10]. It was confirmed that the ion beam was successfully accelerated in the 1st and 2nd gaps by applying the bipolar pulsed voltage. However, the evaluation of the ion energy via time of flight is not enough to demonstrate the principle of the BPA. We estimated the energy of the ion beam by measuring ion range in a solid track detector, CR-39. This paper reports the experimental results on the energy

evaluation of the pulsed ion beam accelerated by the bipolar pulse.

2. Experimental Apparatus

Figure 1(a) shows the schematic configuration of the BPA in the present experiment. The system consists of a bipolar pulse generator and an accelerator. The bipolar pulse generator consists of a Marx generator and a pulse forming line (PFL). The designed output of the bipolar pulse generator is the negative and positive pulses of voltage ±200 kV with pulse duration of 70 ns each. In the system, the double coaxial type is employed as the PFL for the formation of the bipolar pulse. The line consists of three coaxial cylinders with a rail gap switch on the end of the line, which is connected between the intermediate and outer conductors. The characteristic impedance of the line between the inner and intermediate conductors and one between the intermediate and outer conductors are 6.7 Ω and 7.6 Ω, respectively. The PFL is charged positively by the low inductance Marx generator with maximum output voltage of 300 kV through the intermediate conductor. The rail gap switch is filled with pure SF_6 gas and the pressure can be adjusted to control the optimum trigger timing.

Figure 1(b) shows in detail the acceleration gap design and experimental setup of the BPA, which consists of a grounded anode, a drift tube, a grounded cathode and two magnetically insulated acceleration gaps with gap length of d_{AK}=15 mm each. The anode and the cathode are the copper electrodes of diameter 78 mm, thickness 5 mm. The electrodes are uniformly drilled with apertures of diameter 4 mm, giving beam transmission efficiency of 58 %. In order to produce magnetic fields for suppression of the electron flow in both acceleration gaps, a magnetic field coil of grating structure is used and installed on the rectangular drift tube. The uniform magnetic field with strength of 0.3-0.4 T is produced in direction transverse to the acceleration gap by a capacitor bank with capacitance of 500 μF and charging voltage of 4 kV. To obtain higher transmission efficiency of the ion beam, right and left sides of the coil consist of 8 blades each and have a grating structure. Each of the blades (10 mm^W x 118 mm^L x 1 mm^T) is connected in series and works as an 8-turn coil. Since at peak of the magnetic field, the bipolar pulse voltage is applied to the drift tube, the pulsed current produced by the capacitor bank is applied to the magnetic coil through an inductively isolated current feeder.

A gas puff plasma gun, which consists of a gas puff valve and a coaxial plasma gun, was used as the ion source and installed inside the anode as shown in Fig. 1(b). The vessel of the gas puff is filled with N_2 gas. When the pulsed current is applied to the drive coil of the gas puff by discharging the capacitor bank with capacitance of 5 μF and charging voltage of 6 kV, the valve of the gas puff is opened and the filled N_2 gas is injected into the plasma gun. The ion source plasma is produced by discharging the capacitor bank with capacitance of 1.5 μF and charging voltage of 15 kV at the optimum timing.

The charging voltage of the PFL (V_{PFL}) and the output voltage (V_0) of the bipolar pulse were measured by the resistive voltage divider placed near the rail-gap switch, respectively. The ion current density of the

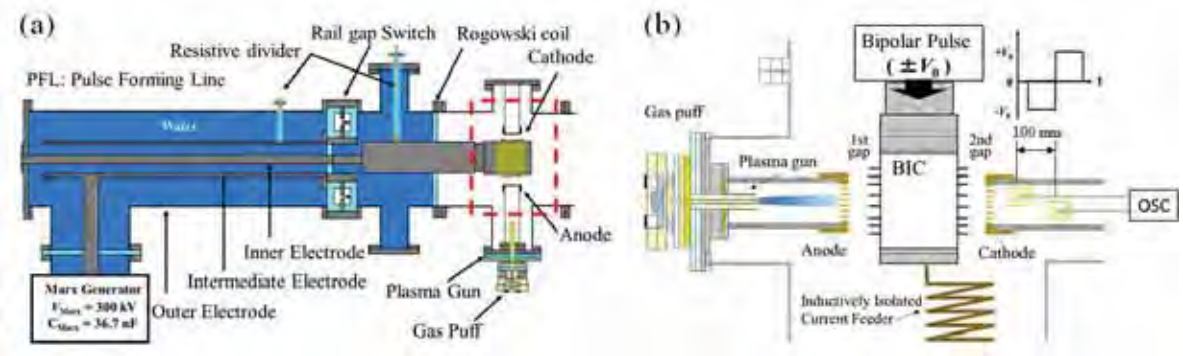

Fig. 1 (a) Schematic configuration and (b) acceleration gap design and experimental setup of BPA.

pulsed ion beam was measured by a biased ion collector (BIC) placed inside the drift tube and the cathode.

3. Energy Evaluation of Ion Beam by solid track detector

We used a solid track detector CR-39 as an evaluation of the ion speacies and energy of the accelerated ion beam. The CR-39 is a plastic material developed as an optical material, and it is used in varius fields such as cosmic ray measurement, emission particle measurement at fusion , and neutron dosimeter. When ions pass through CR-39, the chemical bond in the medium is broken by the interaction, and a specific damage called a track occurs along the ion trajectory. The track core size and formability formed by the irradiation of the charged particles are incident depend on the stopping power of the material, ion species, valance, and ion velocity. After ion iraddiation, ion track region is removed by chemical etching treatment.Therefore, in order to evaluated the ion energy, the range of ions was calculated by multi-step etching technique for observing the growth of the track by performing etching treatment in multiple stages in several hours in order to evaluated ion energy [11].

Figure 2 shows an etch pit forming process in a multi-step etching technique, where R_0 is the range, r is the pit radius, l is the maximum depth, and G is the bulk etch, i.e., the thickness of layer removed,. When etching with a strong alkali aqueous solution, it is etched in a spherical wavefront shape according to the Huygens's theorem, but the range region is removed fasteer than the part with little damage, and it is continuned with a conical shape (dash line in Fig.2). After the tip of the etch pit reaches the end of the track, the etching is continued until the wall of the pit becomes a round-out state (solid line in Fig.2), where the wall surface becomes the spherical surface. In the figure, point A , B and C show the track end point, the etch pit center after he round-out, and the etch pit opening, respectively. Based on the etch pit growth curve, the etch pit radius r and the range R_0 are expressed by the following equation

$$r^2 = 2lG - 2R_0l + l^2 \quad (1)$$

$$R_0 = G + \frac{1}{4}\left(\frac{dr^2}{dG}\right) - \frac{r^2}{\left(\frac{dr^2}{dG}\right)} \quad (2)$$

where dr^2/dG is slope of the squared radius against the bulk etch (G). Equation (2) shows that we can obtain the projected range R_0 by plotting the squared radius as a linear function of the bulk etch. On the other hand, the simulation software (Stopping and Range of Ions in Matter: SRIM) cam calculate the dependence of the ion stopping range in material on the ion energy. Figure 3 shows the stopping range of hydrogen and nitrogen ions in CR-39 as a function of ion energy calculated by SRIM. For example, when ions with energy of 200 keV are irradiated on CR-39, the ion stopping range of nitrogen ion is about 0.63 μm. The ion energy is estimated by comparing the ion range obtained by the experimental results with the SRIM results.

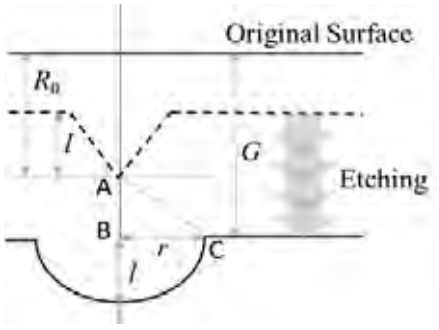

Fig. 2 Etch pit profile after round-out

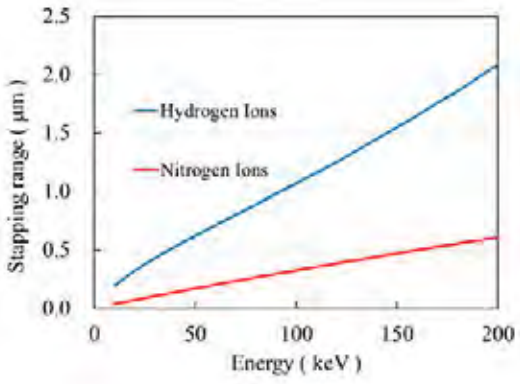

Fig. 3 Ion range of H^+ and N^+ in CR-39 as a function of energy obtained by SRIM code

4. Experimental Results and Discussion

In order to measure the ion range and energy of ion beam accelerated by BPA, CR-39 was irradiated with a pulsed nitrogen ion beam in the 1st accelerating gap. The experimental setup is shown in Fig. 4. CR-39 used in the experiment is HARZLAS TNF-1 manufactured by Fukuvi Chemical Industry Co., and the detection threshold for protons is set at ~27 MeV [12]. Since the pulsed ion beam has high fluence, the ion fluence is limited by two pinholes to reduce the overlap of the ion track on CR-39. The beam diameter on the detector is determined by the two pinhole diameters D_1, D_2, the distances L_1 between two pinholes, and the distance L_2between the pinhole and CR-39. Setting to be $D_1 = D_2 = 0.3$mm, L_1=40 mm and L_2=20 mm, respectively the beam diameter becomes

$$D_3 = D_2\left(1 + \frac{L_2}{L_1}\right) + D_1\frac{L_2}{L_1} = 0.6 \text{ mm}. \qquad (3)$$

Figure 5 shows an optical microscopic image for the etched CR-39 detector after etching time of 45 minutes. The etching rate kept constant at 40 nm/min (2.4 μm/h) by 5mol/L-NaOH aqueous solution with the temperature of 60±2℃. The Marx generator for the bipolar pulse was operated at 60 % of the full charge condition. On this condition, the bipolar pulse with voltage of about -136 kV, +89 kV and pulse duration of about 70 ns (FWHM) was applied to the drift tube and the diode current of about -12 kA and +4 kA was observed. It was found from Fig.5 that three particle groups are observed. Since the nitrogen ion source is used in this experiment, it is considered that the nitrogen ion is dominant in the ion beam. Thus, the ion beam consists of the nitrogen ion and impurity ion. Note that the maximum observable fluence on CR-39

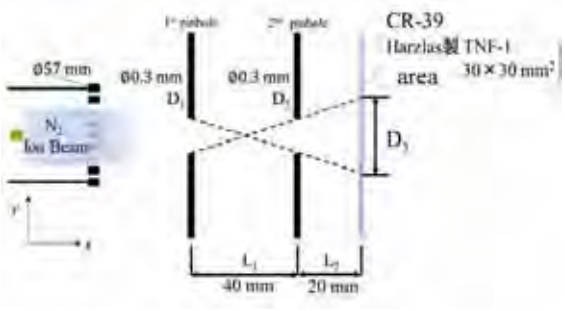

Fig. 4 Experimental setup for measurement of ion range

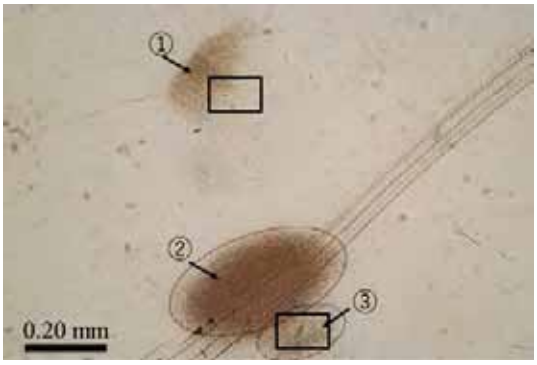

Fig. 5 Optical microscopic image of ion track pattern after etching time of 45 min

would be limited below 10^5 ions/cm2 under the optical microscope, because of the etch pits overlapping. Therefore, we could not carry out the precise measurement of etch pit radius at the beam center. We measured the etch pits at beam halo, which is shown in the rectangular in Fig. 5.

Figure 6 shows an optical microscopic image of group ① in Fig.5 after etching time of 120 minutes. As can be seen in Fig. 6, the etch pit is composed of two circles with different diameters and the smaller etch pit is uniformly distributed. These results show that ions are perpendicularly incident in CR-39. Figure 7 shows the typical optical microscopic image of the etch pits at different etching time. In the present analyses, we will pay special attention on the numbered etch pits as #1, #2 and #3. As shown in Fig.7, it turns out that the diameter increases with the progress of the etching. We measured the dependency of the radius of the etch pit on the etching time, i.e., the bulk etch *G*.

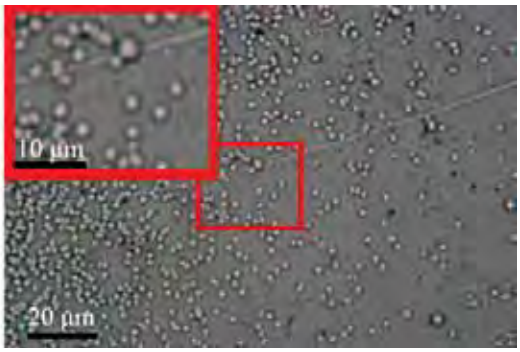

Fig. 6 Optical microscope image of etch pits for group ① in Fig.5 after etching time of 120 min

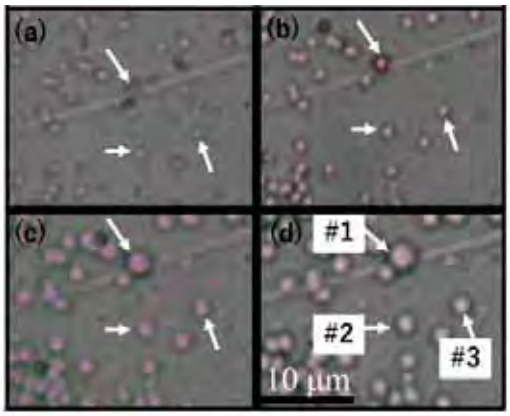

Fig. 7 Optical microscope image of etch pits for inset of Fig.6 as a function of etching time (a) 42 min, (b) 60 min, (c) 90 min and (d) 108 min.

Figure 8 (a) shows profiles of the etch pit radius as a function of the bulk etch (*G*), i.e., etch pit growth curves, for #1, #2 and #3. As shown in Fig.8 (a), the slopes for the curves increase gradually. These are caused by the dependence of the track etch rate around the Bragg peaks on the depth. In the deeper etching, the curves begin to saturate. This shows the start point of the spherical phase. Figure 8 (b) shows profiles of the squared radius r^2 as a function of the bulk etch *G*. As shown in Fig.8 (b), all etch pit growth curves have straight sections after the bulk etch of 1 μm, which shows that all etch pits were round out after this bulk etch. The slope of the squared pit radius against the bulk etch was obtained by the least squared fitting as shown in Fig. 8 (b) with broken lines.

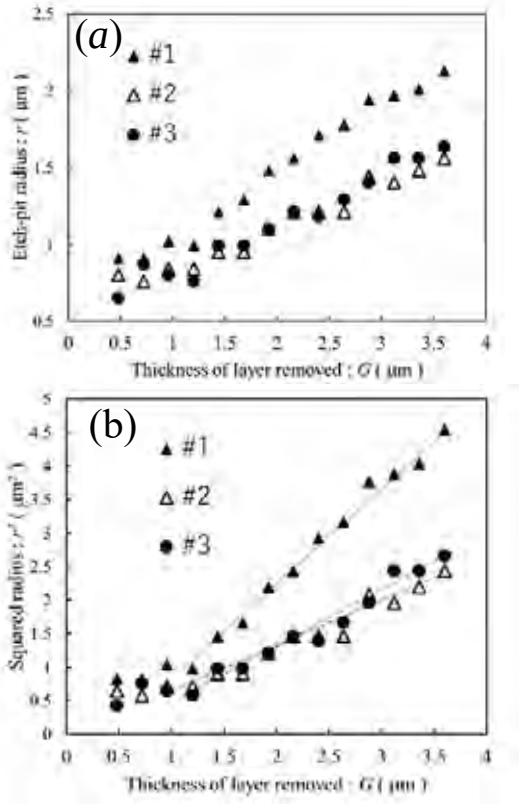

Fig. 8 Etch pit growth curve with multi-step etching for numbered etch pit. Profile of (a) etch pit radius and (b) squared radius

Figure 9 shows profiles of the squared radius r^2 as a function of the bulk etch (*G*) for group ③ shown in Fig.5. The plot is the average value of the variation of the growth for 3 etch pits. The error bar indicates the maximum and the minimum values. It can be seen from Fig.8 and Fig.9 that the radius of the etch pit is slightly smaller than the pits of # 2 and # 3 in the particle group of ①. As shown in Fig. 3, the range of nitrogen ion is smaller than that of hydrogen ion at the same energy. In addition, considering that the nitrogen ion source is used in this experiment, the pulsed ion beam consists of the dominant nitrogen ion and impurity ion. Therefore, we found that the ion specie in group ② and ③ is nitrogen ion and group ① is impurity ion. The projected range of the nitrogen ion is calculated to be 0.30 ± 0.13 μm by using the slope of the squared pit radius against the bulk etch in Fig.9 and Eq. (2). Then, the energy of the nitrogen ion is estimated to be 94±42 keV with SRIM code. The maximum ion energy was in reasonable good agreement with the acceleration voltage, i.e., 1st pulse

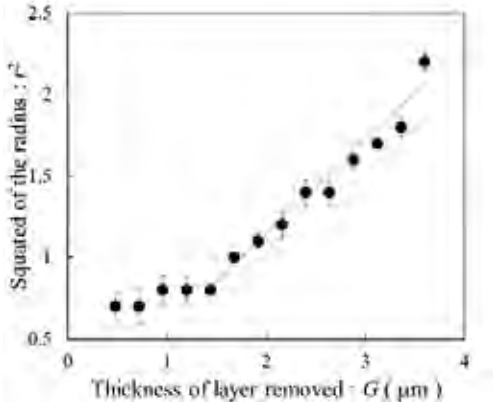

Fig. 9 Profiles of the squared radius r^2 as a function of bulk etch *G*

(negative pulse) voltage of the bipolar pulse.

5. Conclusions

We have developed a prototype of the accelerator to perform proof of principle experiments on the BPA. In this study, the energy of the pulsed heavy ion beam has been evaluated by a solid track detector (CR-39) with multi-step etching technique. The energy of the nitrogen ion was estimated to be 94±42 keV by measuring ion range in CR-39. We are planning to evaluate the energy of the pulsed ion beam accelerated in 2nd-stage by the bipolar pulse in detail by using this method to confirm the principle of the BPA. In addition, we need to optimize the beam quality by modifying the gap structure to increase the beam current.

Acknowledgement

This work was partially supported by JSPS KAKENHI Grant Number JP 15H03961.

References

[1] K. Yatsui *et al.* : "Applications of intense pulsed ion beam to materials science", Phys. Plasma, Vol.1, No.5, pp.1730-1737 (1994).

[2] H. Akamatsu, *et al.* : "Surface treatment of steel by short pulsed injection of high-power ion beam", Suf. Coat. Technol., Vol.136, pp.269-272 (2001).

[3] Y. Nakagawa et al., "Modification of solid surface by intense pulsed light-ion and metal-ion beams", Nucl. Instrum. Method B, Vol.39, pp.603-606 (1989).

[4] G. P. Johnston et al., "Preparation of diamondlike carbon films by high-intensity pulsed-ion-beam deposition", J. Appl. Phys., Vol.76, No.10, pp.5949-5954 (1994).

[5] J. Khamsuwan et al., "High-energy heavy ion beam annealing effect on ion beam synthesis of silicon carbide", Surface & Coatings Technology, Vol.206, pp.770-774 (2011).

[6] Y. Hashimoto et al., "Generation and focusing of intense ion beam with an inverse pinch ion diode", Jpn. J. Appl. Phys., Vol.31, pp.1922-1927 (1992).

[7] X. P. Zhu et al., "Characterization of a high-intensity bipolar-mode pulsed ion source for surface modification of materials", Rev. Sci. Instrum., Vol.73, pp.1728-1733 (2002).

[8] K. Masugata et al., "Diagnosis of high-brightness ion beams produced in point pinch diodes", J. Appl. Phys., Vol.80, pp.4813-4818 (1996).

[9] K. Masugata et al., "Development of bipolar-pulse accelerator for intense pulsed ion beam acceleration", Nucl. Instrum. & Methods in Phys. Res. A, Vol.535, pp.614-621 (2004).

[10] H. Ito et al., "Bipolar pulse generator for intense pulsed ion beam accelerator", Rev. Sci. Instrum., Vol.78, 013502 (2007).

[11] M.Kanasaki, A. Hattori, H.Sakaki, and Y.Fukuda : "A high energy component of the intense laser-accelerated proton beams detected by stacked CR-39", Radiation measurements, Vol.50, pp.46-49(2013).

[12] K.Ogura, M.Asano, N.Yasuda, M.Yoshida : "Properties of TNF-1 track etch detector", Nucl. Instrum. B, Vol.185, pp.222-227 (2001).

Effect of Electrode Shape and Resonance Cavity on Microwave Power in Axially-Extracted Vircator

Tsukasa Nakamura, Fumiya Niwa, Hiroaki Ito

Graduate school of science and engineering for education , University of Toyama, Toyama 930-8555, Japan

ABSTRACT

The virtual cathode oscillator is one of most promising high-power microwave sources. The vircator has the attribute of high-power capability, wide frequency tuning ability, and conceptual simplicity, whereas it has difficult problems in low efficiency and frequency stability. To improve those problems, experiments have been performed in an axially extracted virtual cathode oscillator with a resonant cavity. We present the experimental results on the effect of the cathode shape on the efficiency and microwave power. Three types of shape are a solid, a hollow, and a Rogowski cathodes, all of which are made from aluminum. The microwave with a maximum output power of about 130 MW was observed with the Rogowski type cathode when the diode voltage and diode current are 330 kV and 9 kA, respectively. In addition, the numerical simulation using MAGIC have been carried out and the results were in almost agreement with the experimental results.

Keywords

High-power microwave, virtual cathode oscillator, vircator, resonant cavity, pulsed power technology

1. Introduction

The high power microwaves sources play a significant role in a variety of applications such as particle accelerators, magnetic confinement fusion, astronomy, communications, and various industrial fields [1,2]. A number of high-power microwave sources have been developed. The vicator is attractive due to its high-power capability, device simplicity, and frequency tunability, whereas relatively low efficiency (typically about 3%) of beam-to-microwave power conversion and wide frequency bandwidth are its common disadvantage [1-3]. In order to improve the conversion efficiency and narrow the output frequency, introducing a resonant feedback into the system, one could gain the enhanced efficiency and single frequency operation [4-9]. The vircator placed into a resonator whose natural frequency is close to the virtual cathode oscillator frequency attains the above resonant feedback. However, the best efficiency is up to 10%–12% and an order of magnitude less than that of other high-power sources [7-9].

The experiments has been performed using an axially extracted vircator with the resonant cavity, which was installed by inserting a movable disc plate with an extraction window in the drift space. The choice of the mode is an important consideration in the design of the drift space. In addition, The electrode structure for an intense electron beam plays an important role in the output power and frequency of microwaves emitted from the vircator. In this paper, we report the results on the influence of cathode shape and the resonant cavity structure on the output microwave power and frequency. In addition, the characteristic of the microwave was evaluated by the numerical simulation using MAGIC.

2. Principle of Vircator

The microwave generation process in vircators can generally be explained by two dynamical mechanisms. The first mechanism is electron reflection between the real and virtual cathodes. When the injected electron beam current exceeds the space charge limited current

in drift region, a virtual cathode is formed and most of the electrons in the beam are reflected back. The microwave frequency is given by approximately the electron bounce frequency between the real and virtual cathodes. The other is oscillation of the virtual cathode itself, in which the potential oscillates because of inherent instability of the electron cloud in time and space. The second mechanism is oscillation of the virtual cathode itself, in which the potential oscillates because of inherent instability of the electron cloud in time and space. The oscillation frequency varies from the relativistic beam plasma frequency to 2.5 times the relativistic beam plasma frequency as the injected current increases from the space charge limited current to several times the space charge limited current. The radiation frequency from a vircator is determined both by the reflected electrons due to the virtual cathode and by virtual cathode oscillation. These two oscillation frequencies are fundamentally determined by the geometric structure, the applied voltage and the electron beam parameter.

3. Experimental Setup

Figure 1 shows a schematic configuration of the pulse power system for the axially-extracted vircator used in this study. The pulse power system consists of a Marx generator, a single pulse forming line (PFL), a gas SF_6 spark gap and a pulse transmission line. The Marx generator is the maximum output of 800 kV and the stored energy of 5 kJ at a charging voltage of 50 kV. The PFL is filled with the deionized water as a dielectric. The designed parameters of the PFL are characteristic impedance of 3 Ω, and electrical length of 50 ns. In this experiment, the pulsed power system was operated in negative-output mode and the charging voltage of Marx generator was set to 24 kV and to operate in a single-shot mode.

Figure 2(a) shows the schematic structure of the axial vircator and the microwave measurement setup. The high-voltage pulse generated from the pulsed power system is applied to the cathode of the electron beam diode. A vacuum explosive electron emission diode was used to generate an intense relativistic electron beam. As shown in Fig.2(b), we tested three types of a solid plane, a hollow, and a Rogowski cathodes, which are made from aluminum. A stainless-steel meshed anode with a transparency of ~65% was used. To improve the microwave efficiency and control the output frequency, the resonant cavity was constructed by placing a movable reflection plate for a microwave with a center hole at the distance away from an anode. The output microwave was measured when changing the distance to analyze the resonator effect. From previous experimental results, the AK gap was set to be 8 mm regarding small shot-to-shot variations and good durability of the meshed anode.

The microwave from the vircator traveled along a circular waveguide of 100 mm in diameter and 375 mm in length and is emitted into a free space through an acrylic window. All microwave measurements were carried out with the receiving antenna placed at a distance of 0.7 m away from the vircator window. The open ended rectangle waveguide (WR187: 4.75 × 2.22 cm^2) is utilized as the receiving antenna. The temporal waveform of the output microwave was obtained by using a crystal diode and recorded by a digital

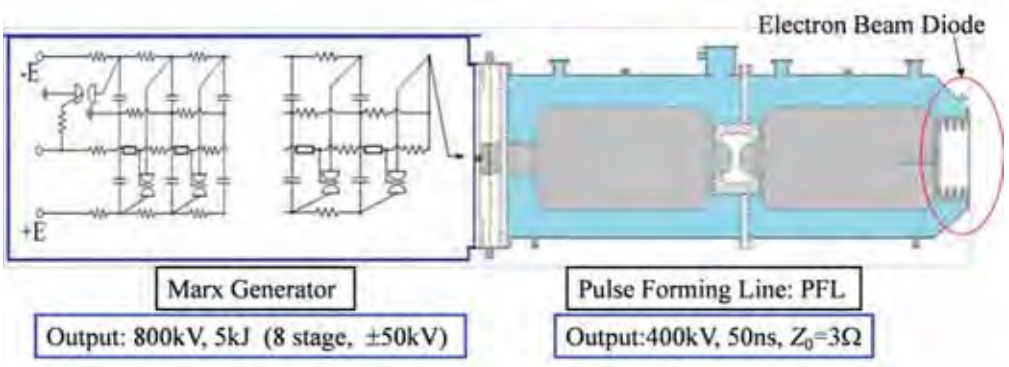

Fig.1 Schematic diagram of Pulsed Power system

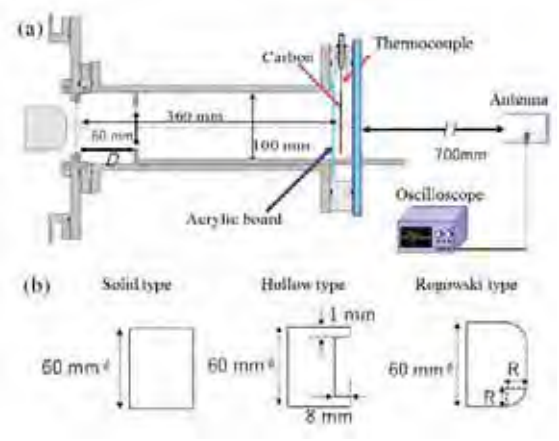

Fig. 2 (a) Schematic structure of axially extracted vircator and microwave measurement setup and (b) three types of cathode tested in this experiment

oscilloscope with a bandwidth of 200 MHz and a sampling rate of 2 GS/s, together with the beam parameters (voltage and current). In order to carry out Fourier transforms, the signal from the antenna was also recorded by a high-speed digital oscilloscope with a sampling rate of 40 GS/s through a coaxial RF cable. The radiated energy of the microwave was measured with a calorimeter, which consists of carbon absorber with 60 mm diameter and 1.5 mm thickness and a K type thermocouple.

A resistive $CuSO_4$ voltage divider was used to measure the output voltage (V_{PFL}) of the pulsed power system and placed at the edge of PFL. The diode voltage (V_d) applied to the cathode is calculated by the inductive correction, since the inductance of the transmission line from the resistive divider to the cathode is ~100 nH. The diode current (I_d) and the

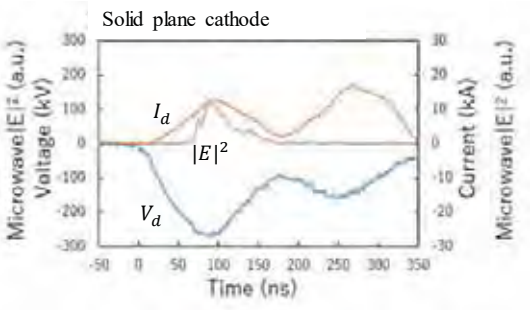

Fig. 3 Typical waveforms of diode voltage V_d, diode current I_d and electric field of microwave with solid type cathode and no cavity

beam current (I_b) passed through the anode were monitored by Rogowski coil at the upstream and downstream of the anode.

4. Experimental Results

Figure 3 shows the typical waveforms of the diode voltage V_d, the diode current I_d and the electric field $|E|^2$ of the microwave with the solid plane cathode and no resonant cavity. The diode voltage increases up to 270 kV within 100 ns and the diode current rises with the diode voltage and has a peak of 13 kA. The microwave is emitted at the rise time of V_d.

Figure 4(a) shows the electric field of the microwave recorded by the high-speed digital oscilloscope for each cathode type. It turns out seen from the figure that the signal with the Rogowski type cathode was consistently higher than the solid and hollow types. In the case of Rogowski type, the signal tends to increase as the curvature R becomes larger. Figure 4(b) shows the Fast Fourier transform (FFT) of the signal shown in Fig 4(a). One can see that for the solid and Rogowski types, microwave frequencies lie between 5.5 and 7 GHz and more than one frequency components have been excited, whereas the hollow type has the frequency range of 4.7–5.5 GHz and a peak at around 5 GHz. The main frequency components of the microwave for the solid type cathode can be identified as 6 and 6.5 GHz. This result indicates that two mechanisms of microwave radiation exist together, namely, the electron reflex between the

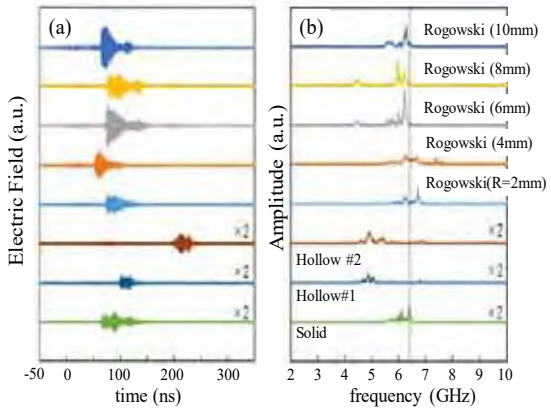

Fig. 4 Typical waveforms of microwave electric field and FFT of microwave E-field shown in Fig.4(a) for 3 types of cathode

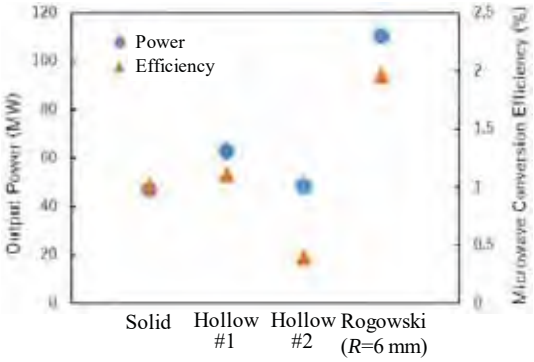

Fig. 5 Microwave peak power and efficiency for each cathode type

real and virtual cathodes as well as the virtual cathode oscillation. It is considered that the low frequency is related to the virtual cathode oscillation, while the high frequency corresponds to the electron reflex process. The frequency for the Rogowski type tends to shift to the low side with an increase of the curvature.

Figure 5 shows the microwave peak power and the efficiency of beam-to-microwave power conversion for each cathode type. The peak power (P) and the efficiency (η) are evaluated by the next equations

$$P = {}^{Q}/_{\tau}$$

$$\eta = \frac{Q}{\int (V_d \times I_d) \mathrm{d}t} \times 100,$$

where Q and τ are the radiated energy of the microwave measured by the calorimeter and full width at half maximum of the microwave pulse, respectively. As shown in Fig.5, the Rogowski type with the curvature of R=6 mm has the microwave power of 110 MW and the efficiency of 2 %, which is two times higher than other cathode types. Figure 6(a) shows the experimental result on the dependence of the peak microwave power and the efficiency on the curvature. Each dotted line in Fig. 8 shows the value of the microwave power and the efficiency for the solid type. It is seen from Fig. 6(a) that as the curvature increases, the power increases and reaches a peak of 110 MW at R=6 mm as the curvature increases, whereas the efficiency gradually increases and has a value of 2.4%.

The numerical simulation was carried out for the vircator with the Rogowski type cathode to confirm the experimental results described earlier. The simulation tool is the well-known “MAGIC” code, which is a 2 1/2-dimensional particle-in-cell (PIC)

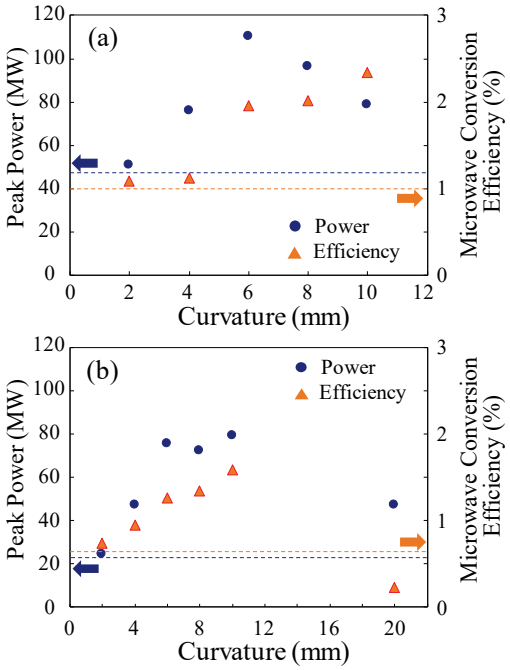

Fig. 6 Peak power and efficiency as a function of Rogowski cathode curvature
(a) in experiment and (b) in simulation

code. Figure 6(b) shows the numerical result on the dependence of the peak microwave power and the efficiency on the curvature. We found that the numerical result has the almost same tendency as the experiment, though there are some differences in the power between those results. In the experiment, the power has a peak at R= 6 mm, while in the simulation, the power increases with an increase from R=2 mm to R=10 mm, but has no peak. This is likely due to the increase of the microwave pulse duration observed in the experiment. In the simulation at the curvature of 20 cm, both power and efficiency drop dramatically.

A resonant cavity was installed in the vircator using the Rogowski type cathode with the curvature of R=10 mm. The vicator attains a resonant feedback when a natural frequency of the resonator, which depends on its structure, is close to the vircator frequency. Figure 7(a) and (b) show the electric field of the microwave and FFT result of the microwave E-field shown in Fig. 7(a) for various resonator length, respectively. The diameter of aperture on the reflector is set to be 6 cm. One can see from Fig. 7(b) that the frequency spectrum has sharp peak by installing the resonator. The

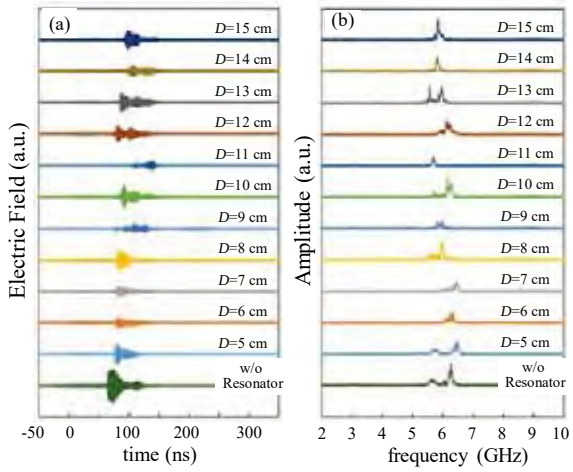

Fig. 7 Typical waveforms of microwave electric field and FFT of the microwave E-field shown in Fig.7(a) as a function of resonator length

microwave frequency tends to shift to the low side as the resonator length increases.

Figure 8 shows the microwave peak power and the efficiency when varying the length of the resonator from 5 to 15 cm. Each dotted line in Fig. 8 shows the value of the microwave power and the efficiency without the resonator. As seen in Fig.8, the peak power and the efficiency greatly change depending on the change of the resonator length and the maximum power of ~130 MW is obtained at the resonator length of 5 cm. One can see that at the resonator length of 5 mm and 15 cm, the peak power is larger than when without the resonator, while the efficiency cannot be improved. The result implies that the resonant feedback did not work well. We consider that the oscillated microwave did not well interact with the microwave reflected by the resonator because the

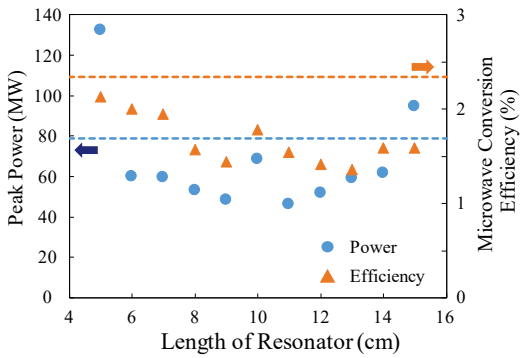

Fig. 8 Peak power and efficiency as a function of resonator length

aperture diameter on the reflector was too large.

5. Conclusions

In this study, we have investigated the influence of the cathode shape and the resonant cavity on the characteristic of the output microwave emitted from an axially extracted vircator to improve the peak power and the efficiency. Both peak power and efficiency of the vircator have been improved by about 2.3 times by changing a solid cathode to a Rogowski type one. By installing the resonator with a length of 5 cm and an aperture diameter of 6 cmin the virtcator with Rogowski type of a curvature R=10 mm, the microwave power increased by 1.7 times to 130 MW. In the future, we plan to redesign the resonator for improvement of the efficiency of the vircator.

References

[1] S. H. Gold and G. S. Nusinovich, “Review of high-power microwave source research,” Rev. Sci. Instrum., vol. 68, pp. 3945–3974 (1997).

[2] J. Benford, J. Swegle, and E. Schamiloglu, “High Power Microwaves” 3rd ed., New York: Taylor & Francis (2016).

[3] R. J. Barker and E. Schamiloglu, Eds., “High-Power Microwave Sources and Technologies”, New York: Wiley-IEEE Press (2001).

[4] J. Benford, et al., “Interaction of a vircator microwave generator with an enclosing resonant cavity,” J. Appl. Phys., vol.61, p.2098 (1987).

[5] Y. Chen, et al.,“Cathode and anode optimization in a virtual cathode oscillator,” IEEE Trans. Dielectr. Electr. Insul., vol.14, pp.1037–1044 (2007).

[6] V. Baryshevsky, et al., “Experimental study of an axial vircator with resonant cavity,” IEEE Trans. Plasma Sci., vol.43, pp.3507–3511 (2015).

[7] G. Z. Liu, et al., “Coaxial cavity vircator with enhanced efficiency”, J. Plasma Phys., vol.74, pp.233–244 (2008).

[8] W. Yang, et al., “Numerical studies of a new-type vircator with a resonant cavity,” IEEE Trans. Plasma Sci., vol.38, pp.2428–2433 (2010).

[9] S. Champeaux, et al., “Improved design of a multistage axial vircator with reflectors for enhanced performances”, IEEE Trans. Plasma Sci., vol.44, pp.31-37 (2016).

Influence of Electrode Structure and Microwave Generation in Reflex Triode Vircator

N. Aoki, R. Haruki, and H. Ito

Graduate school of science and engineering for education , University of Toyama, Toyama 930-8555, Japan

ABSTRACT

The virtual cathode oscillator (vircator) is one of the most attractive high-power microwave sources. The most fundamental issues in the virtual cathode oscillator are conversion efficiency improvement and oscillation frequency control. We have developed the reflex triode vircator to generate high power microwave more than GW order. The reflex triode vircator was operated by Marx generator with the stored energy of 240 J. The purpose of this study is to investigate the influence of the electrode structure on the microwave generation. Experiments were conducted using three types of rogowski cathodes with different diameters for various anode-cathode gap distances.

Keywords

High-power microwave, virtual cathode oscillator, reflex triode vircator,

1. Introduction

Radiation sources of the high-power microwave are being developed for applications in plasma heating, particle acceleration, high-power radar, and many other industrial and military fields [1,2]. A Virtual Cathode Oscillator (Vircator) is a device that generates high power microwave by relativistic electron beam using pulse power technology. The vircator has the attribute of high-power capability, wide frequency tuning ability, and conceptual simplicity [3]. It is possible to generate high-power microwaves ranging from a few tens of megawatts up to a few gigawatts at frequency from a few hundreds of MHz to a few tens of GHz. However, since the vircator has a very low microwave conversion efficiency of about 10%, many researchers have been making research efforts and experimental studies to improve the microwave conversion efficiency [4-8]. In our previous studies, the evaluation of the output microwave has been performed in an axially extracted vircator with a resonance cavity to improve the microwave conversion efficiency. It has been reported that the reflex triode type has a higher conversion efficiency of the microwave than the axially extracted vircator [9-11]. We have developed the reflex triode vircator for the generation of high power microwave. In this paper, we report the experimental results on the influence of the electrode structure on the microwave generation.

2. Principle of Microwave Generation in Reflex Triode Vircator

Figure 1 shows the principle of microwave generation in the reflex triode vircator. The intense electron beam is used for the generation of microwave by the vircator. The electron beam diode consists of a cathode and an anode. When a high pulsed positive voltage is applied to the anode, electrons are emitted

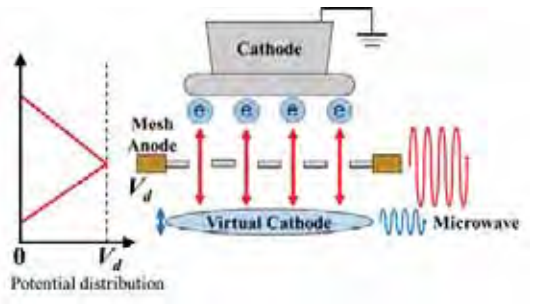

Fig.1 Schematic view for microwave generation in vircator

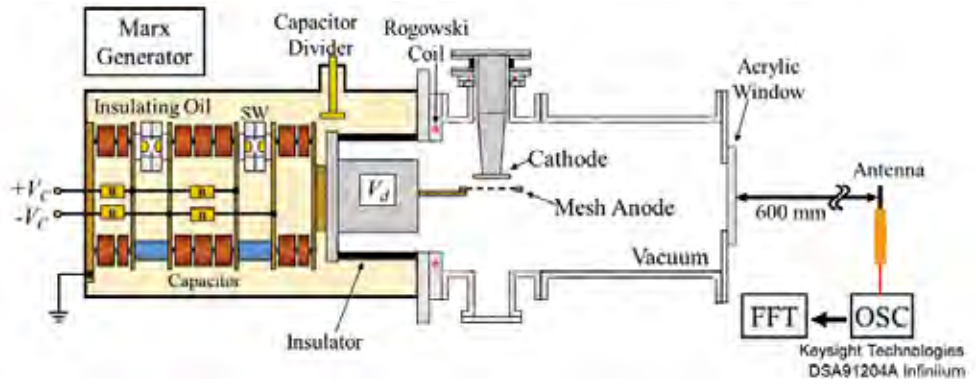

Fig.2 Schematic configuration of the reflex triode vircator

from the surface of the cathode. The electron beam passes through the anode, which is usually a thin foil or a mesh, and is injected into the drift space on the other side of the anode. When the injected electron beam current exceeds the space charge limited current in the region behind the anode, a virtual cathode, which is an unstable region of negative potential, is formed at the same distance as AK gap. Most of the electrons in the beam lose their kinetic energy and are then reflected back toward the anode. The mechanism for microwave generation in the vircator can generally be explained by two dynamical mechanisms [2, 12]. The first is electron reflection in the potential well formed between the real and virtual cathodes. The radiation frequency due to electron reflexing depends on the AK gap and the beam energy. The frequency is approximately given by

$$f_e = \frac{v_e}{4d_{AK}} \approx \frac{c\sqrt{\gamma^2 - 1}}{4d_{AK}\gamma} \tag{1}$$

where v_e is the velocity of electron, d_{AK} is the distance between the anode and the cathode, and c is the velocity of light. The relativistic factor γ is given by

$$\gamma = \frac{1}{\sqrt{1-(v_e/c)^2}} = 1 + \frac{eV_0}{m_e c^2}$$

The second is an oscillation of the virtual cathode in time and space. The oscillation frequency is given by

$$f_{vc} = \frac{5}{4\pi}\omega_p = \frac{5}{4\pi}\sqrt{\frac{e^2 n_b}{\varepsilon_0 m_e \gamma}}^{1/2}$$

$$= \frac{5}{4\pi}\sqrt{\frac{e^2}{\gamma\varepsilon_0 m_e}}\sqrt{\frac{1}{e\beta c}\left(\frac{4\varepsilon_0}{9}\left(\frac{2e}{m_e}\right)^{1/2}\frac{V_0^{3/2}}{d_{AK}^2}\right)}^{1/2} \tag{2}$$

where ω_p is the electron plasma frequency, n_b is electron beam density derived by the space charge limited current, e and m_e are the electron charge and mass, respectively, ε_0 is the vacuum permittivity, V_0 is the applied voltage across the AK gap, and β=v/c. These two oscillation frequencies are fundamentally determined by the geometric structure, the applied voltage and the electron beam parameter.

3. Experimental Setup

Figure 2 shows a schematic configuration of the reflex triode vircator used this experiment. The Marx generator with the stored energy of 240 J at a charging voltage V_c=60 kV is used as the pulsed power generator of the reflex triode vircator. The high-voltage positive pulse generated in the Marx generator is applied to a meshed anode of the electron beam diode. A vacuum explosive electron emission diode was used to generate an intense electron beam. The diode consists of a rogowski type aluminum cathode and a stainless-steel meshed anode with a transparency of ~65%. Experiments were conducted using cathodes with three types of diameters of d_c =30, 46, 60 mm for various anode-cathode gap distances. The AK gap d was in the range of 4-8 mm and changed with the step of 1 mm. The charging voltage was set to be V_c = 40, 45, and 50 kV, which correspond to the diode voltage of V_d = 160, 180, and 200 kV, respectively.

The output microwave from the vircator is emitted into a free space through an acrylic window. All microwave measurements were carried out with the receiving monopole antenna placed at a distance of 0.6

m away from the vircator window. The temporal waveform of the output microwave was recorded by a high-speed digital oscilloscope with a sampling rate of 40 GS/s through a coaxial RF cable. The oscillation frequency of the emitted microwave was evaluated by FFT analysis The diode voltage V_d was measured with a capacitive voltage divider and the diode current I_d was measured with a Rogowski coil.

4. Experimental Results

Figure 3(a) shows the typical waveforms the diode voltage V_d, the diode current I_d and the electric field of the microwave, where the anode-cathode distance is d = 4 mm, the charging voltage is V_c = 50 kV, and the cathode radius r_c = 23 mm. The diode voltage V_d has a pulse width of 50 ns and a peak voltage of 250 kV, and the diode current I_d has a peak value of 15 kA at t = 180 ns. The timing at which the microwave is emitted coincides with the time when the diode current I_d starts flowing. The timing at which the microwave is not observed is when the diode voltage V_d becomes negative, i.e., the electric field in AK gap is reversed.

Figure 3(b) shows the Fast Fourier transform (FFT) of the microwave waveform shown in Fig.3. As seen in Fig.3(b), the bandwidth of the microwave frequency is broad and the main frequency components can be identified as ~6.8 and ~9 GHz. By substituting the diode voltage V_d = 100 kV when microwave is generated into the Eqs. (1) and (2), the oscillation frequency of f_e = 10.3 GHz and f_{vc} = 8.6 GHz is obtained. Comparing these values with the FFT analysis result, we found that it is close to the frequency f_{vc} related to the virtual cathode oscillation.

We investigated the condition of the microwave generation on the anode-cathode distance d and the charging voltage V_c. Figure 4 shows the microwave electric field waveform and the FFT for various AK gap distances d, where the cathode radius and the charging voltage are set to be r_c = 15 mm and V_c = 45 kV, respectively. As seen in Fig.4, the microwave with the domain frequency of 9.5 GHz is observed at the AK gap distance of d=4 mm, while at the AK gap distance of d=6 mm, the microwave was not identified. At the AK gap distance of d=5 mm, the output microwave has various frequency components. The diode impedance increases with an increase of the AK

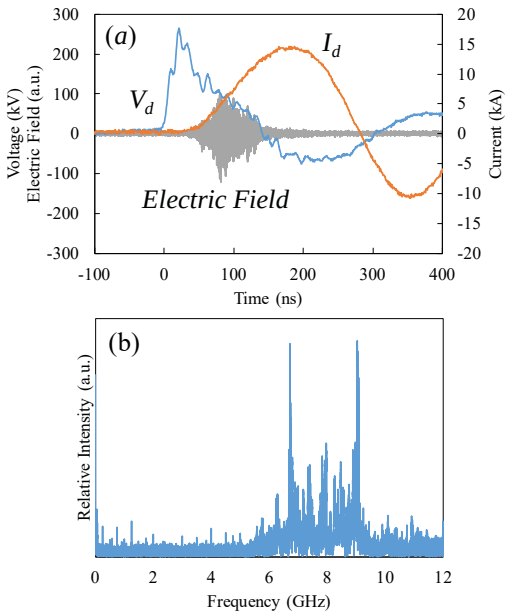

Fig. 3 (a) Typical waveforms of diode voltage V_d, diode current I_d and electric field of microwave and (b) FFT of microwave shown in Fig.3(a).

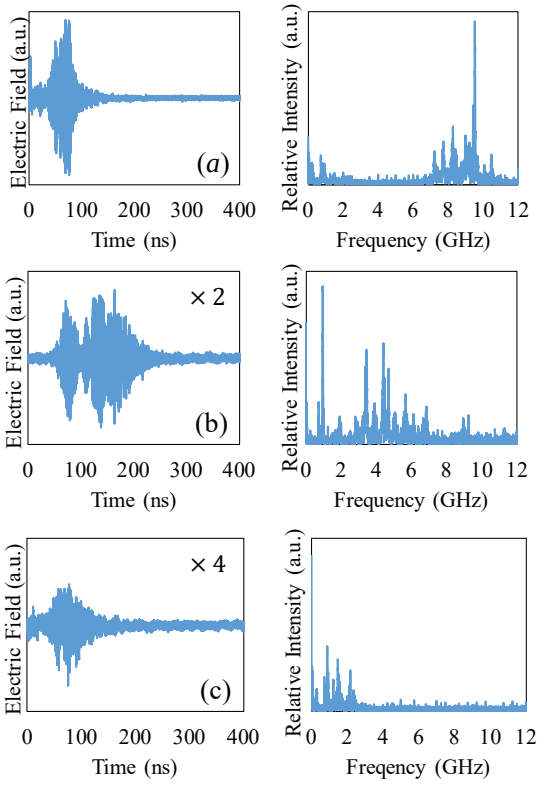

Fig. 4 Microwave electric field waveform (left figure) and FFT (right figure) for AK gap distance of (*a*) d=4 mm, (b) d=5 mm, and (c) d=6 mm

gap, resulting in the decrease of the diode current. Thus, it is considered that the formation of the virtual cathode does not work well. These results show that there is an appropriate electrode distance d for forming a virtual cathode.

Figure 5 shows the waveforms of the diode voltage V_d, the diode current I_d, the microwave electric field waveform and the FFT for the charging voltage V_c of 50 and 45 kV, where the cathode radius and the AK gap distance are r_c = 15 mm and d=6 mm, respectively. As seen from this figure, it is evident that the microwave is emitted at the charging voltage of V_c=50 kV, while at the charging voltage of V_c=45 kV, the microwave was not observed. The diode current decreases with a decrease of the diode voltage. Thus, the current is not enough to form the virtual cathode.

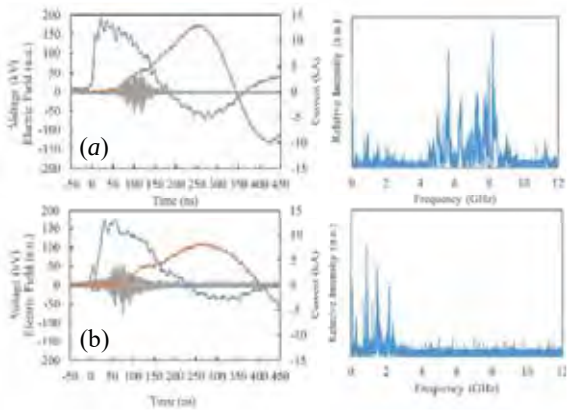

Fig. 5 Waveforms of diode voltage V_d, diode current I_d and electric field of microwave (left figure) and FFT (right figure) for charging voltage of (*a*) V_c=50 kV and (b) V_c =45 kV

The microwave generation conditions on each cathode radius r_c are summarized in Table.1 for the charging voltage V_c and the AK gap distance d for each cathode radius r_c. We found from Table 1 that the microwave tends to be stably generated with higher charging voltage or smaller AK gap distance for each cathode radius. As above mentioned, we consider that these conditions make it easier to form the virtual cathode. There is little influence of the microwave generation for the change of the cathode radius. The diode current does not increase with increasing the cathode radius, since the discharge in the AK gap does not occur uniformly but locally. However, the damage

Table 1 Microwave generation conditions for the charging voltage V_c and the AK gap distance d for each cathode radius r_c

(a) Cathode radius r_c = 15 mm	AK gap d [mm]				
Charging Voltage V_c [mm]	4	5	6	7	8
50	●	●	●	▲	▲
45	●	▲	×	×	×
40	●	▲	×	▲	×

(b) Cathode radius r_c = 23 mm	AK gap d [mm]				
Charging Voltage V_c [mm]	4	5	6	7	8
50	●	●	●	▲	▲
45	●	▲	●	▲	▲
40	●	▲	▲	▲	▲

(c) Cathode radius r_c = 30 mm	AK gap d [mm]				
Charging Voltage V_c [mm]	4	5	6	7	8
50	●	●	●	▲	▲
45	●	●	▲	▲	▲
40	●	▲	×	▲	×

of the cathode due to the discharge is reduced with larger cathode radius. Considering the repetitive operation, the optimum value seem to be found for the cathode radius. In this study, the optimum cathode radius is r_c =23 mm.

5. Conclusions

We have developed the reflex triode vircator for the generation of high power microwave. In this study, we investigated the influence of the electrode structure on the microwave generation. In the experiment, we found that the microwave tends to be stably generated with higher charging voltage and smaller AK gap distance for the cathode radius r_c. However, in consideration of the repetitive operation, the cathode radius r_c should be made larger in order to suppress the cathode damage due to the discharge.

In the future, we plan to measure the power of the microwave and find a practical way of improving its conversion of energy from the electron beam to the microwave and frequency characteristics.

References

[1] R. J. Barker and E. Schamiloglu, Eds., “High-Power Microwave Sources and Technologies”, New York: Wiley-IEEE Press (2001).

[2] J. Benford, J. Swegle, and E. Schamiloglu, “High Power Microwaves” 2nd ed., New York: Taylor & Francis (2007.

[3] D. J. Sullivan, J. E. Walsh, and E. A. Coutsias, “Virtual cathode oscillator (vircator) theory”, in High Power Microwave Sources, V. Granastein and I. Alexeff, Eds. Norwood, MA: Artech House, p. 441 (1987).

[4] B. V. Alyokhin, et al., “Theoretical and experimental studies of virtual cathode microwave devices”, IEEE Trans. Plasma Sci., vol.22, pp.945–959 (1994).

[5] E. H. Choi, et al., “High-power microwave generation from an axially extracted virtual cathode oscillator”, IEEE Trans. Plasma Sci., vol.28, pp.2128–2134 (2000).

[6] W. Jeon, et al., “Output characteristics of the high-power microwave generated from a coaxial vircator with a bar reflector in a drift region”, IEEE Trans. Plasma Sci., vol.34, pp.937-944 (2006).

[7] D. Biswas and R. Kumar, “Efficiency Enhancement of the Axial VIRCATOR”, IEEE Trans. Plasma Sci., vol.35, pp.369-378 (2007).

[8] R. Menon, et al., “High power microwave generation from coaxial virtual cathode oscillator using graphite and velvet cathodes”, J. Appl. Phys. vol.107, p.093301 (2010).

[9] W. Jiang, et al., “Experimental and simulation studies of new configuration of virtual cathode oscillator”, IEEE Trans. Plasma Sci., vol. 32, pp. 54–59 (2004).

[10] J. J. Mankowski, et al.,“ Experimental optimizationn of a reflex triode virtual cathode oscillator,” Proc. Int. Conf. High-Power Particle Beams (BEAMS), Jul. 2004, pp.426–429.

[11] V. Baryshevsky, et al., “Experimental Study of a Triode Reflex Geometry Vircator”, IEEE Trans. Plasma Sci., vol. 45, pp. 631–635 (2017).

[12] H. Sze, et al., “Dynamics of a virtual cathode oscillator driven by a pinched diode”, Phys. Fluids, vol.29, pp.3873-3880 (1986).

Characteristics of Hot Spot Radiation in the Divergent Gas-Puff Z Pinch

Keiichi Takasugi, Mineyuki Nishio*

Institute of Quantum Science, Nihon University

**Anan College, National Institute of Technology*

ABSTRACT

Characteristics of hot spots were compared among normal and reversed discharges in the divergent gas-puff z pinch. By the measurement using CCD, a small spotted hot spot was observed. The size of the hot spot was evaluated, and a smaller hot spot was observed in the reversed discharge.

Keywords

Divergent gas-puff z pinch, Hot spot size, K-shell radiation, CCD camera

1. Introduction

Gas-puff z pinch is an efficient x-ray source capable of repeated discharge [1]. Plasma focus can also cause plasma to converge to a single point reproducibly. The divergent gas-puff z pinch has been devised to realize an efficient point radiation source that combines both advantages [2].

The divergent gas-puff z pinch performs gas-puff from the center conductor to contract the plasma 3-dimensionally and generate hot spots on the front face of the conductor. Compared to conventional gas-puff z pinch, efficient energy input is possible by this method[3].

K-shell and L-shell radiations have been observed from the Ar pinch plasma[4, 5, 6]. In this study, focusing on the K-shell radiation of the divergent gas-puff z pinch, the comparison of the normal and the reversed discharges on the spatial structure of the hot spots were performed.

2. Discharge System

Experiments were conducted on the SHOTGUN III z-pinch device at Nihon University (Fig. 1). The energy storage section of the device consists of a capacitor bank of 40 kV 12 μF with maximum current of 300 kA. The feature of this device is that it can be charged either positive or negative. In this experiment the charging voltage was set at 25 kV or -25 kV.

The gas-puff was made by a high-speed gas valve installed inside the center conductor and a divergent annular Laval nozzle provided on the electrode. The divergence angle of the nozzle was 10° with respect to the central axis. The diameter of the nozzle was 30 mm, and the opposite electrode had a hole of 60 mm. The distance between the electrodes was 30 mm. Ar was used as the operating gas, and the plenum pressure of the valve was 5 atm. The electrode on the side of the center conductor was made of stainless steel and became the supply source of Fe during discharge [4].

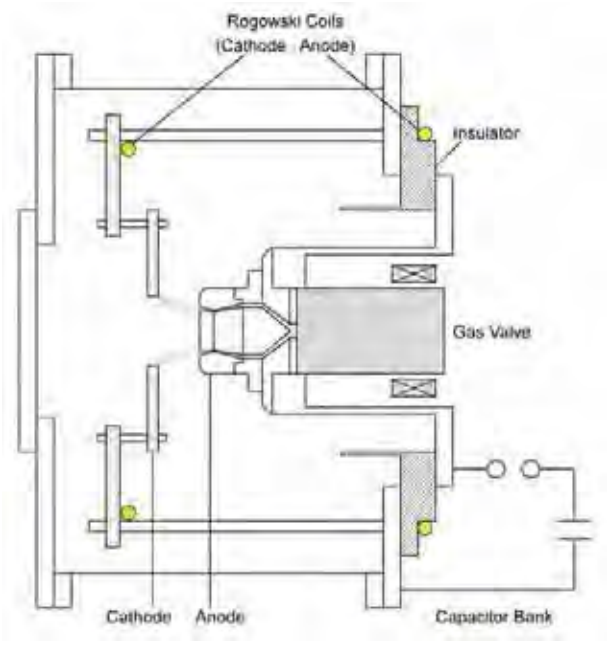

Fig. 1: Schematic diagram of the SHOTGUN III divergent gas-puff z-pinch device. The gas was puffed from the cylindrical Laval nozzle mounted on the center electrode.

3. Diagnostic System

Discharge currents were measured by Rogowski coils placed at the anode (input) and the cathode (load) sides. The anode current represents the current entering the device from the power supply, and the cathode current represents the current flowing between the electrodes.

A scintillation probe (SCI) using a 5 μm Be filter and a 3 mm thick plastic scintillator was used to monitor x-ray. The optical signal

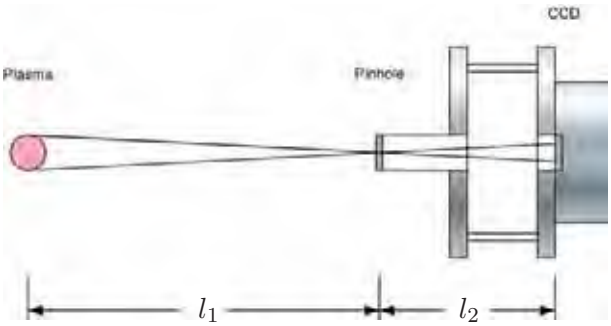

Fig. 2: Schematic diagram of the soft x-ray pinhole camera. The image was detected by the CCD.

was transmitted to the shield room by an optical fiber and converted into electric signal by a photomultiplier. X-ray exceeding 1 keV are detected, and K-shell radiation of Ar ions and Fe K_α line are observed.

Also, an x-ray diode (XRD) having a Au photocathode was used. The x-ray diodes was sensitive to wide wavelength range from ultraviolet to soft x-ray. Both K-shell and L-shell radiations of Ar ions were detected.

In order to observe the spatial structure of x-ray radiation, a pinhole camera using x-ray film was used. The pinhole diameter was 400 μm and the film was Kodak Biomax MS film.

Hot spots were observed using a pinhole camera equipped with a CCD. A CCD made by Laser-Laboratorium Göttingen e.V. was used. The sensitive range is < 1 nm $\sim$ 1,100 nm, and the pixel size is 6.45 μm, $(1,392 \times 1,040$ pixels).

Figure 2 represents the arrangement of the pinhole camera. The distance between the plasma and the pinhole was 220 mm, and the distance between the pinhole and the CCD was 155 mm. The ratio of distances was 1.4:1. A pinhole with a diameter of 20 μm and a Be filter with a thickness of 15 μm were used. Soft x-ray below 1 keV is blocked by the filter. Since the sensitivity of Fe K_α line is low, only K-shell radiation of Ar ions can be observed.

Since the pinhole diameter is not sufficiently small, the size of the hot spot is not simply 1.4 times the size of the image. The image diameter D is expressed as

$$D = a\frac{l_1 + l_2}{l_1} + d\frac{l_2}{l_1}, \qquad (1)$$

where a is the pinhole diameter, d is the hot spot diameter, l_1 is the distance between the hot spot and pinhole and l_2 is the distance between the pinhole and the image. The first term becomes important when a is not sufficiently small compared to d.

4. Experimental Results

Figure 3 shows the current waveform and x-ray signals for (a) normal discharge with charging voltage of 25 kV and (b) reversed discharge with charging voltage of -25 kV. The peak current was about 180 kA for normal discharge and

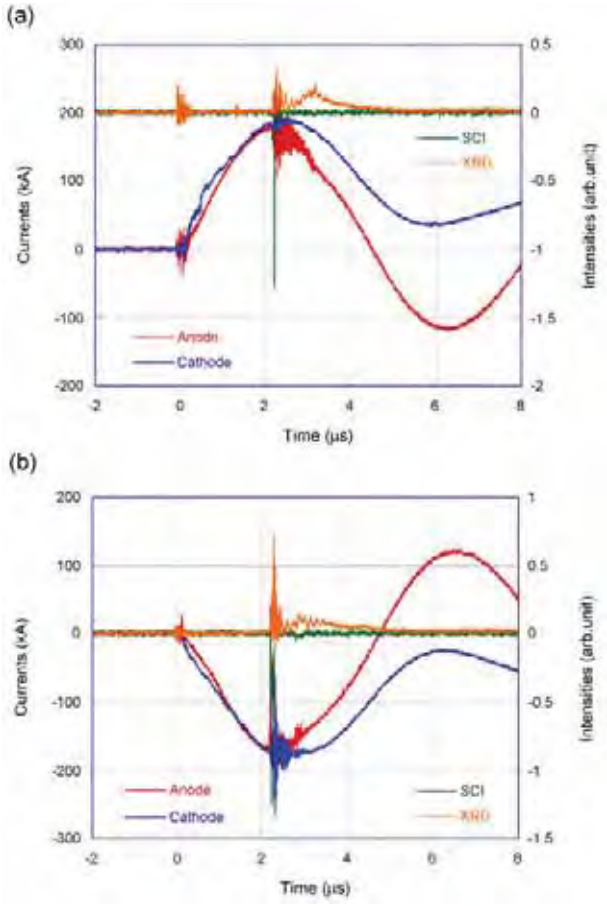

Fig. 3: Discharge currents and x-ray signals of divergent gas-puff z pinch in (a) normal and (b) reversed discharges.

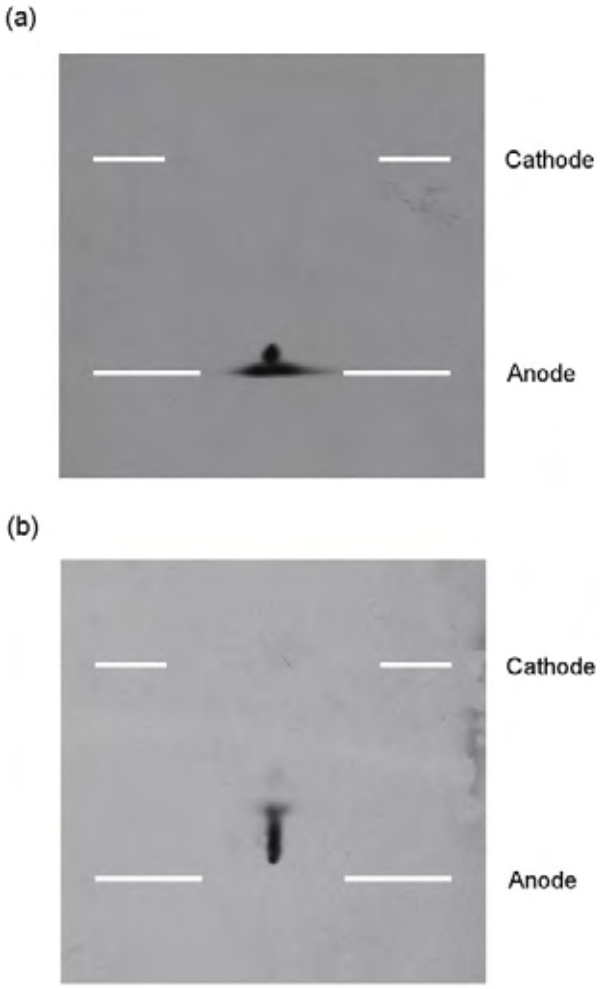

Fig. 4: X-ray pinhole images of divergent gas-puff z-pinch taken by x-ray film in (a) normal and (b) reversed discharges.

about -170 kA for reversed discharge. In each cases, a strong shrinkage occurred in the vicinity of the peak current after 2.25 μs from the discharge start, and a dent was formed in the current. A spike-like SCI signal was observed with the shrinkage. The XRD signal was observed at the contraction and subsequently.

Figure 4 is the image of a hot spot recorded with x-ray film for (a) normal discharge and (b) reversed discharge. In normal discharge, a hot spot was generated on the anode front surface, and x-ray was also generated from the anode surface. In the reversed discharge, no x-ray was observed on the electrode surface. Instead, the hot spot was made to grow long in the axial direction.

Figure 5 is the image of the hot spot projected onto the CCD for (a) normal discharge and (b) reversed discharge. The horizontal direction means the axial direction and the vertical direction means the radial direction. The hot spots were observed as small dot shapes, which were quite different from those in Fig. 4. In normal discharge, the horizontal length was 80 μm and the vertical width was 90 μm. In the reversed discharge, the horizontal length was 50 μm and the vertical width was 60 μm. The resolution is pixel size of 6.45 μm. Relatively small hot spot was observed in the reversed discharge.

5. Summary and Discussion

Normal and reversed discharges of the divergent gas-puff z pinch were performed. In both cases, a strong shrinkage occurred at 2.25 μs after the discharge started, and generation of

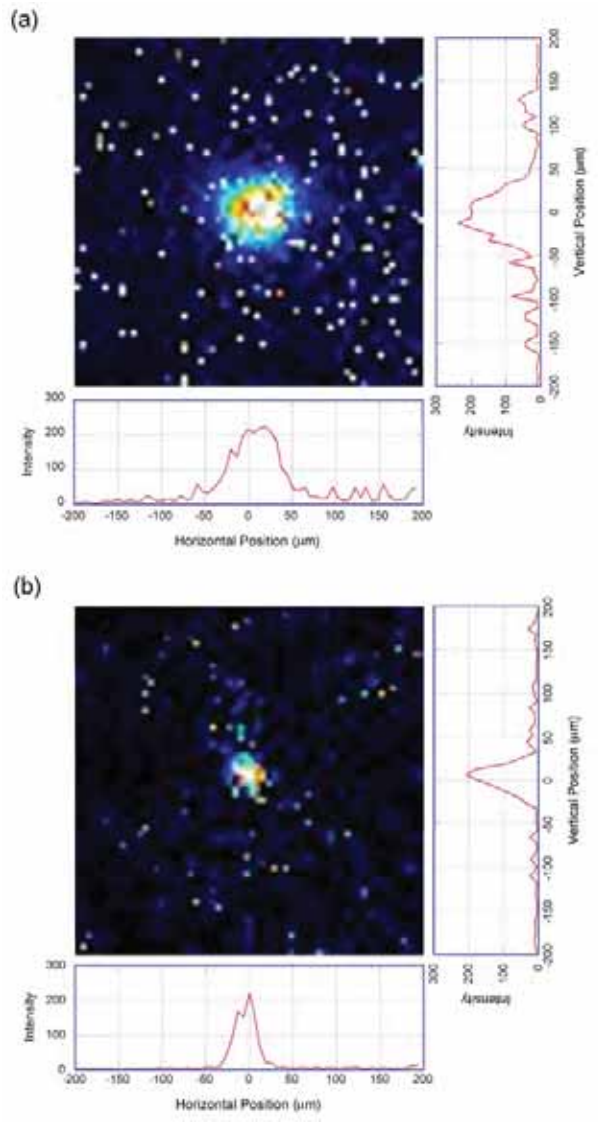

Fig. 5: Soft x-ray images of hot spots on the CCD taken in (a) normal and (b) reversed discharges.

soft x-ray was confirmed. Soft x-ray emitted from hot spots were measured.

K-shell radiation image of hot spot was observed by the CCD camera. Since the diameter of the pinhole used for the measurement was not sufficiently small compared to the hot spot, the hot spot size was analyzed in consideration with the pinhole size. The measurement resolution was 14 μm. In this measurement, a hot spot smaller in reverse discharge than in normal discharge was observed. Since there are not many measurement examples yet, it is not always clear whether there is such a tendency.

In this reversed discharge, considering that

	+25 kV	-25 kV
Horizontal length (μm)	65	23
Vertical width (μm)	79	37

Table 1: Horizontal and vertical size of a hotspot in normal and reversed discharges.

a current of 170 kA is flowing inside the circle of diameter 23 μm, the magnetic flux density at the outer circumference is 3.0×10^3 T, the magnetic pressure is 3.5×10^{12} Pa. Assuming the pressure balance, when the temperature is 1 keV, the combined ion and electron density is 2.2×10^{28} m^{-3}. This value is overvalued by three orders of magnitude compared to the spectroscopic measurement result [7]. If we trust the spectroscopic result, the current is flowing a little wider area.

The shape of the hot spot image of the CCD is different from that of the x-ray film. The difference between CCD and x-ray film is whether you feel Fe K_α line. A nearly spherical hot spot was observed in the CCD. It is thought that Fe atoms or ions get into other parts and emit x-ray. In the case of normal discharge, it is considered that the anode surface emits x-ray and the electron beam directly strikes the anode. In the case of reverse discharge, x-ray are emitted with a strange elongated shape. Within a short period of time from the start of discharge, probably Fe ions enter the plasma and are thought to be illuminated by the electron beam generated together with the pinch.

References

[1] J. Shiloh, A. Fisher and N. Rostoker: Phys. Rev. Lett. **40**, 515 (1978).

[2] K. Takasugi and E. Kiuchi: Plasma Fusion Res. **2**, 036 (2007).

[3] K. Takasugi and E. Kiuchi: NIFS-PROC **72**, 17 (2008).

[4] E.O. Baronova, K. Takasugi, V.V. Vikhrev and T. Miyamoto: Proc. 13th Int. Conf. Particle Beams, 784 (2001).

[5] K. Takasugi and H. Akiyama: Jpn. J. Appl. Phys **43**, 6376 (2004).

[6] F. Kobayashi and K. Takasugi: NIFS-PROC **62**, 10 (2006).

[7] V.V. Shlyaptseva et.al.: submitted to IEEE Trans. Plasma Science.

Numerical Modeling of Electron Beam Diode as Impedance Controller for Warm Dense Matter Generation Using Intense Pulsed Power Device

Md. Shahed-Uz-Zaman, Kazumasa Takahashi, Toru Sasaki, Takashi Kikuchi

Nagaoka University of Technology, Niigata 940-2188, Japan

ABSTRACT

Numerical modeling of electron beam diode as impedance controller to control an input energy in a sample load to generate warm dense matter using an intense pulsed power device ETIGO-II was studied. Electron beam radius in a beam diode gap was expanded due to the space charge effect. Both theoretical and numerical analyses in the electron beam radial expansion were investigated because of its considerable effect on the beam diode impedance.

Keywords

Electron beam diode, Impedance controller, Beam radial expansion, Pulsed-power generator

1. Introduction

Nuclear energy release by inertial confinement fusion (ICF) is one of the most promising next-generation energy sources to solve the energy problem. In the ICF system, materials of a fuel pellet pass through warm dense matter (WDM) regime during the implosion process [1, 2]. In the implosion process of ICF, a temperature-density region with unclear physical properties known as WDM is so important, and has a considerable effect on implosion dynamics [3, 4]. For this reason, research of WDM property at comparable pulse duration of ICF implosion timescale using an intense pulsed power generator "ETIGO-II" with an electron beam diode was proposed [5-7]. The electron beam diode behaves as an impedance controller, which regulates the input energy into the sample load to generate WDM using an isochoric heating technique [8]. Simplified physical properties and behavior of the electron beam diode impedance in the diode gap is needed to understand the WDM properties.

The input energy control and the beam output current of the electron beam diode at the beam diode gap was investigated experimentally [6-8]. The numerical analysis of electron behavior in the beam diode with an electrostatic particle-in-cell (PIC) model corresponding to the experimental results and experimental conditions of the intense pulsed power generator ETIGO-II was also carried out [9]. However, the beam diode impedance behavior was not clearly understood. For the clear understanding of beam diode behavior is necessary to study the equation-of-state for WDM and the constructive structure of WDM generation experimental setup. A numerical model of electron beam diode as the impedance controller with numerically obtained beam radius was analyzed. Tentative beam diode impedance range with the beam radius expansion in beam diode gap was estimated to understand the experimental setup of WDM generation and properties in the implosion time scale of ICF.

2. Numerical model

Figure 1 shows the schematic diagram of computational box and numerical condition for the modeling of electron map in beam diode gap using 2D electrostatic PIC model corresponding to the experimental condition, which was considered as

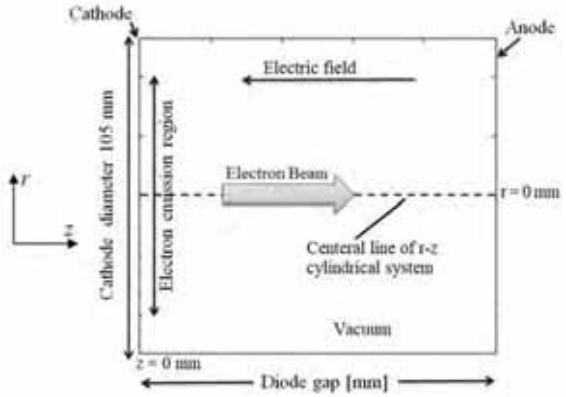

Fig. 1 Computational box and schematic diagram of electron map for numerical simulation in beam diode gap, where electrons emitted from cathode surface due to the electric field from applied voltage, and travel through vacuum. Space charge limited condition is applied for electron beam emission from cathode surface and beam diode gap is set as 10 mm, 15 mm and 20 mm alone with the different initial beam radius of 40 mm, 30 mm and 20 mm.

axisymmetric configuration. Due to the electric field from the applied voltage, electrons emitted from the cathode propagate in a vacuum towards anode. In Fig.1, the left and right boundaries were given as the cathode and the anode. The simulation parameters were assumed by the experimental setup.

The electron emission at the cathode surface was applied to satisfy the space charge limiting emission condition. The electric field components are E_r and E_z, and v_r and v_z are particle velocities in r and z

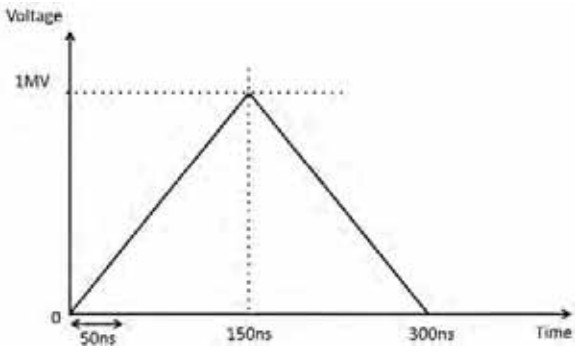

Fig. 2 Applied voltage waveform: maximum voltage is 1 MV, pulse width is 300 ns, the rise and fall time is 150 ns each.

directions, which were solved by Maxwell equation in discretized calculation cells and relativistic equation of motion.

In this calculation condition, the input pulse voltage was 1 MV maximum, which was the normal value of intense pulsed power generator ETIGO-II [10]. The pulse width was 300 ns with rise and fall times of 150 ns each as shown in Fig.2. The peak voltage was 1 MV at 150 ns. The resistance of 1.7 Ω, and the output beam current was 50 ns lack by the applied voltage [7, 10].

The initial beam radius was assumed by 20 mm, 30 mm, and 40 mm. The diode gap distance was assumed by 10 mm, 15 mm, and 20 mm according to the experimental condition [7].

3. Results and Discussion

Figures 3, 4 and 5 show the electron map of electron beam in the diode gap for 10 mm (Fig. 3 (a), (b) and (c)), 15 mm (Fig. 4 (a), (b) and (c)) and 20 mm (Fig. 5 (a), (b) and (c)) with various initial electron beam radius conditions at t = 150 ns. After the electron emission from the cathode surface, the electrons were accelerated towards the anode side due to the electric field from the applied voltage, and the electron beam radius expanded radially due to the repulsive self space charge field created by the electrons. Figures 3, 4 and 5 indicate that in case of small diode gap distance (Figs. 3 and 4) the beam radial expansion was small due to the short beam diode gap and short travelling time to expand. However, with the increase of beam diode gap (Fig. 5) the beam radial expansion increases due to the long diode gap and sufficient travelling to expand more in radial direction. In comparison between the short diode gap and the long diode gap, the final beam expansion radius becomes double with the increase of diode gap from 10 mm to 20 mm (see Figs. 3 and 5). On the other hand, with the increase of initial beam radius, the beam expansion also increases (see Fig. 3 (a), (b) and (c); Fig. 4 (a), (b) and (c), and Fig. 5 (a), (b) and (c)). Numerically obtained beam radial expansion data was compared with the theoretically obtained beam envelope line to

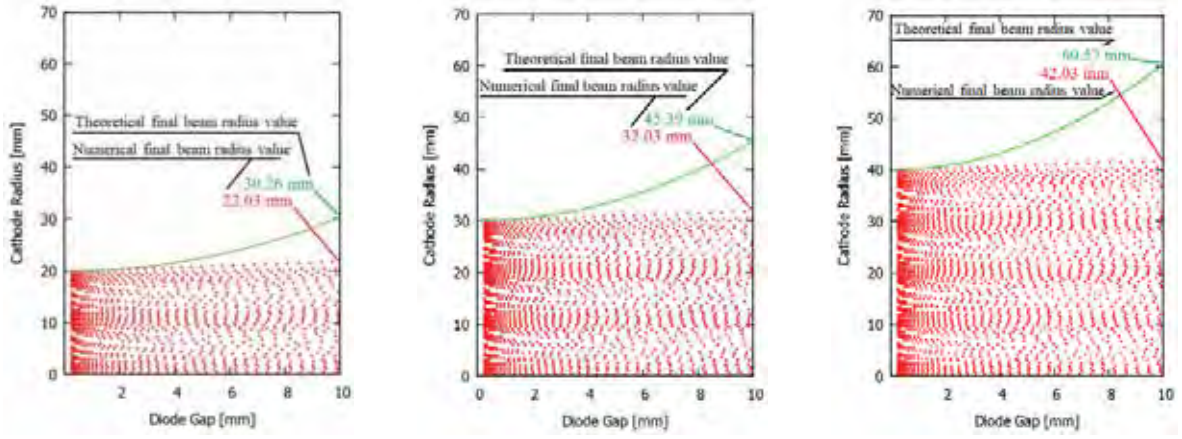

(a) (b) (c)

Fig. 3 Numerically obtained electron maps for 10 mm beam diode gap at t = 150 ns. Beam radial expansion was compared both theoretically and numerically: (a) initial beam radius is 20 mm, (b) initial beam radius is 30 mm, and (c) initial beam radius is 40 mm.

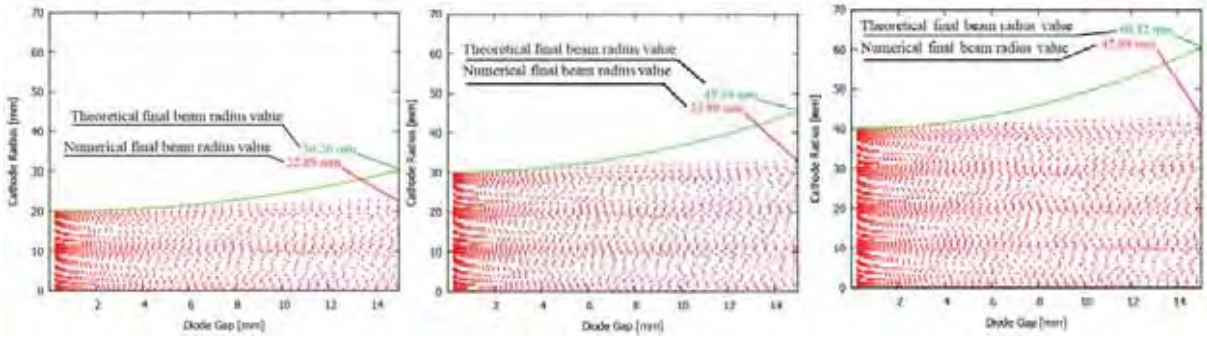

(a) (b) (c)

Fig. 4 Numerically obtained electron maps for 15 mm beam diode gap at t = 150 ns. Beam radial expansion was compared both theoretically and numerically: (a) initial beam radius is 20 mm, (b) initial beam radius is 30 mm, and (c) initial beam radius is 40 mm.

observe the beam expansion behavior in the beam diode gap. The theoretical beam envelope was obtained from a simplified envelope equation [12, 13],

$$r_e = r_b + \frac{I_{0\max} e z^2}{4\pi\varepsilon_0 v_{z0}^3 r_b m} \quad \cdots\cdots (1)$$

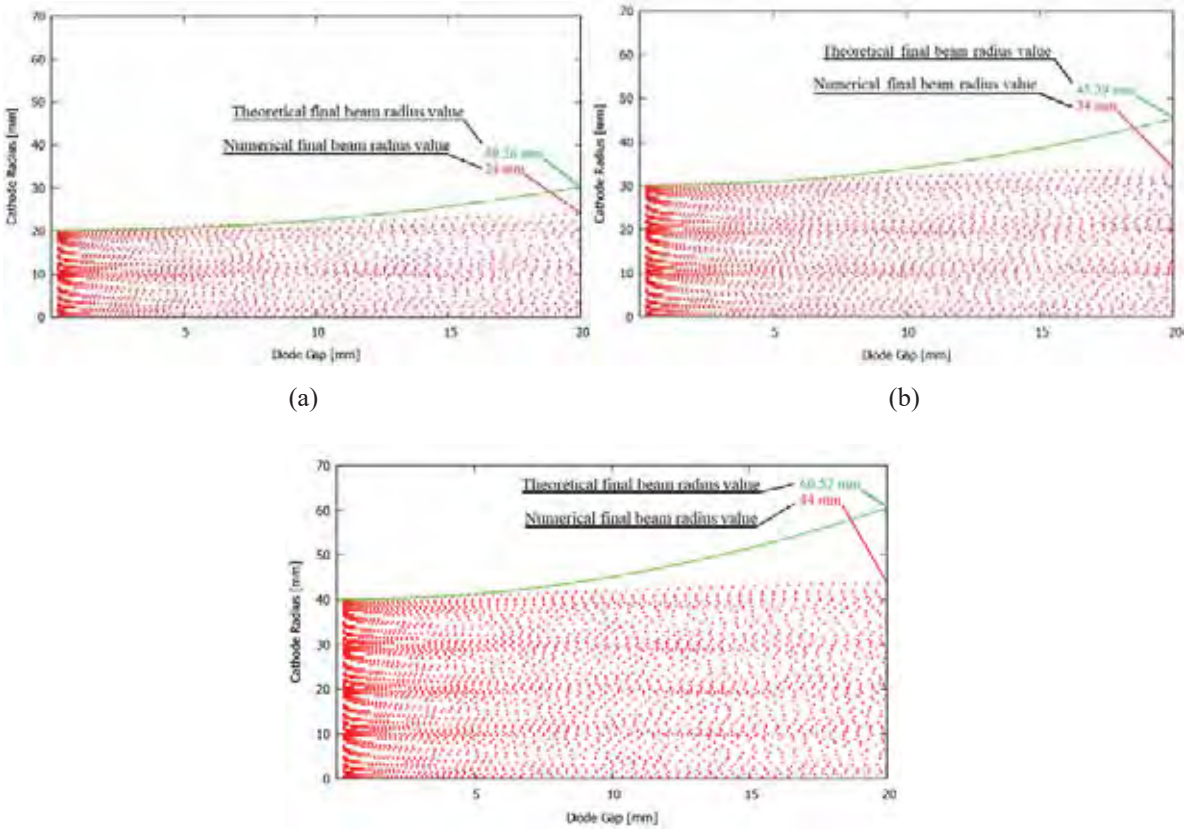

Fig. 5 Numerically obtained electron maps for 20 mm beam diode gap at t = 150 ns. Beam radial expansion was compared both theoretically and numerically: (a) initial beam radius is 20 mm, (b) initial beam radius is 30 mm, and (c) initial beam radius is 40 mm.

Here e is the electron charge, r_b is the initial beam radius, r_e is the beam envelope radius, v_{zo} is the electron velocity, m is the electron mass, ε_0 is the permittivity in vacuum, and $I_{0\max}$ is the maximum beam current, which was measured for 10 mm, 15 mm and 20 mm diode gap at 40 mm, 30 mm, and 20 mm for electron emission radius condition using the space-charge limited equation [9]. The electron beam radius in the radial direction tends to expand gradually as the theoretically obtained beam envelope line. Moreover, in the numerical simulation results, the variable initial electron beam radius with the function of time dependent variable voltage was not considered, and the initial beam radius was framed as constant, where the initial electron beam radius in experiment varies with time in the applied voltage.

Figure 6 shows the ratio of initial beam radius and numerically obtained final beam radius with the function of diode gap for different initial beam radius condition of 40 mm, 30 mm and 20 mm. The ratio of initial beam radius and numerically obtained final beam radius shows that in case of small diode gap,

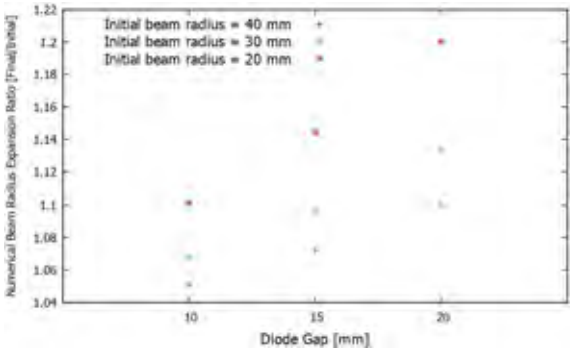

Fig. 6 Ratio of initial beam radius and numerically obtained final beam radius for d = 10 mm, 15 mm and 29 mm at initial beam radius of 20 mm, 30 mm and 40 mm.

the initial beam radius was nearly equal to the final beam radius. In the increase of diode gap length, the beam radius expands more, and the final beam radius is larger than the initial beam radius (see in Fig.6).

Figure 7 shows the theoretically obtained beam diode impedance with the function of electron beam radius for different beam diode gap. The theoretical beam diode impedance was calculated by Eq.(2), which was derived from Child-Langmuir law [11].

$$Z_b = \frac{9d^2}{4\varepsilon_0 \pi r_{eb}{}^2 V^{\frac{1}{2}}} \sqrt{\frac{m}{2e}} \quad \cdots\cdots (2)$$

Here, Z_b is beam diode impedance, r_{eb} is the electron beam radius, and V is the applied voltage (1 MV). Figure 7 illustrates the beam diode impedance behavior for 10 mm, 15 mm and 20 mm in the beam diode gap at the initial beam radius condition of 30 mm. The final beam radius was calculated numerically (see Figs. 3, 4, and 5). Here, the initial beam radius of 30 mm was considered for the analysis of beam diode impedance behavior, which is the tentative beam radius from the comparison of theoretical, numerical and experimental results [9]. Figure 7 indicates that in the case of short beam diode gap and the small initial beam radius, the beam diode impedance near the cathode was nearly equal to the beam diode impedance near the anode due to the small beam expansion. On the other hand, with the

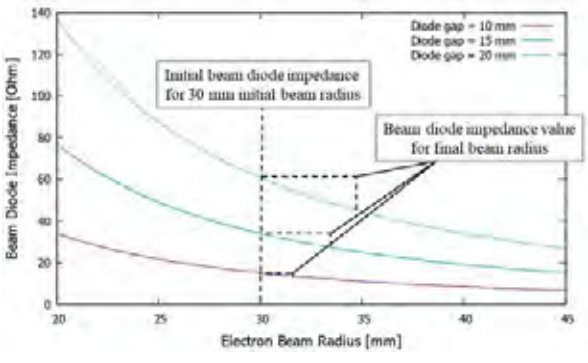

Fig. 7 Theoretically obtained beam diode impedance as a function of electron beam radius for 10 mm, 15 mm and 20 mm diode gap and an impedance range of 30 mm initial beam radius state, where final beam radius was obtained numerically

increase of beam diode gap, the beam radius expands in the radial direction. The difference between the initial beam radius and the final beam radius increases, and the discrepancy between the beam diode impedance near the cathode and the anode also increases. The beam diode impedance range is 15.16 Ω ~ 13.32 Ω for d = 10 mm, 34.10 Ω ~ 28.15 Ω for d = 15 mm, and 60.63 Ω ~ 47.20 Ω for d = 20 mm at the initial beam radius condition of 30 mm.

4. Conclusions

In this study, the numerical analysis of the electron behavior in the beam diode with the electrostatic PIC model corresponding to the experimental conditions of the intense pulsed power generator “ETIGO-II” was carried out for the beam diode impedance behavior. The numerical model of the electron beam diode as the impedance controller with numerically obtained beam radius was analyzed. The beam diode impedance range with the beam radius expansion in beam diode gap was estimated to understand the experimental setup of WDM generation and properties in the implosion time scale of ICF. The numerically obtained beam radius expansion data, we were able to estimate the electron beam diode impedance range, and observed the impedance behavior of the beam diode for the different beam diode gap. It will be useful for the further study for the experimental setup of WDM generation at the implosion timescale of ICF.

References

[1] S. ATZENI and J. MEYER-TER-VEHN “The Physics of Inertial Fusion: Beam Plasma Interaction, Hydrodynamics, Hot Dense Matter”, *Oxford University Press*, (2004)

[2] S. PFALZNER “An Introduction to Inertial Confinement Fusion”, *CRC Press*, (2006)

[3] Y. KOMATSU et al., "Changes of Implosion Dynamics Derived by Difference of Equation of State", *EPJ Web of Conference,* **59**, 04010, (2013)

[4] R. P. DRAKE “High-Energy-Density Physics:

Fundamentals, Inertial Fusion, and Experimental Astrophysics", *Springer Science & Business Media*, (2006).

[5] Y. AMANO et al., "Isochoric Heating of Foamed Metal Using Pulsed Power Discharge as a Making Technique of Warm Dense Matter", *Review of Scientific Instruments,* **83.8,** 085107 (2012).

[6] R. HAYASHI et al., "Numerical Analysis of Temperature Distribution for Isochoric Heating with Intense Pulsed Power Discharge Using Electron Beam Diode Based Impedance Controller", *IEEE 41st International Conference on Plasma Sciences (ICOPS) held with* 2014 *IEEE International Conference on High-Power Particle Beams (BEAMS)*, (2014)

[7] R. HAYASHI et al., "Impedance Control Using Electron Beam Diode in Intense Pulsed-Power Generator", *Laser and Particle Beams*, **33.02,** pp. 163-167 (2015)

[8] T. ITO et al., "Input Energy Control Using Electron Beam Diode as Impedance Controller to Study Warm Dense Matter by Pulsed Power Discharge with Isochoric Heating", *Plasma and Fusion Research*, **12**, 1204024 (2017).

[9] MD. SHAHED-UZ–ZAMAN et al., "Electron Behavior in Beam Diode Driven by Intense Pulsed Power Device for Dense Matter State Research of Inertial Confinement Fusion", *Energy Procedia*, 131C, pp. 348-353 (2017)

[10] W. JIANG et al., "Tight Focusing of Intense Pulsed Light-Ion Beam by Spherical "Plasma Focus Diode"", *Japanese journal of applied physics*, 32, 5B, L752 (1993)

[11] C. D. CHILD "Discharge from Hot CaO", *Physical Review (Series I)*, **32**, 5, p. 492 (1911)

[12] T. KIKUCHI et al., "Intense-Heavy-Ion-Beam Transport through an Insulator Beam Guide", *Japanese Journal of Applied Physics*, **38**, 3A, p. L270 (1999)

[13] R. MILLER "An Introduction to the Physics of Intense Charged Particle Beams", *Springer Science & Business Media*, (2012)

[14] S. I. Toyama "Analysis of beam envelope by transverse space charge effect" *(No. PNC-TN--9410-97-056), Power Reactor and Nuclear Fuel Development Corp* (1997)

[15] S. Humphries "Charged particle beams" *Dover Publications*, (2013)

Thermal Conductivity Measurement of Dense Tungsten Plasma Using Laser-Induced Fluorescence

Shingo Kusano, Satoshi Sugimoto, Kazumasa Takahashi, Toru Sasaki, Takashi Kikuchi

Nagaoka University of Technology

ABSTRACT

We have measured the thermal conductivity of dense plasma using an isochorically-heating pulsed-power discharge with a laser-induced fluorescence. To understands the thermal conductivity dependences on temperature and density for the dense tungsten plasma, we have measured the thermal conductivity of several tungsten samples. The results show that the thermal conductivity is increased with the increase of temperature. The obtained thermal conductivity at the plasma temperature of 10000K is approximately $\log_{10} \kappa = 1.5$ W/(m·K), regardless of density.

Keywords

Thermonuclear fusion, Warm dense matter, Pulsed-power discharges, Laser-induced fluorescence

1. Introduction

Thermonuclear fusion systems have a divertor for the plasma facing components. The divertor is the exhaust device of fusion product as an α-particle escaping from fusion plasma. Tungsten has been selected a material of divertor surface for the international thermonuclear fusion reactor (ITER) because it has a high melting point [1,2]. The surface of divertor is damaged by bombardment of high energetic particle flux from fusion plasma, at the plasma disruption, the edge localized modes and vertical displacements [3,4]. The divertor material will evaporate these off-normal events [1]. The ablated material of the divertor surface will be changed to a state of warm dense matter (WDM) during energetic particles irradiation. However, WDM is the complex state because of the phase transition from a solid to a plasma state, degenerated electrons, and so on. The WDM regime is dense and low-temperature plasma compared to the conventional plasmas state. The experimental data of WDM is required to understand the properties as the transport properties, the equation of state, and so on [5,6].

In the previous studies, to measure the various properties of WDM state had been developed because of energy drivers such as pulsed power discharges, ultra-short-pulse laser, and intense heavy ion beams [7-13]. The generating method of WDM using the pulsed-power discharge is possible to measure a long time scale compared to the other energy driver. We have developed a pulsed-power discharge with isochoric heating system confined by a quasi-rigid capillary tube [14]. This method has possible to generate dense plasma with well-defined density. Moreover, we have developed a method of directly determine the thermal conductivity of the WDM state with a laser-induced fluorescence from ruby [15].

In this paper we clarified the thermal conductivity dependence on temperature and density for WDM using a laser-induced fluorescence method.

2. Experimental Setup

Figure 1 shows the experimental setup of the measurement of thermal conductivity for the WDM. The WDM was generated by pulsed-power discharge with isochoric heating using cylindrical ruby capillary. The pulsed-power discharge was driven by low inductance capacitors of capacitance C = 3.78 μF (1.89μF×2) with 14 kV in charged voltage. We used the sample of thin tungsten wire with D_W = 50-300 μm

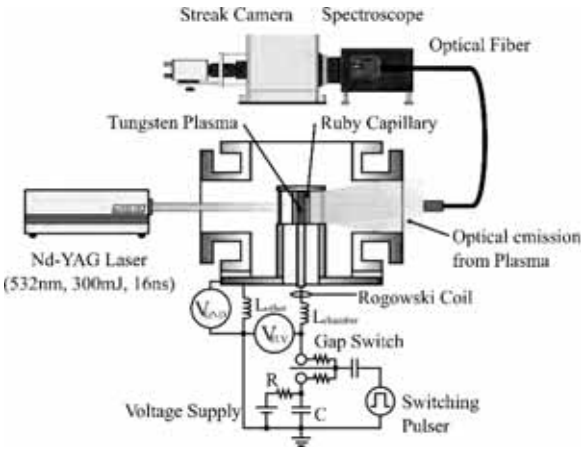

Fig. 1 Experimental setup for laser-induced fluorescence with isochoric pulsed-power discharge

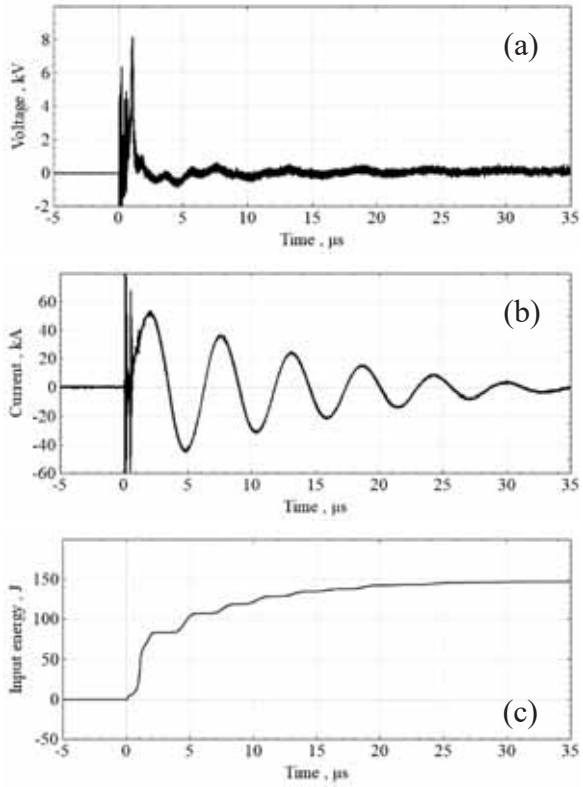

Fig. 2 Typical discharge waveform by isochoric heating device using a pulsed-power discharge.

of a diameter and 15 mm in length. The ruby capillary was 1 mm of inner diameter and 4mm of outer diameter. The mass density of tungsten plasma was set to be $0.0025\rho_s$ - $0.09\ \rho_s$ (ρ_s: solid density). We used a high-voltage probe and Rogowski coil to measure the time-evolution of voltage and current in the wire and plasma, respectively.

The thermal conductivity of warm dense tungsten plasma is estimated by to measure time-evolution of the heat flux from the tungsten plasma to the ruby capillary. Furthermore, the plasma temperature is assumed uniform and cylindrical symmetry, the temperature gradient occurs with the radial direction. To measure the thermal conductivity of the warm dense tungsten plasma, which is given by,

$$\kappa_{\mathrm{P}} = \frac{\rho_{\mathrm{R}} C_{\mathrm{vR}} \frac{\partial T_{\mathrm{R}}}{\partial t} \Delta r^2 + \kappa_{\mathrm{R}} \left(\frac{T_{\mathrm{P}} + T_{\mathrm{R}}}{2} - T_{\mathrm{R}} \right)}{T_{\mathrm{P}} - \frac{T_{\mathrm{P}} + T_{\mathrm{R}}}{2}}. \quad (1)$$

Here, ρ is the density, C_{v} is the specific heat, T is the temperature, and κ is the thermal conductivity, respectively. Moreover, the suffix of P refers to the plasma component, the suffix of R is the ruby component. The typical diffusion length, Δr is estimated by the conventional thermal diffusion for radial direction,

$$\Delta r = \sqrt{2 \frac{\kappa_{\mathrm{P}}}{\rho_{\mathrm{R}} C_{\mathrm{VR}}} \Delta t}\ . \quad (2)$$

On the Eq. (2), Δt is the thermal diffusion time in the ruby capillary from the beginning of attaching plasma to the interior of ruby capillary. From Eq. (1), the thermal conductivity of WDM is estimated from the temperature of both the ruby capillary and tungsten plasma. Therefore, we are required to measure each temperature. The ruby temperature is obtained by fluorescence intensity from the ruby capillary. The intensity of ruby fluorescence depends on temperature which is decreasing with the temperature increasing [16,17]. The fluorescence from the ruby capillary was induced by the Nd-YAG laser (532 nm, 300 mJ, 16 ns). The plasma temperature was estimated from the optical emission of plasma by assuming local thermodynamic equilibrium [18]. Each temperature is obtained from the time-resolved spectroscopy which was used the spectrometer mounted on a streak camera. Typical voltage-current waveforms and the input energy history of the tungsten plasma are shown in Figs. 2. The peak voltage and current of this condition are about 5kV and 50 kA, respectively. The input energy to the tungsten plasma was estimated to be

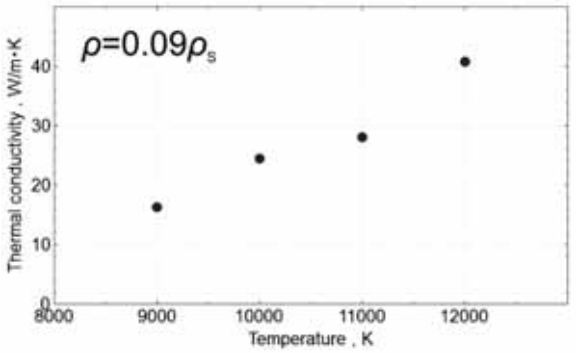

Fig. 3 Thermal conductivity as a function of the temperature of tungsten plasma at $\rho = 0.09\rho_S$

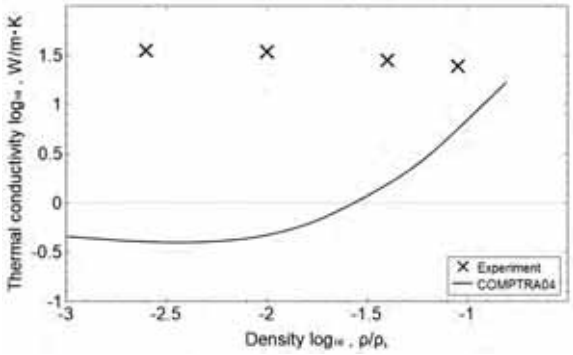

Fig. 4 Thermal conductivity of tungsten plasma as a function of density at 10000K, the solid line indicated the thermal conductivity given by COMPTRA 04 [19,20], the cross point shows the result obtained in the present work.

approximately 150 J in generating the WDM.

3. Results and Discussion

Figure 3 shows the thermal conductivity of tungsten plasma at the density of $0.09\rho_S$ as a function of temperature. We can see that the thermal conductivity is increased with the temperature rising. The thermal conductivities at the different density were the similar tendency as shown in Fig. 3. The thermal conductivity of dense tungsten plasma is increased with the temperature rising.

Figure 4 shows the thermal conductivity of tungsten plasma at the plasma temperature of 10000K as a function of density. The cross point and the line in Fig. 4 are indicated the thermal conductivity obtained from the experiment and the theoretical calculation thermal conductivity at the plasma temperature of 10000 K [19,20], respectively. The thermal conductivities from the experiment are approximately $\log_{10} \kappa$ = 1.5 W/(m·K), regardless of the plasma density. Whereas, the thermal conductivity estimated by theoretical calculation is increased with increasing the density of tungsten plasma. The thermal conductivity obtained by this experiment is over 10 times higher than that from the theoretical prediction by COMPTRA 04. Therefore, we will explore the discrepancy of thermal conductivity from the experimental observations.

4. Conclusions

We have experimentally measurement the temperature-density dependence on the thermal conductivity in dense tungsten plasma generated by pulsed-power discharge. The thermal conductivity was obtained by utilized the laser-induced fluorescence method with a time-resolved spectrometer. The thermal conductivities from the experiment are increased with the plasma temperature rising. Moreover, the thermal conductivities are approximately $\log_{10} \kappa$ = 1.5 W /(m·K), regardless of the plasma density. The thermal conductivity from the experimental observation is over 10 times higher than that from the theoretical prediction from COMPTRA04.

References

[1] ITER Summary of the ITER Final Design Report (ITER ODA DOCUMENTATION SERIES No.22) (2012).

[2] Mario Merola, Frederic Escourbiac, Alphonse Rene Raffray, Philippe Chappuis, Takeshi Hirai, Stefan Gicquel: Fusion Eng. Des. **96-97** (2015) 34-41.

[3] G. T. A. Huijsmans, C. S. Chang, N. Ferrarro, L. Sugiyama, F. Waelbroeck, X. Q. Xu, A. Loarte, and S. Futatani: Phys. Plasma **22** (2005) 021805.

[4] M. Sugihara, Y. Kamada: J. Plasma Fusion Res. **82** (2006) 566-574.

[5] J. Hasegawa, K. Takayama, T. Sasaki and K. Horioka: J. Plasma Fusion Res. **86** (2010) 269-281.

[6] H. Yoneda: J. Plasma Fusion Res. (2005) 172-180.

[7] A. W. DeSilva and H. J. Kunze: Phys. Rev. E **49** (1994) 4448.
[8] A. W. DeSilva and J. D. Katsouros: Phys. Rev. E **57** (1998) 5945.
[9] T. Sasaki, Y. Yano, M. Nakajima, T. Kawamura, and K. Horioka: Laser Part. Beam **24** (2006) 371.
[10] T. Sasaki, M. Nakajima, T. Kawamura, and K. Horioka: Phys. Plasmas **17** (2010) 084501.
[11] H. Yoneda: J. Plasma Fusion Res. (2007) 624-627.
[12] F. B. Romeji, R. W. Lee, D. Riley, J. Meyer-ter-Vehn, A. Krenz, T. Tschentscher, An. Tauschwitz, A. Taushwitz, V. S. Lisitsa A. Ya. Faenov: J. Phys.: Conf. Ser. **72** (2007) 012007.
[13] F. M. Bieniosek, J.J. Barnard, A. Friedman, E. Henetroza, J. Y. Jung, M. A. Leitner, S. Lidia, B.G. Logan, R. M. More, P. A. Ni, P. K. Roy, P. A. Seidl, W. L. Waldron: J. Phys.: Conf. Ser. **244** (2010) 032028.
[14] Y. Amano, Y. Miki, T. Takahashi, T. Sasaki, T. Kikuchi and N. Harada: Rev. Sci. Instrum. **83** (2006) 085107.
[15] S. Sugimoto, A. Watabe, Y. Sugimoto, S. Kusano, K. Takahashi, T, Sasaki, T. Kikuchi and N. Harada: Phys. Plasma **24** (2017) 072703.
[16] J. R. Lakowicz: Topics in Fluorescence Spectroscopy (1994).
[17] T. H. Maiman, R. H. Hoskins, I. J. D'Haenens, C. K. Asawa, and V. Evtuhov: Phys. Rev. **123** (1961) 1151.
[18] NIST Atomic Spectra Database Lines Form.
[19] R. Redmer: Phys. Rev. E **59** (1999) 1073.
[20] S. Kuhlbrodt, B. Holst and R. Redmer: Contrib. Plasma Phys. **45** (2005) 73-88.

Characteristic of Surrounding Gas-Fed Atmospheric Pressure Plasma Jet and its Application to Surface Treatment

Tetta Mitani, Kazuki Watanabe, and Hiroaki Ito

Graduate school of science and engineering for education, University of Toyama, Toyama 930-8555, Japan

ABSTRACT

We have developed the surrounding gas-fed plasma jet using a double coaxial glass tube to increase and control the production of active species in the plasma jet. Two gas flows can introduce independently into the tube and the gas and plasma flows interact outside of the glass tube. The developed plasma jet was compared with the conventional plasma jet with single glass tube by using optical emission spectroscopy. With an outer nitrogen (N_2) and an inner helium (He) gas flows, emission lines of nitric oxide, the first negative and second positive system bands of N_2 were observed, while emission line of nitric oxide was not observed in the single glass tube. The double coaxial glass tube makes a laminar flow and enhances the effective reaction area, resulting in energetic nitrogenous productions. We also evaluated the hydrophilic property of polyethylene terephthalates treated by the surrounding gas-fed plasma jet.

Keywords

Atmospheric pressure plasma jet, dielectric barrier discharge, optical emission spectroscopy, surface treatment

1. Introduction

In recent years, an atmospheric pressure plasma jet (APPJ) has attracted tremendous attention in various research fields. The low-temperature plasma like atmospheric pressure plasma is characterized by its ion and neutral species being close to room temperature, whereas it generates a variety of active components like charged particles, radicals, and reactive as well as excited species [1]. Therefore, it is possible to realize valuable tools for surface treatment without any heat damage, but with high chemical reactivity [2]. Due to the operation at atmospheric pressure, APPJs can also be used for application in biomedicine field, such as chronic wound healing [3, 4], skin disease [5], tooth bleaching [6], sterilization [7], and cancer treatment [8]. These applications strongly depend on plasma-generated reactive oxygen species and reactive nitrogen species. In order to meet the requirements of research and industrial application, it is very important for APPJs to increase productions of reactive species.

It has been shown that the production of reactive species could be enhanced in many ways, such as oxygen addition [9], water vapor addition [10], and other gas addition [11]. The mixing ratio, however, was below only a few percent due to the negative reactions for stable plasma discharge.

We have developed a surrounding gas-fed plasma jet with a double coaxial glass tube for the increase of radical productions [12]. The double coaxial glass tube can make a laminar flow by introducing an additional gas flow in parallel to core gas flow. The laminar-flow APPJ can control the flow rates of two gases separately using independent injection ports. This mechanism is expected to extend the plasma jet length with a guiding effect by the surrounding gas flow. Therefore, the increase of the jet length leads to an improvement of the effective reaction area for Penning effect related to the production of radical species. In this study, we observed the emission spectra of the surrounding gas-fed plasma jet and evaluated the fundamental characteristics of the laminar flow APPJ by comparing with the conventional APPJ. In addition,

we evaluated the hydrophilic property of stainless steels and polyethylene terephthalates (PETs) treated by the surrounding gas-fed plasma jet.

2. Experimental Setup

Figure 1 shows a cross-sectional view of a double coaxial glass tube and the schematic diagram of an experimental setup. The glass tube consists of inner and outer glass tubes and the size of each tube is shown in Table 1. There are two independent paths for central and surrounding gas flows. With this double coaxial structure, two different gases can introduce into the glass tube and can control each flow rate independently. The inner glass tube has a flange to prevent from arcing between electrodes and is used as a dielectric barrier. The copper films are wrapped to both sides of the flange of the inner tube as an electrode. The sinusoidal voltage generated by a step-up transformer of 7.5 kV with a frequency of 20 kHz was applied to the electrodes to induce the dielectric-barrier discharge. Voltage and current signals applied on the APPJ were measured by a high voltage probe (P6015A, Tektronix, Inc.) and a current transformer (4100, Pearson Electronics, Inc.) through a digital oscilloscope (Tektronix TDS2024B).

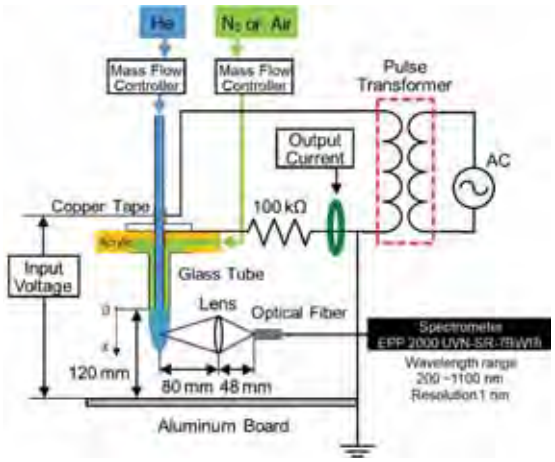

Fig. 1 Cross-sectional view of the double coaxial glass tube and experimental setup.

Table 1 Size of each glass tube

Tube type	Inner dia.	Outer dia.	Length
Inner	6 mm	9 mm	142 mm
Outer	13 mm	15 mm	39 mm

Helium (99.99 %) gas was used for an inner gas flow to produce the core plasma, and nitrogen gas was used for a surrounding gas flow. Each flow rate was controlled by a mass flow controller (8500MC-S3-1-2, KOFLOC Co., Ltd.). Helium gas was passed through the inner path with a flow rate of 5 L/min and the plasma was produced by the dielectric-barrier discharge. On the other hand, N_2 gas was passed through the outer path with 0−10 L/min.

We used the optical emission spectroscopy to measure at different positions in free jet region by using a spectrometer (EPP2000, StellarNet Inc.) in a wavelength range of 200−1000 nm with a typical full width at half maximum of 2.5 nm. The Emission spectra with an exposure time of 0.4 s are taken from the side of jet perpendicularly with a distance ranging from 0 to 50 mm measured from the jet exit. Emissions from a spot area with a diameter of 1 mm in the plasma jet, i.e., effective spatial resolution in the experiment, were focused into the optical fiber connecting to the spectrometer by using a double-convex lens with the focal length of 30 mm. The spectral distribution of the emission spectra of the APPJ was measured by moving the optical fiber from a tip of the glass tube toward the grounded aluminum board with the step of 2 mm.

3. Results and Discussion

3.1 Characteristics of Laminar APPJ

Figure 2 shows the comparison of the optical emission spectrum of the He/N_2 mixed gas plasma jet with single glass tube and the laminar plasma jet observed at X = 16 mm. In the case of the single He plasma jet with the flow rate of 5 L/min and mixing rate of 1.8 % shown in Fig.2 (a), it shows a typical distribution of emission spectrum from a He-based APPJ. In other words, emissions from He I transition, N_2 corresponding to the second positive system (N_2 2nd p.s.: C $^3\Pi_u \rightarrow$ B $^3\Pi_g$) transitions, N^+ corresponding to the first negative system (N_2 1st n.s.: B $^3\Pi_g \rightarrow$ A $^3\Sigma_u$) transitions were observed at 706 nm, in the ranges of 310−360 nm, and 390−470 nm, respectively. In addition, emissions from hydroxyl radical (OH) was observed at 309 nm. In the case of the laminar plasma jet shown in Fig.5 (b), the emission

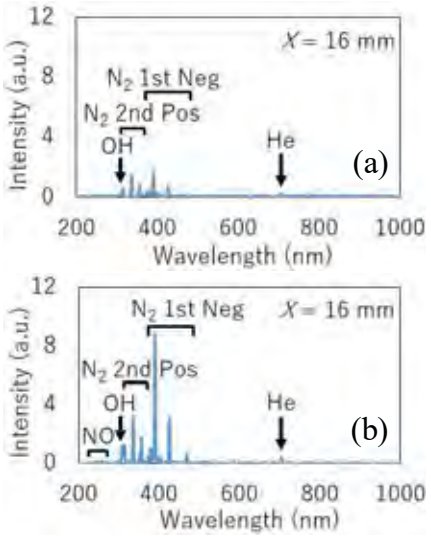

Fig. 2 Typical emission spectra of (a) He/N_2 mixed gas APPJ with single glass tube and (b) He-N_2 laminar APPJ observed at X = 16 cm.

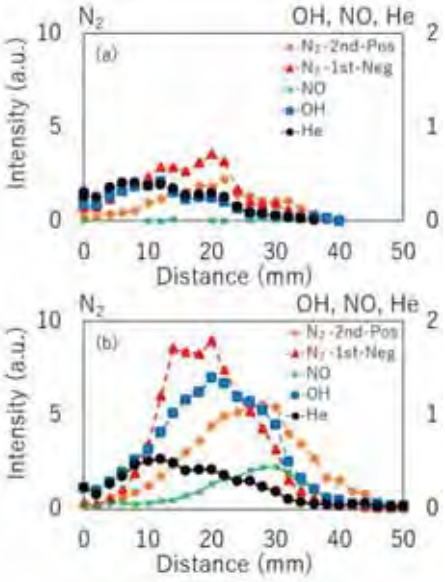

Fig. 3 Dependence of intensity for each emission line on distance from the tip for (a) He/N_2 mixed gas APPJ and (b) He-N_2 laminar APPJ

spectra has almost the same as the He/N_2 plasma jet shown in Fig. 2(a), but emissions from NO corresponding to γ–system ($A\ ^2\Sigma^+ \rightarrow X\ ^2\Pi_{1/2}$) transitions was observed in the ranges of 200-300nm. Here, the flow rates of inner He and surrounding N_2 gases are 5 and 4 L/min, respectively. It turns out from Fig.5 that each emission intensity except He line in the laminar plasma jet is higher than the He/N_2 plasma jet. We consider that the main reason that emissions from NO were observed only in the laminar He–N_2 plasma jet relates to the increase of energetic nitrogenous productions.

Figure 3 shows the dependence of the intensity for each emission line on the distance from the tip, i.e., He I 2p–3s transition at 707 nm, OH radical at 309 nm, NO radical at 245 nm, N_2 1st n.s. at 391 nm and N_2 2nd p.s. at 337 nm, respectively. Here, the flow rates are the same conditions as in Fig. 2. It turns out from Fig. 3 that although no significant change in the emission intensity for He between the He/N_2 mixed gas plasma jet and the laminar plasma jet was observed, the intensity of other emission lines in the He-N_2 laminar APPJ increased by about 3 times compared with the He/N_2 mixed gas APPJ. One can see that the plasma jet length of the laminar APPJ is longer than the He/N_2 APPJ by more than 10 mm. The result indicates that the surronding gas N_2 flow confines and guides the inner He plasma flow. This effect leads to the extension of the region of the effective interaction to produce excited N_2. Therefore, the double coaxial glass tube can produce excited N_2 rich plasma jet. Energy of the lowest metastable state (He I 1s2s) of He is 19.8 eV, and is suitable to produce upper states of N_2 2nd p.s. and N_2 1st n.s., respectively, by the energy transfer and Penning ionization. The upper states of N_2 2nd p.s. also could be produced by the decay of N_2^+. In the case of the He–N_2 APPJ, the surrounding N_2 gas interacts with a central He plasma jet at the interface of them outside of the glass tube, and then excited N_2 species are produced. The interaction of energetic N_2^+ with H_2O in ambient air contributes to the production of OH radicals. Therefore, each emission intensity of He, OH and N_2 1st n.s. (N_2^+) has peak at same distance as shown in Figs. 3(b). In addition, since N_2^+ has relation to the production process of NO [13], emissions from NO were observed only in the case of He–N_2 plasmas. We consider that the effect of the laminar flow APPJ, i.e., the increase of the effective reaction area and time, could lead to enhance the formation rate of NO drastically.

3.2 Results of surface treatment

The hydrophilicity improvement of polyethylene

Fig. 4 Photo of contact angle on (a) untreated, (b) pure He APPJ treated, and (c) He-N_2 laminar APPJ treated PETs

terephthalate (PET) was studied to evaluate effect of the laminar He–N_2 plasma jet on the surface treatment. The surface properties of the untreated and plasma-treated samples are characterized through water contact angle. Figure 4 shows the photos of the contact angle on the untreated PET and plasma-treated PET after the treatment time of 10 s. The PET surface is treated by the pure He APPJ with the He gas flow rate of 5 L/min and He-N_2 laminar APPJ with flow rates of 5 and 4 L/min for inner He and surrounding N_2 gases. Here, the treatment distance was at 20 mm. The contact angles were 80°, 37°, and 31° for the untreated, the pure He APPJ-treated and He-N_2 laminar APPJ-treated PETs, respectively. It turns out from Fig. 4 that the treatment of PET with the APPJ can improve the surface hydrophilicity.

Figure 5 shows the contact angle on the plasma-treated PET as a function of the treatment distance when the treatment time was fixed at 10 s. Here, the flow rates of each pure He APPJ and He-N_2 laminar APPJ are the same conditions as in Fig. 4. As seen in Fig. 4, the contact angle on the laminar APPJ-treated PET is smaller than the APPJ-treated one over the measured treatment distance, and has the minimum value around the treatment distance of 20 mm. As seen in Fig. 3(b), intense emission lines from N_2 second positive (337 nm), N_2 first negative (391 nm), and OH (309 nm) can be identified around 20 mm from tip. These energetic active species can bombard the PET surface under treatment and break the chemical bonds (C–C or C–H bond) on the surface, leading to the formation of radicals on the PET surface. Some of radicals can react with active species in the discharge regime, resulting in the creation of oxygen-containing polar groups on PET surface. These oxygen-containing polar groups allow much more H_2O molecules bond to them easily. Thus, the hydrophilicity improvement on PET surface is due to the introduction of oxygen-containing groups to the surface [14].

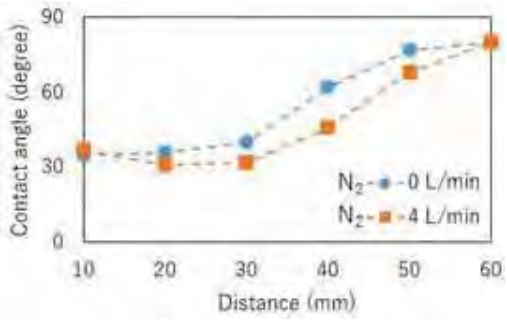

Fig. 5 Contact angle on PET as a function of treatment distance for (a) pure He APPJ, and (b) He-N_2 laminar APPJ

Figure 6 shows the contact angle on the plasma-treated PET as a function of the treatment time when the treatment distance was fixed at 20 mm. One can see that the water contact angle dramatically reduces in 10 s with the increase of treatment time. When the treatment time exceeds 10 s, the contact angle does not almost change and reaches saturation state.

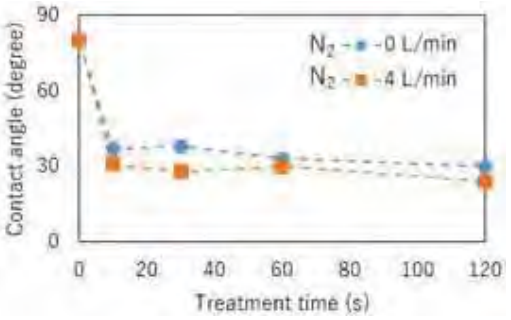

Fig. 6 Contact angle on PET as a function of treatment time for (a) pure He APPJ, and (b) He-N_2 laminar APPJ

4. Conclusions

We have developed a laminar flow type APPJ and evaluated its fundamental characteristics. The effect of the laminar flow enhances the effective reaction area and the time of inner and surrounding flow components in the APPJ, resulting in the increase of the production of energetic active species such as N_2 second positive (337 nm), N_2 first negative (391 nm), OH (309 nm), and NO (245 nm). The excited state in the core plasma is one of the important conditions to

determine the characteristics of the APPJ. Therefore, the laminar flow APPJs have a wide controllability by the choice of gas species, its flow rate and the feeding path. In addition, we evaluated the hydrophilicity improvement of polyethylene terephthalate (PET) treated by the APPJ. The treatment of PET films with the laminar APPJ can improve surface hydrophilicity more than that with the He APPJ. The increase of surface hydrophilicity is mainly due to the increase of energetic active species. The optimum value of water contact angle was 31° at treatment time of 10 s and treatment distance of 20 mm.

References

[1] V. Schulz-von der Gathen, *et al*., "Optical diagnostics of micro discharge jets", Contributions to Plasma Physics, vol.47, pp.510–519 (2007).

[2] K. Fricke, *et al*., "High rate etching of polymers by means of an atmospheric pressure plasma jet", Plasma Process. Polym, vol.8, pp.51–58, (2011).

[3] N. Barekzi and M. Laroussi, "Fibroblast cell morphology altered by low temperature atmospheric pressure plasma", IEEE Trans. Plasma Sci., vol.42, pp.2738–2739, (2014).

[4] S. Fathollah, *et al*., "Investigation on the effects of the atmospheric pressure plasma on wound healing in diabetic rats", Sci. Rep., vol.6, p.19144, (2016).

[5] G. Daeschlein, *et al*., "Antibacterial activity of an atmospheric pressure plasma jet against relevant wound pathogens in vitro on a simulated wound environment," Plasma Process. Polym., vol.7, pp.224–230 (2010).

[6] S. H. Nam, *et al*., "High-efficiency tooth bleaching using non-thermal atmospheric pressure plasma with low concentration of hydrogen peroxide", J. Appl. Oral Sci., vol.21, pp.265-270 (2013).

[7] S. Ikawa, *et al*., "Effects of pH on Bacterial Inactivation in Aqueous Solutions due to Low-Temperature Atmospheric Pressure Plasma Application", Plasma Process. Polym., vol.7, pp.33-42 (2010).

[8] D. B. Graves, "Reactive species from cold atmospheric plasma: Implications for cancer therapy", Plasma Process. Polym., vol.11, pp.1120–1127, (2014).

[9] W. Chen, *et al*., "Treatment of enterococcus faecalis bacteria by a helium atmospheric cold plasma brush with oxygen addition," J. Appl. Phys., vol.112, p.013304 (2012).

[10] N. Srivastava, *et al*., "Effects of water addition on OH radical generation and plasma properties in an atmospheric argon microwave plasma jet," J. Appl. Phys., vol.110, p. 053304 (2011).

[11] T. Yuji, *et al*., "Experimental Study of Temperatures of Atmospheric-Pressure Nonequilibrium Ar/N_2 Plasma Jets and Poly(ethylene terephtalate) - Surface Processing", Jpn. J. Appl. Phys., vol.46, pp.795-798, (2007).

[12] H. Ohashi, *et.al*., "A Versatile Laminar Flow Atmospheric Pressure Plasma Jet Using a Double Coaxial Glass Tube", IEEE Trans. Plasma Sci., vol.45, pp.2481-2485, (2017).

[13] D. D. Cleary, "Daytime high-latitude rocket observations of the NO γ, δ, and ε bands", J. Geophys. Res.: Space Phys., vol.91, pp.11337-11344 (1986).

[14] A. Sarani, *et.al*., "Surface modification of polypropylene with an atmospheric pressure plasma jet sustained in argon and an argon/water vapour mixture," Appl. Surf. Sci., vol.257, pp.8737-8741 (2011).

Evaluation of electrical characteristics of high-voltage SiC-MOSFET and development of inductive energy storage pulsed power generator

Yuki Hasegawa, Katsuyuki Takahashi, Koichi Takaki, and Kenji Fukuda*

Iwate University

**National Institute of Advanced Industrial Science and Technology, Advanced Power Electronics Research Center*

ABSTRACT

Electrical characteristics of a silicon carbide (SiC)-MOSFET with blocking voltage of 3.3 kV were evaluated and inductive energy storage (IES) pulsed power generator was developed. The experiment to evaluate was carried out using a circuit of a capacitor and a resistor. The maximum pulsed current of 165 A, the fall time of stabilized at 20 ns at a large current of 20 A and more, on-resistance 80 mΩ were obtained. IES pulsed power generator is consisted of the SiC-MOSFET employed as opening switch, a capacitor, and a pulsed transformer. The maximum output of 24.8 kV and full width at half maximum of 118 ns were obtained with an input voltage of 240 V and a charging time of 2 μs. The output pulse energy was 9.77 mJ corresponding to 31.9 % of the input energy with a load resistance 1 kΩ.

Keywords

Pulsed power, Silicon carbide, MOSFET

1. Introduction

Plasma application technology by high-voltage pulsed discharge is attracting attention for the removal of environmental pollutants such as nitrogen oxides (NOx) and organic compound[1][2]. Pulse discharge develops in two main phases; streamer corona discharge propagation phase and glow-like discharge . When a high positive voltage is applied to a center electrode (i.e., anode), a small luminous zone called a streamer head, develops from the center electrode to the outer electrode (i.e., cathode). The streamer head reaches the cathode and generates an ionized filament that bridges the gap between the anode and cathode. This initial phase of streamer propagation is called the "primary streamer". After the arrival of the primary streamer at the cathode, a subsequent streamer develops from the anode toward the cathode, is called a "secondary streamer" or a "glow-like discharge". The characteristics of the primary and secondary streamers are quite different. The primary streamer includes a relatively large number of high-energy electrons to dissociate molecules such as oxygen and nitrogen with high efficiently [3]. To inhibit the transition to glow-like discharge, the pulsed power generator simultaneously realizes a high-voltage output and a short pulse generation time is required[4].

Conventional triggers mounted on pulsed power generator have been used spark gap switches utilizing dielectric breakdown of air. However, it is difficult to implement in application fields because it has switch deterioration and operation instability. In order to solve this problem, researches are being carried out to apply semiconductor power devices having a semi-permanent lifespan and easy to control to triggers[5]. Although high capacitive semiconductor can obtain high output energy, its switching time is slow.

MOSFET is a kind of semiconductor, it is a relatively small capacity and high-speed device. Previously, further improvement in that capacity was achieved by devising the structure[6]. However, realization of further performance is extremely difficult based on the physical property value of the conventional Silicon (Si) material. Silicon carbide (SiC) has been much attention as a high- performance material replacing Si. SiC is known to have a bandgap of about 3 times, a dielectric breakdown electric field of about 10 times and a thermal conductivity of about 3 times higher than that of Si. There are shown that has high-temperature operation, low loss characteristics and high exhaust heat respectively[7][8].

In this research, the characteristics of SiC-MOSFET developed by Tsukuba Power Electronics Constellations (TPEC) with blocking voltage 3.3 kV[9] is evaluated to develop a pulsed power generator capable of realizing both high output voltage and ultra-short pulses. The characteristics of the inductive energy storage (IES) pulsed power generator using the SiC-MOSFET as switching device are also evaluated.

2. Experimental Setup

Figure 1 shows the schematics of evaluation circuit for the switching characteristics. Capacitive energy is stored in the capacitor of the capacitance C_B via the resistor R of 500 kΩ from the DC stabilized power supply V_{DD}. When the pulsed signal from a gate driver is applied between gate and source of the MOSFET, the MOSFET is turned on and the energy stored in the C_B is discharged through the resistor R_L. The drain-source voltage v_{DS} is measured using the voltage probe (Tektronix, P6015A) and the i_D is measured using a current transformer (Pearson, MODEL 2877).

Figure 2 shows the schematics of evaluation circuit for on-resistance of MOS-FET. The circuit consists of two MOSFETs connected in series. The drain of the lower MOSFET (M2) is connected to the source of the upper MOSFET (M1) , and the source is grounded. A gate driver is connected to the gate of M1 and DC 20 V is applied to the gate of M2. In order to calculate time change of the on-resistance $r_{DS(ON)}$, when M1 is switched, the v_{DS} ($v_{DS(ON)}$) is measured using the

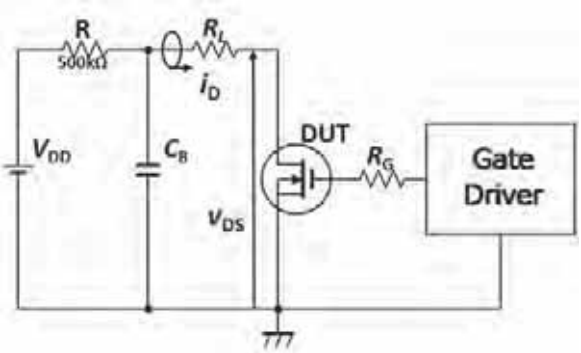

Fig. 1 Schematics of evaluation circuit for switching characteristics

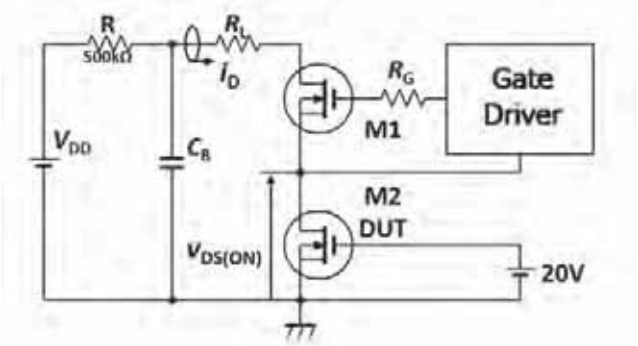

Fig. 2 Schematics of evaluation circuit for on-resistance characteristics

voltage probe (Tektronix, TPP1000) and the i_D was measured using a current transformer (Pearson, MODEL 2877). The C_B was 0.22 μF, the R_G was 510 Ω, and the pulsed width of the signal was 5 μs.

3. Results and Discussion

3.1 Switching characteristics

Figure 3 shows the waveform of i_D as for various V_{DD}. R_L is shortened. The C_B is 16.4 mF, the gate resistance R_G is 10 Ω, and the pulsed width of the signal is 50 μs. The peak value of i_D increases with increasing V_{DD}. When V_{DD} was 80 V, it has saturated at 165 A without failure.

Figure 4 shows the waveforms of v_{DS} and i_D when the MOS-FET is turned on and off. The C_B was 0.22 μF and the pulsed width of the signal was 250 ns. The V_{DD} is 3 kV and R_L is 150 Ω. The time required to reach from 90 % to 10 % at turn-on of v_{DS} is defined as rise time, and 10 % to 90 % at turn-off of v_{DS} is defined as fall time. The rise time and the fall time are 31 n and 22 ns, respectively, under this condition. Figure 5 shows the rise time and the fall time as a function of

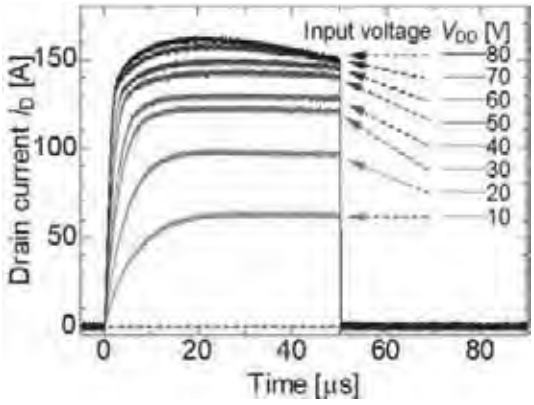

Fig. 3 Waveforms of drain current for various Input voltage

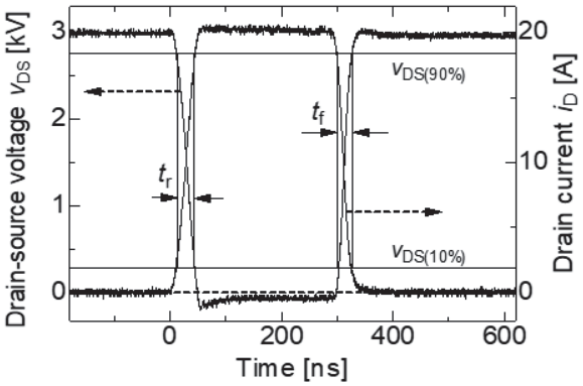

Fig. 4 Waveforms of drain-source voltage and drain current

R_L and i_D with V_{DD} of 3 kV. The rise time increases with increasing the R_L; on the other hands, the fall time decreases. When the i_D is higher than 20 A, the fall time has a constant value and is 20 ns. The switching time is about one order faster than a large capacity device like IGBTs[10]. Since the drain-source stray capacitance of the drift region is charged through R_L, the fall time of the MOSFET depends on the R_L. Therefore, the MOS-FET is suitable for the large cut-off current in a short time with heavy loading.

3.2 On-resistance characteristics

Figure 6 shows the waveforms of $v_{DS(ON)}$ and i_D and $r_{DS(ON)}$ calculated by $v_{DS(ON)}$ and i_D when the V_{DD} is 3 kV and R_L is 50 Ω. Because the resolution of the measurement system is not enough, $r_{DS(ON)}$ is calculated at the off-state of switching. The $r_{DS(ON)}$ does not change during turning on is a very low value of 0.08 Ω. Figure 7 shows the $r_{DS(ON)}$ as a function of input voltage and current. The $r_{DS(ON)}$ is independent

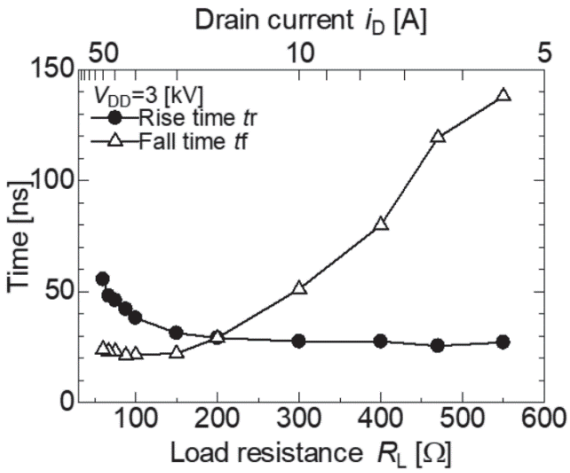

Fig. 5 Rise and fall times as a function of load resistance

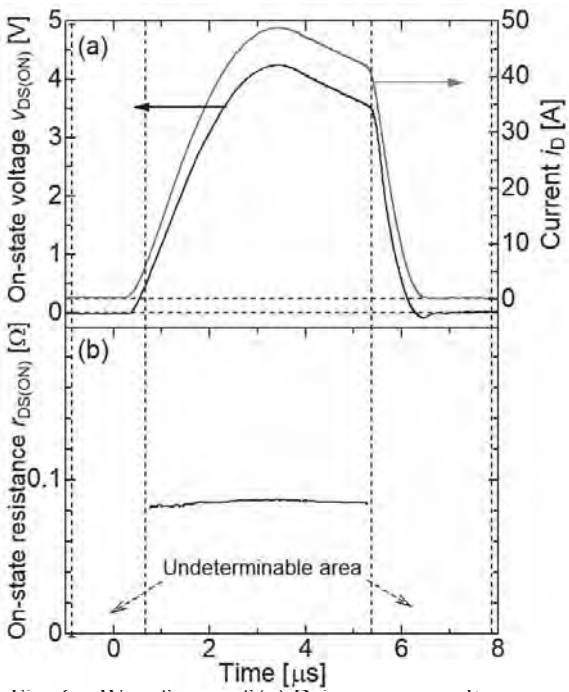

Fig. 6 Waveforms of (a) Drian-source voltage and drain current (b) calculated time change the on-resistance

of input voltage and current . From this, it can be seen that low loss is expected in the on-state and easy to loss calculation.

4. IES pulsed power generator

According to the electrical characteristics evaluation results, the device is suitable for an opening switch because its low on resistance and rapid current cut-off. In this study, an inductive energy storage (IES)

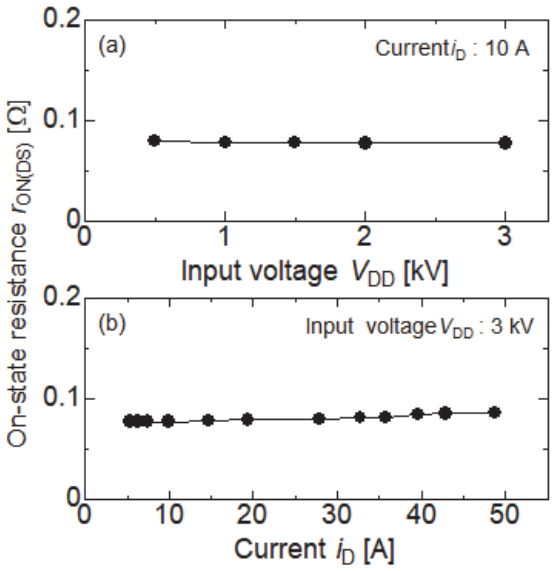

Fig. 7 On-resistance as a function of (a) Input voltage (b) current

pulsed power generator using SiC-MOSFET as an opening switch is developed. Figure 8 shows the schematics of the IES pulsed power generator. The primary circuit consists of energy storage capacitor C_B, a transformer and SiC-MOSFET. The C_B was using 12 μF. The transformer consists of a magnetic core (Hitachi Metals, FT-3H, cross section area $2.6*10^3$ mm^2, magnetic path length $3.2*10^3$ mm) with the turn ratio 2:20. AC/DC converter and a rectifier is used to reset the transfer with continuous current. During the SiC-MOSFET switch is closed, the charge stored in the capacitor flows through the transformer and MOSFET, and the inductive energy is stored in the inductance of the pulse transformer. When the MOSFET switch is opened, the current interrupted. As the results, pulsed voltage appears at the secondary circuit of the transformer.

Figure 9 shows the waveforms of the current flows the primary circuit i_{L1}, v_{DS}, the voltage across the primary transformer v_{L1}, the output voltage of secondary transformer. i_{L1} and output current i_O are measured using a current transformer (bergoz, CT-D1.0-B), v_{DS}, v_{L1} and v_O are measured using voltage probes (Tektronix, P5100, Testec, TT-SI 9010 and Tektronix, P5100 respectively.) The V_{DD} is 3 kV, a charging time is 2 μs and the R_G is 1 Ω or 20 Ω. In the case of R_G of 1 Ω, i_{L1} has maximum value of 52 A and

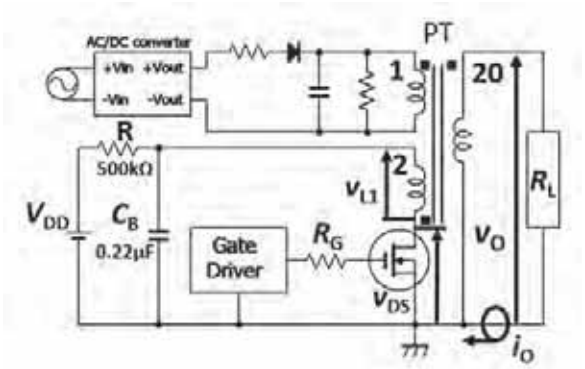

Fig. 8 Schematics of inductive energy storage pulsed power generator using SiC-MOSFET

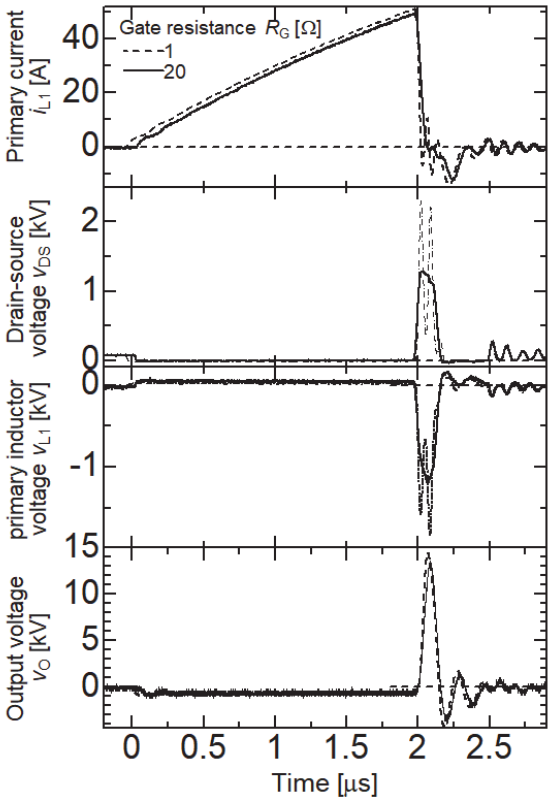

Fig. 9 Waveforms of the current flows the primary circuit i_{L1}, v_{DS}, the voltage across the primary transformer v_{L1}, the output voltage of secondary transformer.

is interrupted with the fall time of 24 ns. The maximum value of the v_{DS} and v_{L1} are 2.5 kV and 1.9 kV respectively. The full width at half maximum (FWHM) of v_{DS} and v_{L1} are both 32 ns. The maximum value of v_O is 15 kV. FWHM of v_O is 86ns and is longer than that of v_{DS} due to a plurality of induced voltage on the primary side. In the case of R_G of 20 Ω, The maximum value of the v_{DS} and v_{L1} are both 1.3 kV. The maximum value of v_O is 13 kV and the FWHM is 84

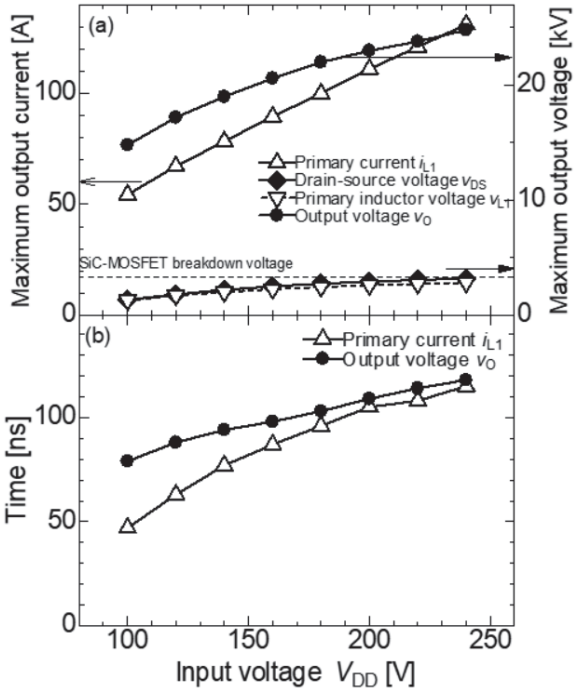

Fig. 10 (a) The maximum values of i_{L1}, v_{DS}, v_L and v_O, and (b) fall time of i_{L1} and FWHM of v_O, as a function of V_{DD}.

ns. The rise time and cut-off speed decrease with increasing R_G, the plurality of induced voltage is suppressed. Therefore, although the maximum value of v_{DS} decreases, maximum value and FWHM of v_O is independent to R_G.

Figure 10 shows (a) the maximum values of i_{L1}, v_{DS}, v_L and v_O, and (b) fall time of i_{L1} and FWHM of v_O, as a function of V_{DD}. The maximum value of them are increases with increasing V_{DD}. When V_{DD} is 240 V, the maximum values of i_{L1}, v_{DS} and v_O are 131 A, 3.2 kV, 25 kV respectively. The FWHM of v_O is 118 ns, which is longer than when V_{DD} is 100 V.

Figure 11 shows the energy consumed in the primary circuit u_1 and that in R_L, u_O, as a function of R_L. u_1 is calculated by integrating electric power obtained by the voltage across the C_B and i_{L1} over time. u_O is calculated by integrating the electric power obtained by the v_O and i_O over time. u_O is divided into a charging period, $u_{O(ON)}$, and after current interrupt, $u_{O(OFF)}$. $u_{O(ON)}$ decreases with increasing R_L because the impedance of secondary side of transformer increases. The $u_{O(OFF)}$ has a maximum value, 9.77 mJ corresponding to 31.9 % of the input energy with a load resistance 1 kΩ, when R_L is 1 kΩ because the

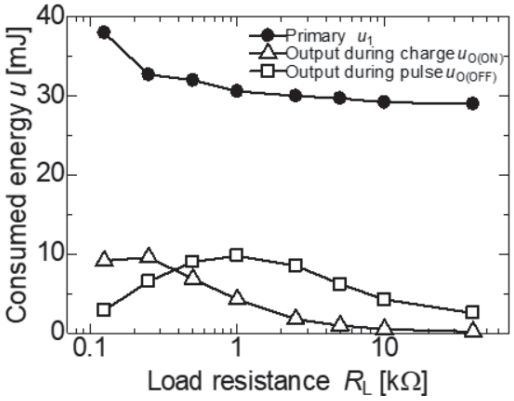

Fig. 11 the energy consumed in the primary circuit and that in load resistance before and after current interrupt as a function of load resistance

impedance of primary and secondary sides after current interrupt is matched.

5. Conclusions

In this research, the electrical characteristics of SiC-MOSFET is evaluated and IES pulsed power generator using SiC-MOSFET is developed. This device can be conducted a large pulsed current of 165 A. Also, fall time is as short as 20 ns with large pulsed current. The on-resistance is 0.08 Ω. The maximum output voltage and FWHM of The IES pulsed power generator are 25 kV and 118 ns, respectively. The output pulse energy was 9.77 mJ corresponding to 31.9 % of the input energy with a load resistance 1 kΩ.

Acknowledgments

Part of work this work has implemented under a joint research project of Tsukuba Power Electronics Constellations (TPEC).

References

[1] T. Namihira et al., "Improvement of NOx Removal Efficiency Using Short-Width Pulsed Power", *IEEE Trans. Plasma Sci.*, **28**, 2, pp.434-442 (2000)

[2] M. A. Malik et al., "Water purification by electrical discharges", *Plasma Sources Sci. Technol.*, **10**, 1, pp.82-91 (2001)

[3] Y. Teramoto et al., "Streamer Propagation of

Positive and Negative Pulsed Corona Discharges in Air", *IEEE Trans. on Plasma Sci.*, **39**, 11, pp.2218-2219 (2011)

[4] D. Wang et al., "Development of higher Yield Ozonizer Based on Nano-Seconds Pulsed Discharge", *ISSN J. Adv. Oxid. Technol.*, **13**, 1, pp.71-78 (2010)

[5] D. Gerber et al., "Gate Unit With Improved Short-Circuit Detection and Turn-off Capability for 4.5-kV Press-Pack IGBTs Operated at 4-kA Pulse Current", *IEEE Trans. on Plasma Sci.*, **41**, 10, pp.2641-2648 (2013)

[6] B. J. Baliga, "A new vertical power MOSFET structure with extremely reduced on-resistance", *IEEE Trans. Electron Devices*, **38**, pp.1568-1575 (1991)

[7] B. J. Baliga, "Power Semiconductor Device Figure of Merit for High-Frequency Applications", *IEEE Electron Device Lett.*, **10**, 10 pp.455-457 (1989)

[8] H. Okumura, "Present status and Future Widegap semiconductor High-Power Devices", *Jpn. J. Appl. Phys.*, **45**, 10A, pp.7565-7586 (2006)

[9] T. Tsuji et al., "3300 V-class 4H SiC Implantation-Epitaxial MOSFETs with Low Specific On-resistance of 11.6 $m\Omega cm^2$ and High Avalanche Withstanding Capability", *Materials Sci. Forum*, **858**, pp.962-965 (2016)

[10] D. Gerber et al., "Gate Unit With Improved Short-Circuit Detection and Turn-Off Capability for 4.5 kV Press-Pack IGBTs operated at 4-kA Pulse Current", *IEEE Trans. on Plasma Sci.*, **41**, 10, pp.2641-2648 (2013)

Development of an Induction Accelerator Cell Driver Utilizing 3.3 kV SiC-MOSFETs

Katsuya Okamura, Daiki Kumamoto*, Ken Takayama

High Energy Accelerator Research Laboratory

**Nagaoka University of Technology*

ABSTRACT

Pulse switching characteristics of newly developed 3.3 kV SiC-MOSFET were investigated. With supply voltage of 2.5 kV and the load resistor of 100 Ω, rise time T_r and fall time T_f were 76 ns and 88 ns respectively. Thereafter, they were provided for a prototype switching power supply (SPS). In the SPS, drain to source voltage waveform exhibits a extremely spike-free switching waveform. Also, continuous mode switching tests were attempted. As a result, repetition of 150 kHz was confirmed with a power loss of 63 W/device.

.

Keywords

Induction Accelerator, Switching Power Supply, SiC-MOSFET

1. Introduction

A novel synchrotron called an induction synchrotron (IS) was developed at KEK in 2006 [1]. In the IS, charged particles are accelerated by pulse voltages driven by switching modulators employing high-power high –repetition –rate semiconductor switches. The switches are turned on and off by gate signals corresponding to the revolution frequency of the ion bunches. As the ion beam is accelerated to nearly light speed, maximum switching frequency reaches up to MHz order.

A switching pulse supply (SPS) that generates bipolar pulses is one of the key technologies for the IS. The rating of SPS is roughly 2.5kV-20A-1MHz. To accomplish these requirements, we adopted 7 series connected Si-MOSFET for the switches of the 1st generation SPS. However, it was too large and complicated for practical accelerators. Therefore we started to develop the next generation SPS utilizing silicon carbide (SiC) devices, because they have inherently excellent properties in high electric fields such as durability, high-speed switching and high-temperature resistance [2, 3].

In the early stage of this research, we had focused on JFET devices, which had been considered to be more practical in those days. Consequently we developed a high power discrete package [4] and succeeded to demonstrate a beam acceleration experiment [5] utilizing SiC-JFETs. However, development of MOSFET devices has been dramatically progressed recently. Thereby 3.3 kV class MOSFET has been already demonstrated [6,7]. In this paper, we describe the pulse switching test results of a prototype SiC-MOSFET developed by Rohm Co., Ltd and test results of a prototype switching power supply utilizing them.

2. Switching Performance of The Prototype Device

Firstly, we conducted the switching performance test of the prototype device. The device package utilizes general TO-247 package with a minor conversion so that it could ensure the higher voltage rating. The switching test was performed with resistive loads since the load is not inductive in the induction accelerator driver. Fig. 1 and Fig. 2 shows the switching waveforms and switching losses with

† katsuya.okamura@j-parc.jp

various values of load resistors at constant V_{DD} of 2.5 kV respectively. With load resistors of 220 Ω and 100 Ω, on voltages are extremely low, whereas on voltage exceeds 200 V with such a heavy load of 50 Ω. Moreover, switching losses also steeply increase. With the load resistor of 100 Ω, rise time T_r and fall time T_f were 76 ns and 88 ns respectively.

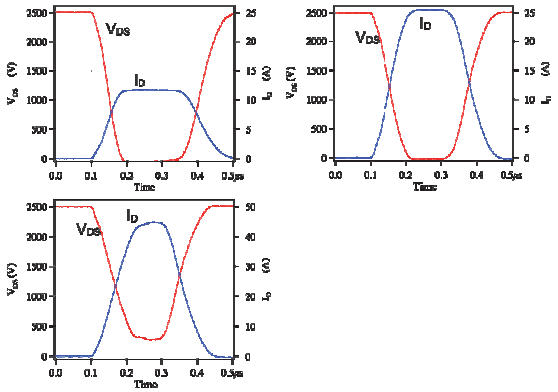

Fig. 1 Switching waveforms of a prototype 3.3 kV MOSFET. Top left: R_L=220 Ω, top right: R_L=100 Ω, botom : R_L=50 Ω.

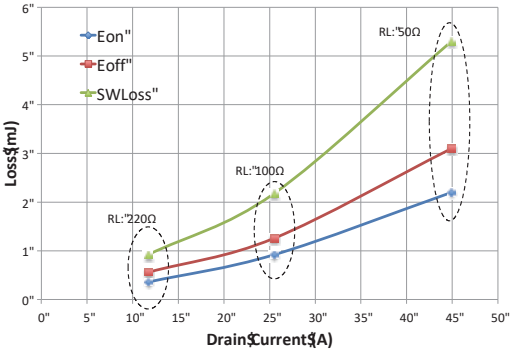

Fig. 2 Switching losses (V_{DC}=2500 V).

Making a SPICE model of the device was also attempted. A simulation circuit and the test results are shown in Fig.3 and Fig. 4, respectively. The device model was made according to the SPICE Level 3 MOSFET model. The parameters are shown in Fig. 3. Comparing the waveforms of Fig. 4 to those of Fig. 1, fairly good agreement are obtained between them with load resistance of 220 Ω and 100 Ω. However, non-negligible difference is observed with the load resistance of 50 Ω. This difference may come from transient temperature rise.

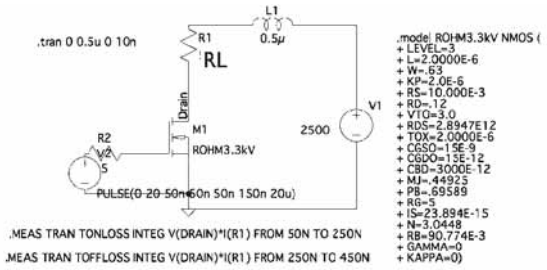

Fig. 3 SPICE Simulation Circuit.

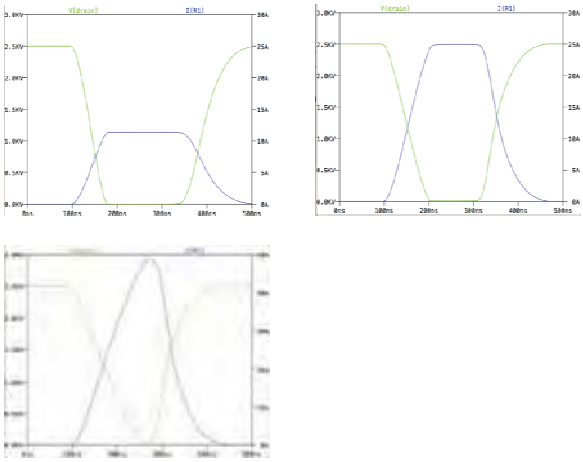

Fig. 4 Simulation Result utilizing LTSPICE. Top left: R_L=220 Ω, top right: R_L=100 Ω, botom : R_L=50 Ω.

3. Prototype Switching Power Supply

3.1 Design

A pulse generator that has a circuit topology of H bridge circuit was fabricated with this prototype MOSFET, the circuit diagram is shown in Fig. 5. MOSFETs are mounted on water-cooled heat sink and interconnection between devices are done with laminated copper plates insulated by Nomex® paper.

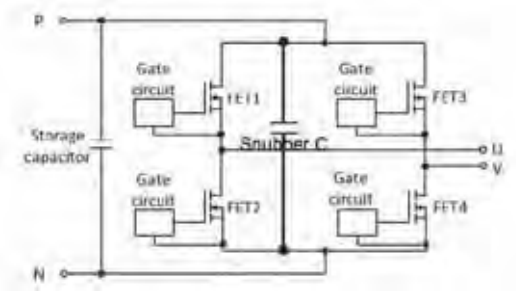

Fig. 5 Circuit Diagram of the Prototype Switchig Power Supply.

3.2 Single Shot Performance

At first, the SPS was tested with single shot mode operation mode. In such a high speed switching circuit, switching surge voltage is one of the most crucial issues. Therefore spike voltage between drain and source of each FET was measured with the dc rating voltage of 2.5 kV. Figure 6 shows the waveforms of drain to source voltage and output current. As a consequence, even in the highest case, spike voltage was 2532 V corresponding to only 101.3 % of the dc voltage. Low stray inductance structure of laminated bus enables such a low spike voltage only with a simple snubber capacitor.

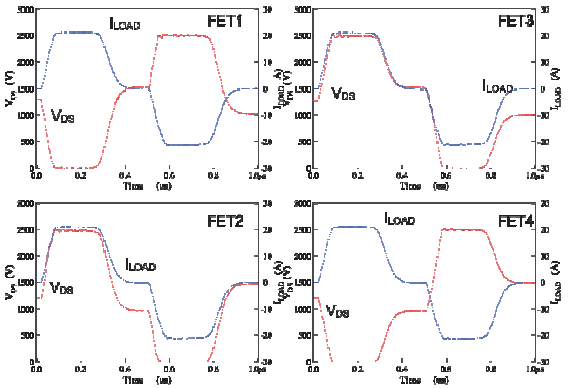

Fig. 6 Drain-Source Voltage of the FETs and Output Current Waveforms in Single Shot Mode with DC Voltage of 2500 V and Load Resistance of 120 Ω.

3.3 Continuous Operation

After the single shot mode operation, continuous mode operation, with load resistance of 80 Ω was executed with water-cooling. Drain to source voltage, drain current, and case temperature of FET2 was measured in the experiment. Figure 7 and Fig. 8 shows the waveforms of the drain to source voltage and the drain current and the load current with dc voltage of 2000 V at 150 kHz operation, respectively. From the voltage and current waveform, the switching losses were calculated, which are shown in Fig. 9. The turn-on loss of 250 μJ and the turn-off loss of 170 μJ were confirmed, therefore average loss is estimated to be 63 W at 150 kHz operation. At the same time, the temperature rise of the device was 10-13 K. From this results, we expect operation with higher frequency.

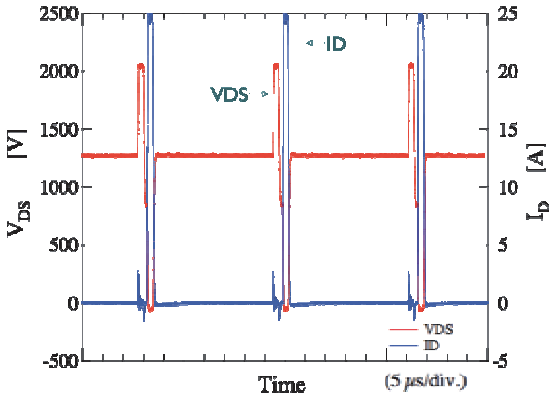

Fig. 7 Switching Waveforms of FET 2 during 150 kHz Operation.

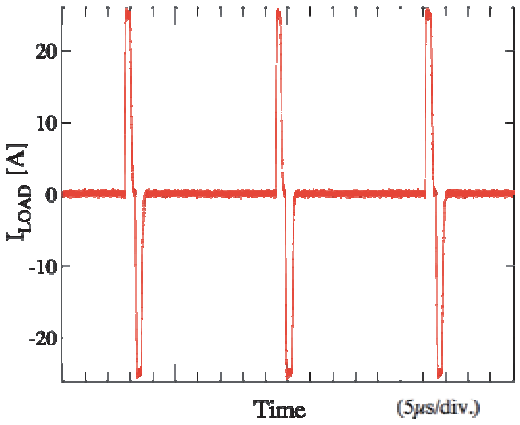

Fig. 8 Output Current during 150 kHz operation.

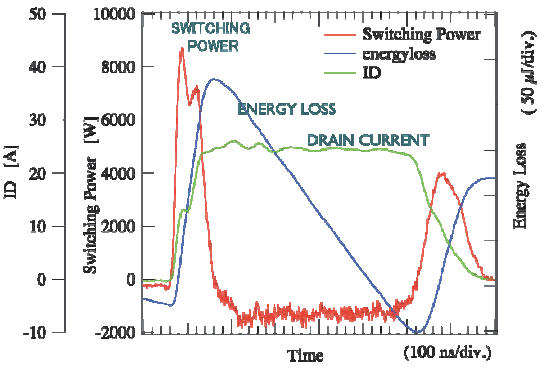

Fig. 9 Switching Loss

4. Summaries and Future Plan

Pulse switching characteristics of newly developed

3.3 kV SiC-MOSFET were tested and they were provided for a prototype switching power supply (SPS). The SPS consists of only 1 device in its arm and can output 2.5 kV pulse. A 150 kHz continuous mode operation was confirmed. These successful results encourage us to develop an ultra-compact pulsed power supply the induction acceleration system for future accelerators, such as the fast cycling hadron driver for cancer therapies [8], induction microtron for giant cluster ions [9], and giant cluster ion inertial fusion driver [10]. Moreover, custom high-power packages with bi-directional heat-exhaust technology will also enable MHz order continuous mode operation [11].

Acknowledgement

The authors wish to thank Rohm Co., Ltd for provision of prototype MOSFETs.

References

[1] K. Takayama et al., Phys. Rev. Lett., 98, no.5, pp.054801(1)-054801(4) (2007).
[2] H. Okumura, Japanese J. Appl. Phys. vol.45, no.10A, pp. 7565-7586, Oct. 2006.
[3] K. Shenai et al., IEEE Trans. Electron Devices, vol. 36, no. 9, pp. 1811-1822, Sep. 1989.
[4] K. Okamura et al., IEEE Trans. Plasma Sci., vol.40, no.9, p. 2205 (2012)
[5] K. Okamura et al., IEEJ Trans. FM., Vol. 134, pp. 402-409, 2014.
[6] S. Mori et al., Proc. of the 2016 28th ISPSD, June 12-16, 2016, Prague, Czech Republic.
[7] T. Tsuji et al., Materials Science Forum, Vol. 858, pp. 962-965, 2016
[8] Leo K.W. et al., Phys. Rev. ST-AB 19, 042802 (2016).
[9] K.Takayama et al., Phys. Rev. ST-AB 18, 050101 (2015).
[10] K. Takayama and K. Horioka, HIF2016, Astana (2016).
[11] K. Okamura et al., Material Science Forum 778-780, pp. 883-886 (2014)

Study of the 13 kV class High-Voltage SiC-MOSFET for a Pulsed Power Supply of the KEK Digital Accelerator

Daiki Kuamoto, Katsuya Okamura*,
Hidenori Kitai**, Hisato Michikoshi**, Kenji Fukuda**

Department f Electrical, Electronics and Information Engineering, Nagaoka University of Technology, Nagaoka, Japan

**Accelerator Laboratory, High Energy Accelerator Research Organization, Tsukuba, Japan*

***Advanced Power Electronics Research Center, National Institute of Advanced Industrial Science and Technology, Tsukuba, Japan*

ABSTRACT

Switching characteristics of the 13 kV SiC-MOSFET developed by Tsukuba Power Electronics Constellations (TPEC) was investigated. With the conditions of drain voltage of 10 kV and load resistance off 1 kΩ, turn on loss E_{on}, turn off loss E_{off}, ris time T_r and fall time T_f were 1.7 mJ, 1.1 mJ, 64 ns, 75 ns, respectively. As to gate charge characteristics, required electric charge to increase gate source voltage until 20 V was about 100 nC.

Keywords

Key Words (MOSFET, Silicon carbide, Pulse power supply, Digital Accelerator)

1. Introduction

The KEK digital accelerator (KEK-DA) is schematically shown in Figure 1. The KEK-DA is a first cycling induction synchrotron driven by induction acceleration systems. This feature is distinguished from the conventional radio frequency (RF) synchrotron [1]-[2]. The induction acceleration system consists of a DC power supply, a switching power supply, and an induction acceleration cell, which is a one-to-one pulse transformer. Two induction acceleration cells are independently used to confine and to accelerate the beam. A degree of freedom of the beam handling of induction synchrotron greatly improved compared with that of an RF synchrotron [3]. Meanwhile, other pulse power devices are used in the KEK-DA. The Eintzel lens chopper and electrostatic injection kicker are among them. Si-MOSFETs are used in the Marx circuit to generate the gate voltage for the Einzel lens and SI-Thyristors are employed in the discharge circuit of the ES injection kicker system instead of Thyratron [3]-[6]. KEK have been continuously devoting to further improvement of characteristics of these switching devices such as lower switching loss, higher withstand voltage, and high-power operation. This present work is on this context. Such improvement should lead to a compact pulse power supply and their easier maintenance.

Fig. 1. Outline of the KEK Digital Accelerator

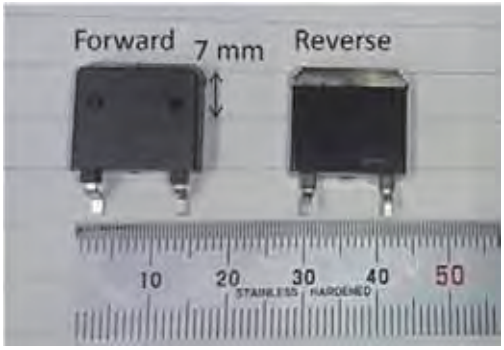

Fig. 2. Photograph of a 13kV-SiC MOSFET

2. SiC-MOSFET

Although the researches aiming for replacing thyratrons by semiconductor devices have been energetically done, its progress has been gradually because the performance of conventional Si power devices are limited by its material property. On the other hand, Silicon Carbide (SiC) is expected to bring the innovative progress because it has excellent properties of (1) three times larger band gap, (2) ten times higher electrical breakdown strength, (3) twice higher melting point, and (4) three times higher thermal conductivity as compared to those of Si. Also the SiC-MOSFET that has the withstand voltage of over 10 kV has been developed recently [9]. Switching characteristics of 13 kV class SiC-MOSFET developed by Tsukuba Power Electronis Constellation (TPEC) is described in this paper. Figure 2 shows the external view of the device, which is similar to the standard TO-268-2L package.

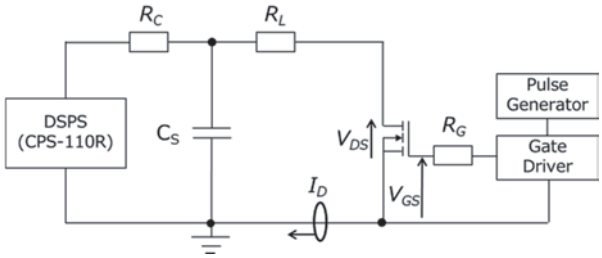

Fig. 3. Evaluation circuit

3. Experimental Setup

Figure 3 shows the test circuit. The circuit consists of a DC power source, a charging resistor R_C (47 MΩ), a load resistor R_L (200 Ω-10 kΩ), a gate registor (6.2 Ω), a storage capacitor C_S (2000 pF), a gate driver and a pulse generator. Drain-source voltage and drain current were measured utilizing a high voltage probe (LeCroy, PPE20kV) and a current transformer (Pearson, MODEL 6585), respectively. The

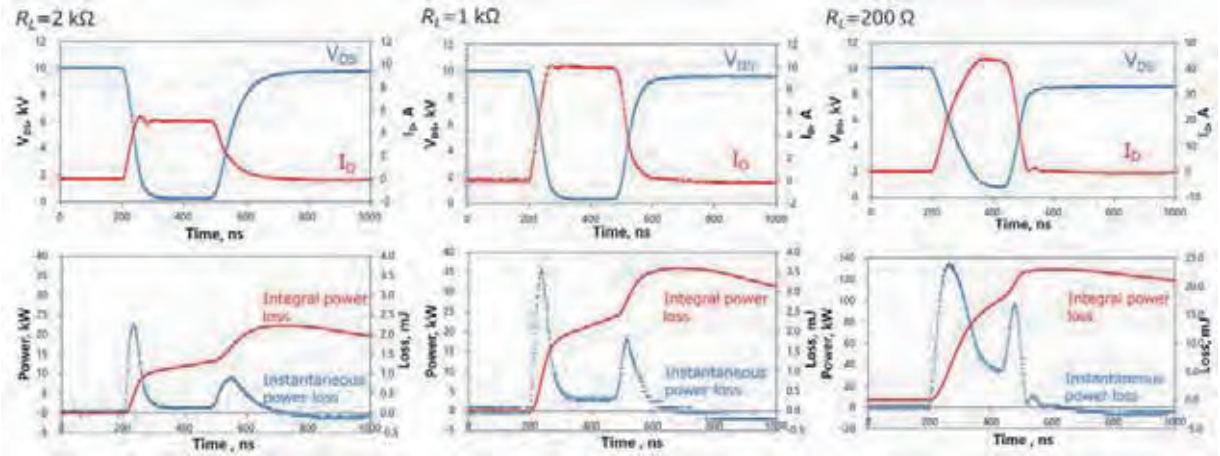

(a) (b) (c)

Fig.4 Switching waveforms V_{DS} = 10 kV drain-source Voltage and drain current (upper), instantaneous power loss and integral power loss(under) (a) R_L = 2 kΩ, (b) R_L = 1 kΩ, (c) R_L = 200 Ω

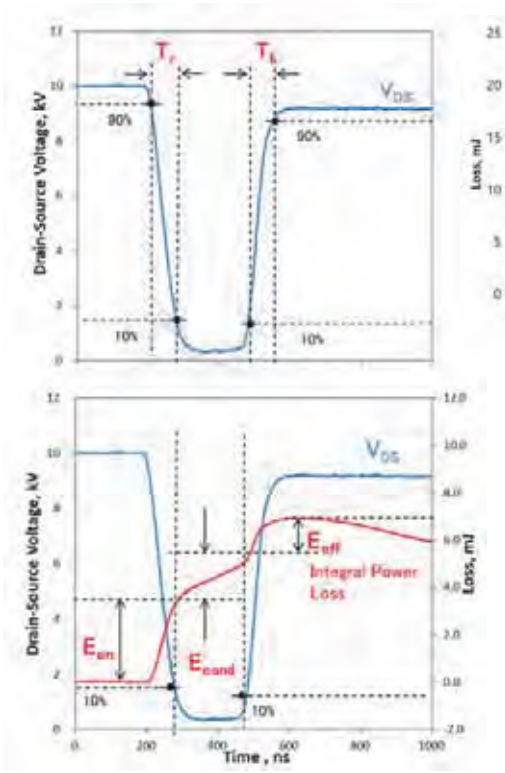

Fig.5 Definition of switching time (upper) and switching loss (under)

maximum drain-source voltage was 10 kV. Switching characteristics of the SiC-MOSFET was investigated under a single-shot mode.

4. Switching Characteristics

4.1 Load Resistor Dependency

Figure 4 shows switching waveforms and switching losses under various load resistors. With the load resistance of 2 kΩ, an oscillation is observed in the rising portion of the drain current. It is considered

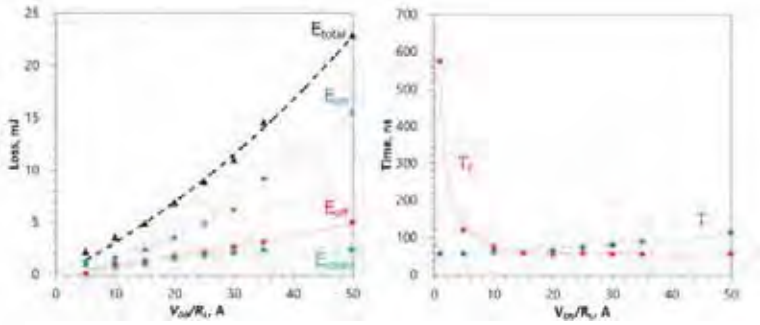

Fig. 6. (a) Switching Loss, (b) Switching time

that a stray inductance of the circuit and the parasitic capacitance of the MOSFET caused this oscillation. With the load resistance of 200 Ω, a peak drain current of 43.5 A was observed.

Figure 5 shows definition of the rise time, the fall time, the turn-on loss, the turn-off loss and the conduction loss. Figure 6 shows switching loss and switching time characteristics, where horizontal axes are drain currents normalized by V_{DS}/R_L. The turn on Loss E_{ON} shows a rapid increase with the drain current, whereas turn off loss E_{off} does not show strong dependency. As to switching time, the falling time T_f shows a rapid decrease with the drain current up to 10 A, thereafter saturates. It is considered that the falling time depends on the time constant decided by the charging resistance R_C and the parasitic capacitance C_P below the drain current of 10 A, whereas it depends on the device characteristics itself above 10 A.

If the device can be considered as an ideal switch

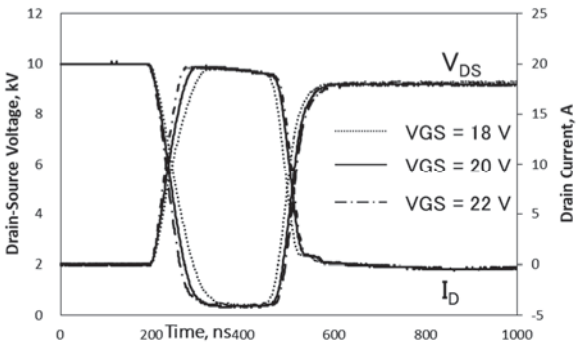

(a)

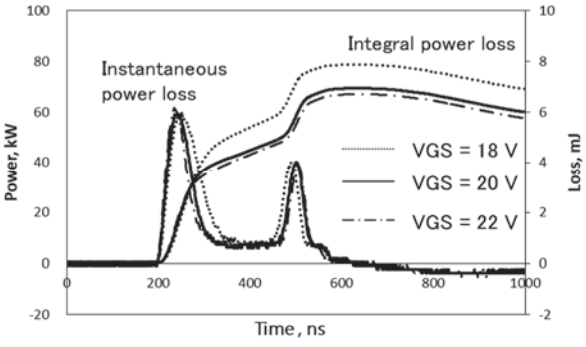

(b)

Fig.7. (a) Drain-Source Voltage, Drain Current, (b) Instantaneous power loss and integral power loss

V_{DS} = 10 kV, R_L = 500 Ω

and a parallel-connected capacitance C_P, the voltage recovery is described by equation (1).

$$V=V_0\left\{1\text{-}\exp\left(\frac{\text{-t}}{RC}\right)\right\} \quad (1)$$

The falling time T_f and the parasitic capacitance C_P can be calculated using equation (2) and (3) as follows.

$$T_f = -RCln0.9 - RCln0.1 \approx 2.20RC \quad (2)$$

$$C = \frac{T_f}{2.20R} \quad (3)$$

Substituting the value of 575 ns for RC of 10 kΩ and 120 ns for 2 kΩ, we obtain 26.1 pF and 27. 3 pF, respectively. Therefore we concluded that the parasitic capacitance of the device is around 27 pF.

4.2 Gate-Source Voltage Dependency

Figure 7 shows switching waveforms and switching losses for various gate-source voltages and figure 8 shows the switching loss and the switching time characteristics as a function of the gate-source voltage. Turn on loss E_{on} and the falling time T_f decreases with increasing gate-source voltage. From these results it is concluded that the gate voltage should be higher than 20 V.

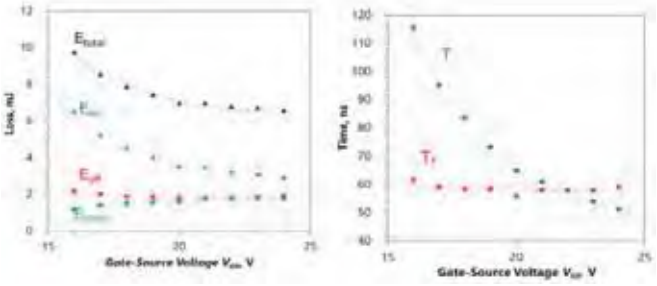

Fig. 8. (a) Switching Loss, (b) Switching Time
V_{DS} = 10 kV, R_L = 500 Ω

4.3 Gate Charge Characteristics

A gate charge characteristic is one of the important factor for designing a gate driver circuit. The gate charge can be calculated using equation (4).

$$Q_G = \int I_G dt \quad (4)$$

where Q_G: gate charge, I_G: gate current.

We measured gate current from the voltage of gate resistance. Figure 9 shows the gate-source voltage

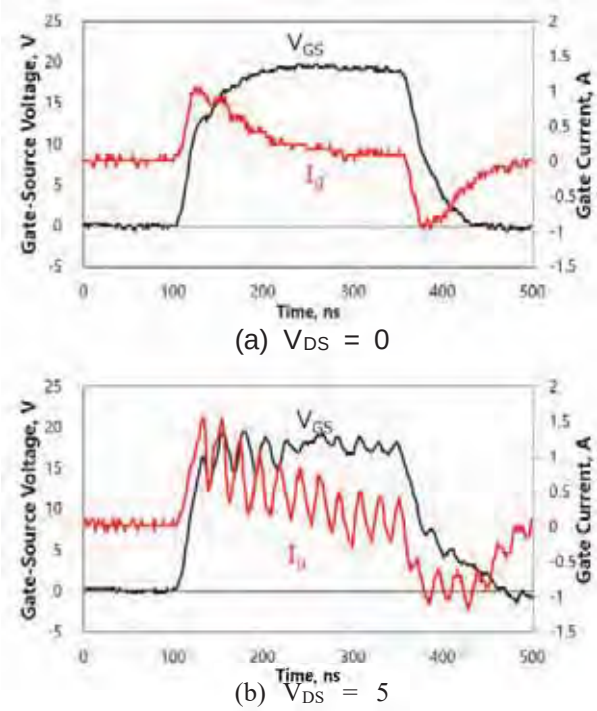

(a) V_{DS} = 0

(b) V_{DS} = 5

Fig. 9. Gate-Source Voltage waveform and Gate Current waveform (a) V_{DS} = 0 V, (b) V_{DS} = 5 V

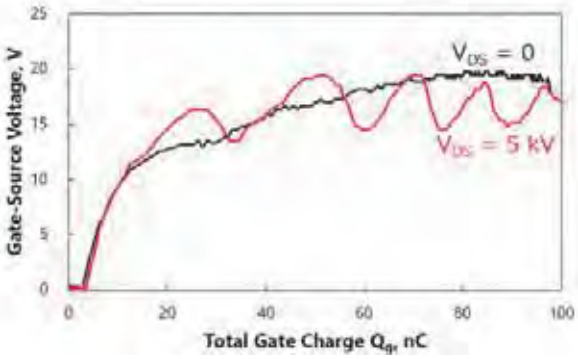

Fig. 10. Total Gate Charge Characteristics

and gate current waveforms with (a) V_{DS}=0 and (b) V_{DS}=5 kV. And Fig. 10 shows the gate-charge vs gate-source voltage characteristics. In the case of drain-source voltage of 5 kV, oscillation is observed. It is considered that the stray inductance of gate wiring and the input capacitance caused this oscillation. In Fig. 10, we observed the Miller effect around 20 nC of gate charge and confirmed 100 nC is needed to fully drive this device.

5. Summary

We have investigated switching characteristics of newly developed 13 kV SiC-MOSFET, where V_{DS}, R_L and V_{GS} were 10 kV, 1kΩ and 20 V, respectively. Consequently we obtained E_{on}, E_{off}, E_{cond}, T_r and T_f of 1.7 mJ, 1.1 mJ, 0.8 mJ, 64 ns, 75 ns, respectively. The maximum drain current of 43.5 A was confirmed. As to the results of gate charge characteristics, required electric charge to increase gate-source voltage until 20 V was about 100 nC.

References

[1] K.takayama et al., "KEK digital accelerator and its beam commissioning", Proceedings of IPAC2011,WEOBA02 (2011)

[2] T. Iwashita, T. Adachi, K. Takayama, K. W. Leo, T. Arai, Y. Arakida, M. Hashimoto, E. Kadokura, M. Kawai, T. Kawakubo, T. Kubo, K. Koyama, H. Hakanishi, K. Okazaki, K. Okamura, H. Someya, A. Takagi, A. Tokuchi, and M. Wake, "KEK Digital Accelerator", Phys. Rev. ST-AB, vol. 14, 071301 (2011).

[3] 堀岡 一彦, 佐々木 徹, 高山 健, 長谷川 純, "パルスパワー技術による Warm Dense Matter 実験", J. Plasma Fusion Res. Vol.86, No.5, pp.269-281(2010)

[4] T. Adachi, T. Arai, K. W. Leo, K. Takayama and A. Tokuchi, "A solid-state Marx generator driven Einzel lens chopper", Rev. Sci. Instrum., vol.82, 083305 (2011)

[5] T. Adachi, T. Kawakubo, "Electrostatic injection kicker for the KEK digital accelerator", Phys. Rev. ST-AB, vol 16, 053501 (2013)

[6] H. Kobayashi, L. Xingung, T. Kawakubo, T. Adachi, "SI-Thyristor matrix array driven electrostatic injection kicker for the KEK digital accelerator and beam dynamics analysis of injection", PASJ2015, THP026 (2015)

[7] 佐久川貴志, 浪平隆男, 勝木淳, 秋山秀典, 長田俊宏, 小金澤竹久, "半導体パルスパワー電源のプラズマ応用機器への適用", プラズマ・核融合学会誌, Vo.81, No. 5, pp.350-354(2005)

[8] H. Okumura, "Present Status and Future Prospect of Widegap Semiconductor High-Power Devices", J. J. Appl. Phys., Vol.45, No.10A, pp. 7565-7586 (2006)

[9] 吉川明彦, 赤﨑勇, 松波弘之,: 「ワイドギャップ半導体 –あけぼのから最前線へ–」, 培風館, pp. 273 (2013)

Observation of development of pulsed discharge inside bubble under water using ICCD camera

Shota Kobayashi, Yusei Nagata*, Masahiro Takeda, Katsuyuki Takahashi, Koichi Takaki, and Takao Namihira*

Iwate University

**Kumamoto University*

ABSTRACT

Development of discharge inside bubble in water is observed using two high speed gated ICCD cameras. A tungsten wire is inserted into a glass tube, which is immersed in water. The pulsed high voltage is generated using an inductive energy storage system pulsed power generator driven by SI-Thyristor. Two ICCD cameras with their optical axes perpendicular to each other are used to take two orthogonal images. The discharge propagates into the bubble from tip of the wire in the glass tube. Then, the discharge propagates along the bubble surface. The maximum length of discharge propagation decreases with increasing water conductivity. Indigo carmine, a common used organic dye, was used as chemical probe of active species produced by discharge inside bubble. The energy efficiency for indigo carmine decomposition in the water decreases with increasing water conductivity. These results show that the amount of active species consumed in loss reactions such as their recombination increases with decreasing the length of discharge propagation.

Keywords

Discharge inside Bubble, Discharge Propagation, Hydroxyl Radical, Conductivity

1. Introduction

A pulsed discharge plasma in water and in contact with water have been attracting much attention as a promising technology in various fields such as agriculture [1], healthcare [2] and environmental remediation [3,4]. The pulsed discharge plasma enables the instantaneous production of a non-thermal plasma with various chemical species such as hydroxyl radical. Since hydroxyl radical is a powerful oxidizing agent, it plays an important role in decomposition of chemical compounds and sterilization of bacteria in water [3-5].

The discharge plasma treatment has several advantages; however, its high running cost of discharge plasma system is a major obstacle in the applications, which is still an open question. The energy efficiency of treatment is affected by structure of discharge reactor [6]. In general, the energy efficiency for water treatment decreases with increasing conductivity of the water, because of an increase in the energy dissipation by the ohmic loss, which does not contribute to the production of the chemical species [7,8]. To solve this problem, gas–liquid separated reactors have been proposed and their performance has been evaluated experimentally [9-12]. In the reactors, discharge plasma is generated at the electrode placed in the gas phase such as an inside of gas bubble to decrease the ohmic loss, and propagates along the surface of the bubble in the solution [13,14].

In the case of the discharge plasma inside bubble, the chemical species such as hydroxyl radical are produced by plasma in the gas phase. The hydroxyl radical at the water interface dissolve into the water, which contribute to decomposition of soluble compounds in water [15]. Hydroxyl radical is mainly

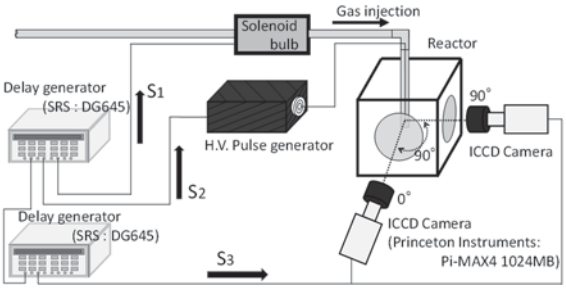

Fig. 1. Schematics of discharge observation system using two ICCD cameras

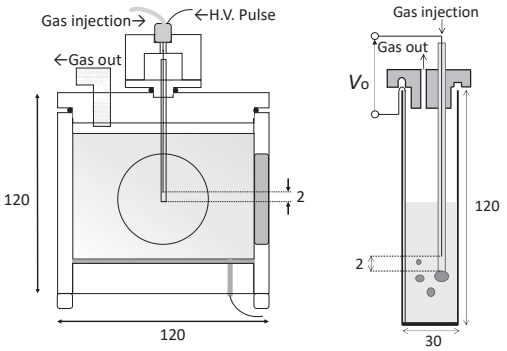

Fig. 2. Schematics of discharge reactors for (a) observation of discharge using ICCD camera and (b) decolorization of organic dye

lost by a self-recombination reaction that produces hydrogen peroxide and the decomposition reaction of hydrogen peroxide [16-18]. The energy efficiency for waste water treatment decreases with increasing hydroxyl radical consumed in the loss reactions. The loss reaction increases with increasing the local density of hydroxyl radical, affected by the discharge propagation.

In this study, development of discharge inside bubble in water is observed, and the relationship between the discharge propagation and the energy efficiency for the decomposition of chemical organic compounds in water is investigated. Two ICCD cameras with their optical axes perpendicular to each other are used to take two orthogonal images of discharge propagation. Indigo carmine, a common dye, is used as a chemical probe of hydroxyl radical to evaluate the amount of hydroxyl radical dissolved in the solution.

2. Evaluation test Setup

2.1 Discharge propagation

Figure 1 shows the schematic diagram of the discharge observation system using two ICCD cameras. The system consists of a discharge reactor, a solenoid valve (SMC, VQ21A1-5G-C6), an inductive energy storage system pulsed power generator using SI thyristor [19], two delay generators (Stanford Research Systems, DG645) and two ICCD cameras (Princeton Instruments, Pi-MAX4 1024MB). Figure 2 shows the schematic diagram of the discharge reactor for observation of emission spectra. The reactor consists of an acrylic vessel (100 mm in width, 100 mm in depth and 100 mm in height). The vessel has two quartz window (60 mm in diameter and 3 mm in thickness) on two side of the vessel. 700 mL of potassium nitrate solution is placed in the vessel. The conductivity of the solution is adjusted by adjusting concentration of potassium nitrate and is ranged from 2 to 1000 μS/cm. A glass tube (0.8 mm in inner diameter, in which the electrode of tungsten wire (0.2 mm in diameter) is inserted, is vertically immersed in the solution in the vessel. The electrode of the tungsten wire in the glass tube is placed above the water. The gap length between the tip of tungsten wire and the tip of glass tube is 2 mm. Argon gas (99.99 vol.% purity) is injected into the glass tube through the solenoid valve with the pressure of 0.1 MPa to generate a bubble a the tip of glass tube in the solution with a constant volume at a synchronized timing. The operation of the solenoid bulb is controlled by the delay generator. A stainless-steel (SUS304) board is sunk to the bottom of the glass vial and is connected to the ground. The pulsed voltage generated by a pulsed power generator is applied to the tungsten wire to generate the streamer discharge in the tube and the gas bubble. The streamer discharge is generated at the tip of wire and propagates into the bubble. The peak value of the pulsed voltage is ranged from 5 to 7 kV. The pulse repetition rate is fixed at 10 pps.

Two ICCD cameras are placed in front of the quartz windows with their optical axes perpendicular. The length between the cameras and the quarts windows is 100 mm. The procedures of taking flaming photographs of discharge inside bubble is as follows:

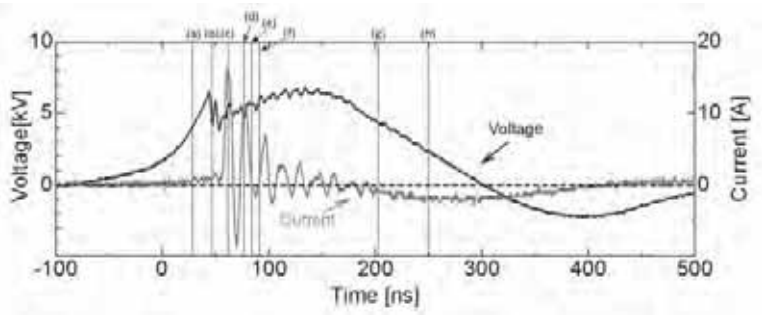

(a)

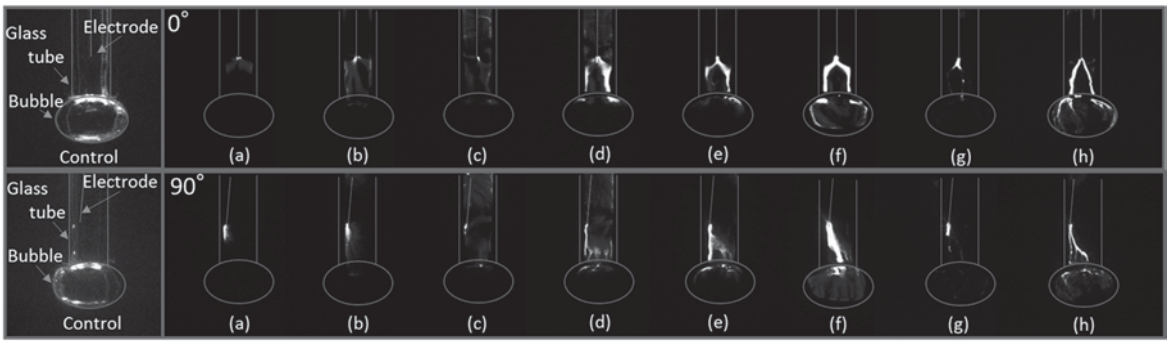

(b)

Fig. 3. (a) Waveforms of applied voltage and current and (b) flaming photographs of discharge inside bubble

.

The solenoid coil is operated with the signal (S1) and the gas bubble is generated at the tip of the glass tube. After 26 ms of S1, the pulsed voltage is applied to the wire electrode with the signal S2. Then, the gate signal S3 is input to the two ICCD cameras. The delay time between S2 and S3 is adjusted by the delay generator. The exposure time of the ICCD camera is fixed at 5 ns.

2.2 Decomoposition of dye solution

Figure 2 (b) shows the schematic diagram of the discharge reactor for decolorization of dye solution. The rector consists of a glass cylindrical vessel (120 mm in height and 30 mm in diameter). The electrode of tungsten wire in a glass tube as shown in figure 2 (a) is immersed in the solution. Indigo carmine solutions is prepared by dissolving indigo carmine (Wako Pure Chemical Industries, JIS special grade, Acid blue 74, CAS No. 860-22-0) in 30 mL of purified water at the concentration of 15 mg/L. The conductivity of the solution is adjusted by adding potassium nitrate and is ranged from 2 to 1000 μS/cm. The input energy per a pulse, impedance of the discharge and the discharge propagation is same as the that of the reactor as shown in figure 2 (a). The pulse repetition, the bubble volume and the delay between the signals are same with the discharge observation. The amount of the indigo carmine decomposition and the energy efficiency of the decomposition are evaluated after treatment time of 120 min. Concentration of hydrogen peroxide in the potassium nitrate solution is measured using PACKTEST (KYORITSU CHEMICAL-CHECK Lab., WAK-H2O2). PACKTEST provides a simple measurement of hydrogen peroxide by 4-aminoantipyrine visual colorimetric method with enzyme.

3. Results and Discussion

3.1 Discharge propagation

Figure 3 shows the waveforms of applied voltage and current flows the reactor and flaming photographs of discharge inside bubble in water. The photograph (control) shows the reactor without discharge taken at an exposure time of 1 ms. A small bubble is generated at the tip of the glass tube, which has a constant volume at the synchronized timing. As shown figure 3

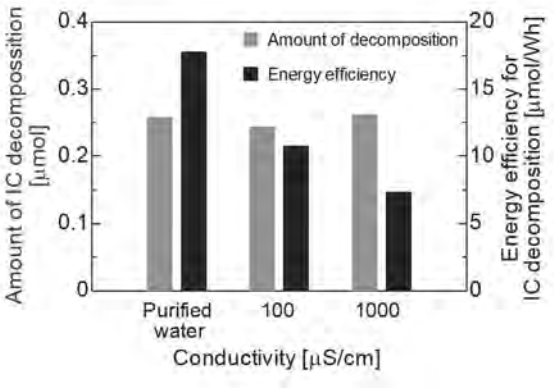

Fig. 4. Amount of decolorization of indigo carmine and energy efficiency for decolorization for various conductivity

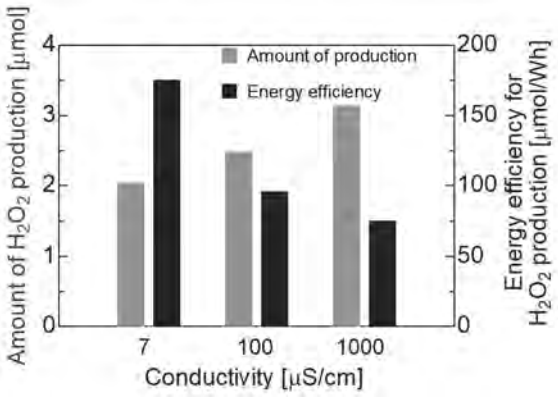

Fig. 5. Amount of hydrogen peroxide production and energy efficiency for production for various conductivity

(a), the corona discharge occurs at the tip of the electrode at the 4 kV of applied voltage due to the high electric field at the vicinity of the tip of the electrode. As shown in figure 3 (b), the discharge propagates to the tip of the glass tube along the surface of the glass tube. After the discharge reach to the tip of the glass tube, it propagates inside the bubble (figure 3 (d, e)) and has the maximum length as shown in figure 3 (f). Figure 3 (g) shows that the discharge extends into the bubble and the discharge around the wire is disappeared with polarity change of differentiation of the applied voltage as same manner of dielectric barrier discharge. After the decay of light emission from the discharge, as shown in figure 3 (g), the discharge between the wire and the inner surface of the glass tube occurs again with decrement of voltage and reverse current as shown in figure 3 (h).

As shown in the two orthogonal images, the discharge inside bubble propagates along the bubble surface. The maximum length of the discharge propagates on the bubble surface for various conductivities was estimated from the photograph that the discharge has maximum length as shown in figure 3 (f). The maximum length in the case of conductivities of 0, 100 and 1000 μS/cm are 9.0, 6.6 and 5.4 mm, respectively. The equivalent circuit of the water surface is expressed as the resistor and capacitor connected in parallel. The resistance of the resistor decreases with increasing conductivity. The decrease in the resistance enhances the leakage of the accumulated charge on the surface of the bubble, which causes the concentration of discharge current and decrease of electric field. Therefore, the discharge length decreases with increasing conductivity.

3.2 Decomposition of dye solution

Figure 4 shows the amount of indigo carmine decomposition and the energy efficiency for the decomposition. The amounts of indigo carmine decomposition with 120 min treatment in the cases of conductivities of 7, 100 and 1000 μS/cm are 0.26, 0.24 and 0.26 μmol, which shows the decomposition is independent of the conductivity. On the other hands, the energy efficiencies of the decomposition in the cases of conductivities of 7, 100 and 1000 μS/cm are 17.7, 10.7 and 7.3 μmol/Wh. The energy efficiency decreases with increasing the conductivity.

Figure 5 shows the amount and the energy efficiency of hydrogen peroxide production. The amount of hydrogen peroxide production increases with increasing conductivity. Since the almost hydrogen peroxide is produced by recombination reaction of hydroxyl radicals [20], the hydroxyl production by the discharges increases. The hydroxyl radical mainly contributes to indigo carmine decomposition [21]. As shown in figure 4, the amount of indigo carmine decomposition is independent with of conductivity. Therefore, the amount of hydroxyl radicals that dissolved into water and reacts with indigo carmine is also independent of the conductivity.

The hydroxyl radicals produced by the discharge inside bubble is dissolved in the water through the bubble surface, and react with solute in the solution. The discharge length on the bubble surface decreases with increasing conductivity. The hydroxyl radical is mainly produced by electron impact to water molecule in the discharge channel [22]. In the case of high conductive solution, hydroxyl radical is produced at the upper part of the bubble and the local concentration of hydroxyl radical increases. The increase of hydroxyl radical concentration increases recombination reaction and the decrease of the local concentration of indigo carmine at the vicinity of the bubble surface, which leads the decrease in the energy efficiency. The thermalization in the discharge channel increases the gas and water temperature, which could lead the decrease of reduction of hydroxyl radicals into the water. Furthermore, the ohmic loss in the solution increase with increasing conductivity [7,8]. Therefore, the energy efficiency decreases with increasing the conductivity.

4. Conclusions

Development of discharge inside bubble in water is observed using two high speed gated ICCD cameras. Two ICCD cameras with their optical axes perpendicular to each other are used to take two orthogonal images. The discharge propagates into the bubble from tip of the wire in the glass tube. Then, the discharge propagates along the bubble surface. The maximum length of discharge propagation decreases with increasing water conductivity. The energy efficiency for indigo carmine decomposition in the water decreases with increasing water conductivity. These results show that the amount of active species consumed in loss reactions such as their recombination increases with decreasing the length of discharge propagation.

References

[1] K. Takahashi *et al.*, "Development of Automatically Controlled Corona Plasma System for Inactivation of Pathogen in Hydroponic Cultivation Medium of Tomato", *J. Electrostat.*, **91**, pp.61-69, (2018).

[2] T. von Woedtke *et al.*, "Plasmas for medicine", *Phys. Rep.*, **530**, 4, pp. 291–320, (2013).

[3] Y. Huang *et al.*, "Escherichia coli inavtivation in water using pulsed discharge", *IEEE Trans. Plasma Sci.*, **44**, 6, pp. 2654-2655, (2016).

[4] K. Takahashi *et al.*,"Water remediation using pulsed power discharge under water with advanced oxidation process", *J. Adv. Oxidat.*, **15**, 2, pp.365-373, (2012).

[5] M. J. Kirkpatrick *et al.*, "Atmospheric pressure humid argon DBD plasma for the application of sterilization- measurement and simulation of hydrogen , oxygen, and hydrogen peroxide formation", *Int. J. Plasma Environ. Sci. Technol.*, **1**, 1, pp.96-101, (2007).

[6] M.A. Malik, "Water Purification by Plasma Which Reactors are Most Energy Efficient?.", *Plasma Chem. Plasma Process.*, **30**, pp.21-31, (2010).

[7] P. Lukes *et al.*, "Ultraviolet radiation from the pulsed corona discharge in water", *IEEE Trans. Plasma Sci.*, **17**, 2, 024012 (2008).

[8] T.H. Dang *et al.*, "Degradation of organic molecules by streamer disharges in water: coupled electrical and chemical measurement", *IEEE Trans. Plasma Sci.*, **17**, 2, 024013 (2008).

[9] K. Takahashi *et al.*, "Purification of High-Conductivity Water Using Gas–Liquid Phase Discharge Reactor", *IEEE Trans. Plasma Sci.*, **38**, pp. 2694 – 2700 (2010).

[10] S. Kawano *et al.*, "Influence of pulse width on decolorizaiton efficiency of organic dye by discharge inside bubble in water", *J. Phys.: Conf. Ser.*, **441**, 012007 (2013).

[11] D. Levko *et al.*,"Plasmas generated in bubbles immersed in liquis; direct current streamers versus microwave plasma", *J. Phys. D. Appl. Phys.*, **49**, 28, 285205, (2016).

[12] A. Hamdan *et al.*,"The effects of gaseous bubble composition and gap distance on the characteristics of nanosecond discharges in distilled water" *J. Phys. D: Appl. Phys.*, **49**, 24,

245203 (2016).
[13] K. Takahashi *et al.*, "Development of Pulsed Discharge inside Bubble in Water", *IEEE Trans. Plasma Sci.*, **39**, 11, pp. 2654-2655 (2011).
[14] K. Tachibana *et al.*, "Analysis of a pulsed discharge within single bubbles in water under synchronized conditions", *Plasma Sources Sci. Technol.*, **20**, 3, 34005 (2011).
[15] P. J. Bruggeman, *et al.*, "Plasma–liquid interactions: a review and roadmap" *Plasma Sources Sci. Technol.*, **25**, 5, 53002 (2016).
[16] F.D. Baerdemaeker *et al.*,"Efficiency of hydrogen peroxide production by ac capillary discharge in water solution", *J. Phys. D: Appl. Phys.*, **40**, 9 (2007).
[17] H. Hayashi *et al.*, "Comparison of OH-radical Concentration for Two Method Produced by Underwater Discharge", *I.J. PEST*, **10**, 1 (2014).
[18] Y.Y. Zhao *et al.*,"Hydroxyl radicals and hydrogen peroxide formation at nonthermal plasma-water interface", *IEEE Trans. Plasma Sci.*, **44**, 10, pp. 2084-2090 (2016).
[19] K. Takahashi *et al.*, "Estimation of Hydroxyl Radicals Produced by Pulsed Discharge inside Bubble in Water Using Indigo Carmine as Chemical Probe", *IEEE Trans. Plasma Sci.*, **46**, 3, pp.663-669 (2018).
[20] D.R. Grymonpré *et al.*,"Suspended activated carbon particles and ozone formation in aqueous-phase pulsed corona discharge reactors", *Ind. Eng. Chem. Res.*, **42**, 21, pp.5117-5134 (2003).
[21] H. Liao, D. Stenman *et al.*,"Study of Indigo carmine as radical probe in photocatalysis", *J. Photoch. Photobio. A*, **202**, pp. 86-91 (2009).
[22] R. Ono *et al.*,"Dynamics of ozone and OH radicals generated by pulsed corona discharge in humid-air flow reactor measured by laser spectroscopy", *J. Appl. Phys.*, **93**, 10, pp.5876-5882 (2003).

Spatial distribution measurement of liquid droplets generated in impulsed high voltage atomization

M. Nishio, A. Uchida and R. Kiyono

National Institute of Technology, Anan College, Tokushima, 774-0023, Japan

Abstract

Impulsed high voltage atomization experiment were carried out for comparison to electrostatic atomization. Reduction of mist size and increment of the number of mist droplets are required in order to maximize interactions between surrounding air and droplets. Spatial distributions of atomized droplets of water solution were measured by shadowgraph imaging with pulsed light source. From the comparison of histograms, impulsed high voltage atomization can generate more number of small size and less number of middle size.

Keywords

electrostatic atomization, impulsed high voltage, spatial distribution of droplets, shadowgraph

1. Introduction

Physical properties of fine liquid droplets vary easily by coalescence or disruption. Chemical properties of them vary also by mixing or volume change against fine solid particles. An operation that atomize liquid droplets (atomization or misting) can enlarge surface area and can also amplify interaction between droplets and air vapor under atmospheric pressure. Techniques with atomization are utilized in many fields such as an industry field, agricultural field, and so on [1–4]. Application examples include fuel injection in engines, spray painting for vehicle body, and fine particle generation by spray dryer. Approaches to generate fine droplets are categorized as nozzle method with pressure energy, jet method with vapor energy, wheel method with rotating energy, ultrasonic wave method with vibration method, evaporation and condensation method with thermal energy, and electrostatic method with electric energy.

Electrostatic atomization (for short, EA) requires no mechanical part, and can adjust atomization properties by changing applied voltage. Application examples of EA include moisturizing effect in air conditioners or electro-spraying for effective car-body painting and so on. Direct current high voltage is applied between nozzle electrode ejecting liquid solutions and a counter-electrode. If charged amount into a droplet is enough, three-dimensional cone, called as Taylor cone, is generated at the end of the nozzle electrode with a sharp tip. When a outward repelling force among supplied charges exceed an inward attracting force by surface tension, continuous disruption phenomena is caused by fluid-dynamical instabilities of liquid structures.

Hartman *et al.*, (2000) [4] indicated that theoretical disruption processes and experimental verification. According to it, more supplied charges into droplets caused stronger repelling force between charges remained on the surface, and the disruption mode changed from zero-ordered sausage-type instability to one-order kink-typer one. Obata *et al.*, (2015) [5] reported that rapid rise-time of applied impulse voltage enables to achieve short generation time of the Taylor cone in an atomization experiment with a impulsed high voltage power supply. Also, they showed that the number of Taylor cones increased in accordance with the amount of extra-charge.

The amount of current in the atomization circuit depends on the applied voltage and the resistance of electrolyte solution. More amount of electric charges supplied into droplets is required for less size of mist droplets and more numbers of mist droplets. In a single nozzle for atomization, applied voltage to the electrode will increase with effect of reflection of transmitting voltage wave. This enables to increase the amount of current injected droplets.

This study aims to achieve reduction of mist size and increment of the number of mist droplets with an application of impulsed voltage without change of intensity of voltage in order to maximize

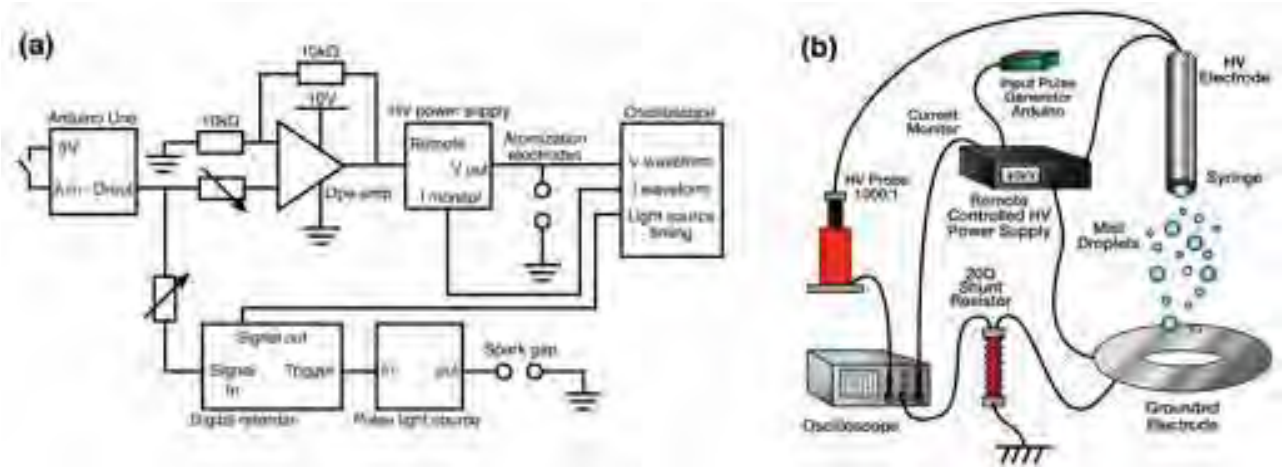

Fig. 1: circuit diagram and schematic diagram of impulsed high voltage atomization

interaction between surrounding air and droplets. In this study, both electrostatic and impulsed high voltage atomization (for short, IHVA) were conducted in order to reveal difference of mist size distributions in between the two types of voltage applying.

2. Experimental Setup

DC or impulsed high voltage was connected to spray nozzle of water solution to supply electric charges into droplets. Flow rates were adjusted by trimming dial of intravenous bag storing the solution. Flat-tip hollow stainless tube was used for the spray nozzle. Outer diameter of the tube was 0.5 mm. Opposite electrode was stainless metal having torus-shape. In the experiment of impulsed one, only one droplet was attached below the tip of hollow tube without adjustment of flow rate of the solution. Ethanol-water solution (50 wt. %) was used in both DC and IHV experiments.

DC high voltage power supply, MKS40KP (Maxellec Inc.), generates impulse high voltage in accordance with input voltage signal through its remote terminal. The power supply accept pulsed low-voltage signal from 0 to 10 [V] and generate corresponding value of pulsed high voltage from 0 to 40 [kV]. Because an one-chip microcomputer module, Arduino Uno, can produce only 5 [V], the input low-voltage signal to MKS40KP was amplified to 10 [V] by non-inverting amplifier circuit with an operational amp. Following four data were measured with digital phosphor oscilloscope: impulsed voltage waveform applied to the spray nozzle, voltage waveforms transmitted into the remote receive terminal of the high voltage power supply, current waveform of charge arrived at the opposite electrode after misting, and current waveform of the current supplied to spraying nozzle. Fig. 1 (a) shows circuit diagram of impulse high voltage generation. Fig. 1 (b) shows schematic diagram of power supplies and measurement devices.

Current waveforms were obtained by using a shunt resistor. When the small resistor was inserted serially in between the counter electrode and a ground cable, voltage drop was occurred in between both ends of shunt resistor (200 [Ω]). Current waveforms were obtained from the voltage drop value divided by resistance of the shunt resister.

Spatial distributions of atomized droplets were recored by pulsed light-source-type shadowgraph apparatus (NS400). This light source includes pulse generation circuit using a thyratron. The pulsed width was 50-80 ns. After generating pulsed light for shadowgraph, the light was parallelize by transmitting through first convex lens. At the target, droplets absorb enough amount of light intensity in accordance with their outer shapes. Second convex lens make the image concentrated at the focal point. These images were recorded with a single-lens reflex camera, α58 (Sony). Saved spatial droplet distribution images were analyzed with a image-analytics software, Image J. Its particle measurement function can measure area of cross-section of droplets and the number of them by droplet size category. The images were converted gray-scaled images, then were converted to binary images. Histogram data of them were categorized and showed that the difference between EA and IHVA.

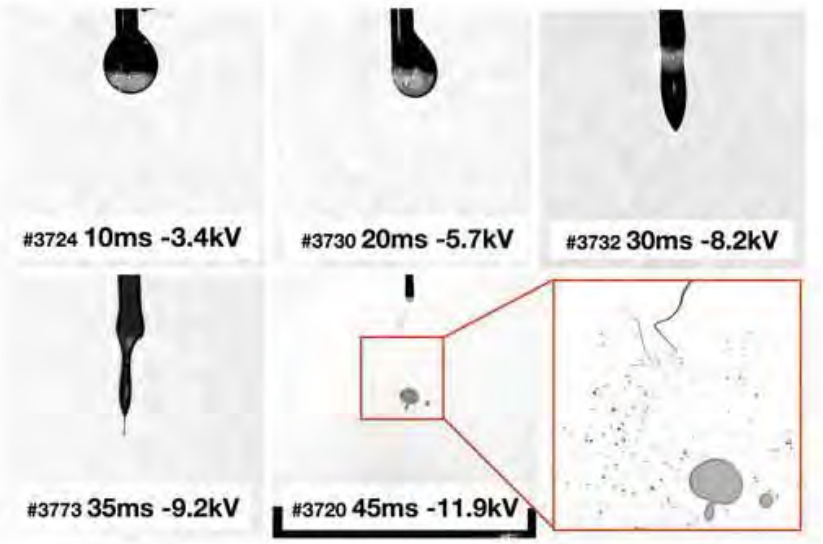

Fig. 2: Generation processes of fined droplets indicated from shadowgraph measurements

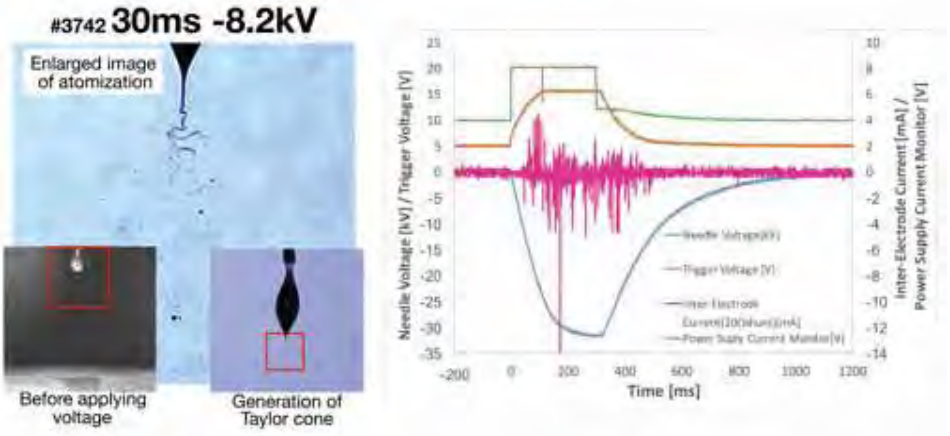

Fig. 3: sub-μm size droplets generation and its current waveforms

3. Results and discussion

Generation processes of fined droplets were indicated with the shadowgraph measurements in Fig. **??**. Those images were recorded in different targets (similar volume of droplets) and different pulsed voltages. From 10 to 20 [ms], droplets began to deform its outer shapes after applying IHV. Around 30 [ms], Coulomb force acting to charges in the droplet became larger. Because charges locating at lower bottom of the droplet responded more than the other part, the outer shape changed to three-dimensional sharp cone. This structure is called as "Taylor cone". In the 35 [ms], because the repelling force exceeds the surface tension with this IHV, small-size droplets in combination with large amount of charges were ejected from the tip end of Taylor cone. In the 45 ms, a number of atomized droplets distributed around elongated Taylor cone. As the result of Taylor cone, thin elongated liquid column could have disrupted into small sections in accordance with the wavelength of fluid-dynamical instabilities (for example, Kelvin-Helmholtz instability or Rayleigh-Taylor instability). This process of generation of small droplets indicates IHVA.

Detailed behavior of tip area of the Taylor cone is shown in left part of Fig. 3. When the fluid-dynamical instability occurred in the elongated Taylor cone, a spiral structure was observed some times. Shape of smaller size droplets were dubious because the size of them should be under resolution capability of the shadowgraph method with visible light. This means size of them may be sub-μm. Fig. 3 indicates the voltage waveform applied to the droplet, current waveform of charges which reached at the counter electrode, input voltage, and output current monitor signal in this shot. Impulsed voltage having 200 ms rise-time, 32 kV peak amplitude

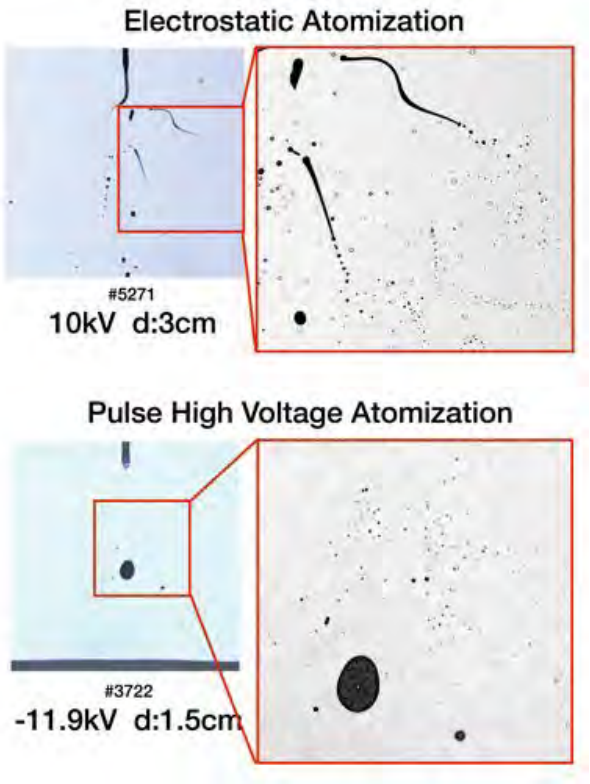

Fig. 4: difference between atomization dynamics

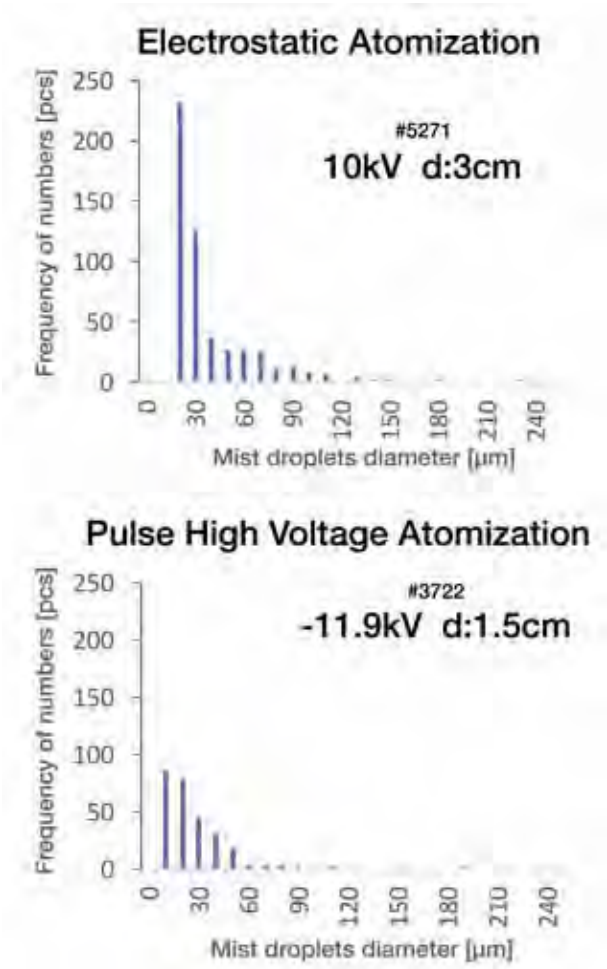

Fig. 5: histograms of both type of atomization

was achieved. Although negative power supply was used in this experiment, current waveform carried by atomized droplets showed bipolar signals in accordance with pulse width of input voltage. This may mean ion generation of air molecules.

Fig. 4 shows comparison between spatial distribution of droplets under EA and IHVA. Fig.5 shows histograms of droplet diameter with respect to each size category indicated in Fig. 4. In the EA, applied voltage was 10 kV, electrode interval was 3 cm. In the IHV, instantaneous applied voltage at the timing of the image was -11.9 kV, electrode interval was 1.5 cm. IHVA process can generate more number of smaller size droplets (approximately 10 μm) and less number of middle size droplets (approximately from 60 to 110 μm) compared with the EA. Application of impulsed voltage into uncharged droplets can cause reflection of voltage wave at the end of a distributed parameter circuit. Superimposed voltage as the result of the wave reflection may produce instantaneous surge current.

4. Conclusion

Small droplets generation in IHVA was compared to that in EA. IHVA can generate more number of smaller size droplets and less number of middle size droplets.

References

[1] Smith D. P., IEEE Trans. Ind. Appl., Vol. IA-22, No. 3, pp 527-535, (1986).

[2] Kebarle P. and Tang L., Anal. Chem., Vol. 65. No. 22, pp 972-986, (1993).

[3] Okuda H. and Kelly A. J., Phys. Plasmas, Vol. 3. No. 5, pp 2191-2196, (1996).

[4] Hartman R. P. A. *et al.*, J. Aerozol Sci., Vol. 31. No. 1, pp 65-95, (2000).

[5] Obata D. *et al.*, J. Electrostatics, Vol. 76, 274-277, (2015).

Measurement of Population of Viable and Dead Cells on Inactivation of Bacillus Subtilis in Water by Pulsed Power Injection

Shouta Sato[1], Kouichi Kanai[1], Satoshi Takesono[2], and Go Imada[1,*]

[1] *Department of Information & Electronics Engineering, Niigata Institute of Technology, Japan*

[2] *Department of Environmental Science, Niigata Institute of Technology, Japan*

ABSTRACT

Inactivation of bacteria in water is experimentally proved in pulsed power method. A large number of micro bubbles are successfully produced by applying the pulsed power (4 kV, 250 A, 3.4 μs) to the water. Shock waves generated by collapse of the bubbles and/or instantaneous heating of the water due to the pulsed power injection may inactivate the bacteria. Bacillus subtilis as bacteria are discharged into the water in a water vessel. We found that 34 %, 90 % and 97 % of the bacteria are inactivated by firing 10, 50 and 100 shots of the pulsed power injection, respectively. The gross energy efficiency for inactivation reaches $(0.6\sim8.8)\times10^{12}$ cells a kWh.

Keyword

Pulsed power, Bacteria, Inactivation, Ballast water, Micro bubble

1. Introduction

Ballast water is necessary to stabilize ship's hulls during navigation. The total amount of ballast water reaches 3 to 5 billion tons a year, which is transferred internationally. Japan exports approximately 0.3 billion tons of the ballast water a year and imports 0.017 billion. The ballast water includes bacteria, microbes, spawn and larvae of marine organisms, which are undesirably discharged at a port of call. To prevent the migration of these organisms and conserve the marine environment, a international convention for the control and management of ships ballast water and sediments was adopted by the International Maritime Organization in 2004 [1]. It obligates the ships to manage their ballast water by using devices not later than 2006. Many methods for treatment of the ballast water have been studied; such as chemical, heat, sonic, magnetic, biological, radioactive and electrical treatments [2-6], however, more methods and techniques are required to develop the feasible devices.

In this study, we propose a new technique on the inactivation of the bacteria in the ballast water, which uses pulsed-power method [7,8]. Micro bubbles are produced by applying the pulsed power to the water. Shock waves generated by collapse of the bubbles and/or by instantaneous heating of the water between the pulsed-power electrodes, and radicals produced by the electric discharge may affect the life of the bacteria. The purpose of this study is to investigate the properties of inactivation of the bacteria.

2. Experimental setup

Figure 1 shows the experimental setup. It consists of a pulsed power supply, a rotary gap switch and a water vessel with electrode. The pulse forming network, PFN (4000 pF−10 μH × 8 stages, stored energy: 3.6 J), in the pulsed power supply generates a rectangular-shaped pulsed power with 13 kV, 260 A and 4 μs into short-circuited load (see Fig. 2). This pulse is applied to the electrode through the rotary gap switch, where the pulse repetition rate is 0.33 pps (pulse per second). The water vessel is made of clear acrylic resin with the inner dimensions of $40\times40\times40$ mm^3 and is filled with sterile purified

* imada@iee.niit.ac.jp

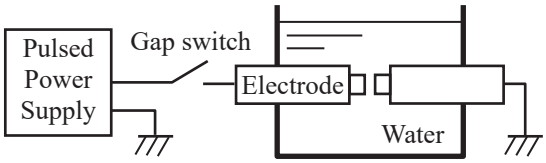

Fig. 1. Experimental setup.

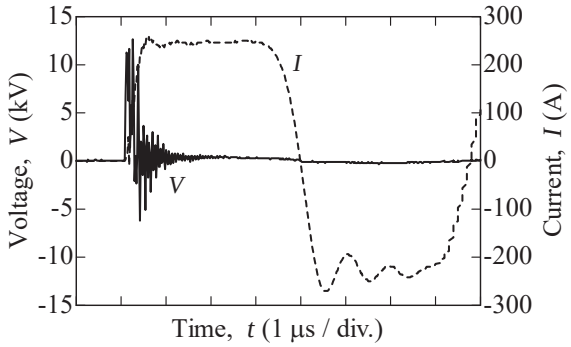

Fig. 2. Typical voltage and current of pulsed power supply into short-circuited load.

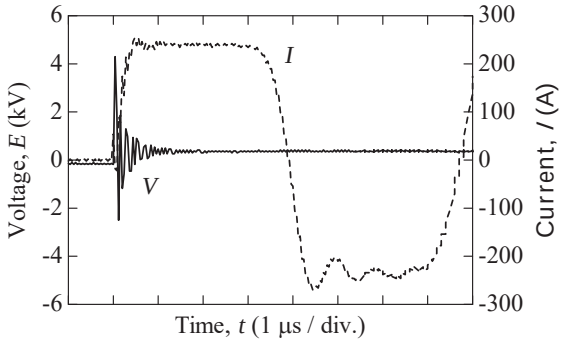

Fig. 3. Typical voltage and current at electrode in treatment.

water (48 ml, 24.5 °C, 4.1 μS/cm). The electrode, made of copper or stainless steel covered with polyethylene- resin pipe, is located at 15 mm above the bottom of the vessel. Its gap diameter and distance are 2.4 and 0.6 mm, respectively. The water temperature rises to 25.0 °C after 100 shots of the pulsed power injection.

Bacillus subtilis (ATCC 21332) are discharge into the water as bacteria. Bacillus subtilis cell is rod-shaped bacteria, and is found in soil, air and vegetation. It can live in stress situations such as acidic, alkaline, osmotic or oxidative conditions, and heat or ethanol. In this study, the population of bacteria cell is counted by using two methods. The viable cell is observed from a culture method with

(a) Immediately after pulsed power injection

(b) Just before second pulse of pulsed power injection

Fig. 4. Production and expansion of bubbles by pulsed power injection into water.

LB agar medium. The viable and dead cells are observed simultaneously from a fluorescent staining method, where a rapid microbial testing system (Bioplorer KB-VKH01, KOYO SANGYO Co. Ltd.) is used [9]. 4', 6'-diamidino-2-phenylindole is a nonionic dye used as a reagent. It can make both viable and dead cells fluorescent. Propidium iodide is also used as an ionic dye. It can detect only dead cell.

3. Results and Discussion

3.1 Properties of pulsed power

Figure 3 shows the voltage and current at the electrode in the water. The pulsed power of 4 kV in voltage, 250 A in current and 3.4 μs (FWHM) in pulse width of the current is applied to the water. It is found from Fig. 3 that the plateau of voltage (~300 V) is confirmed, where the power and the injected

energy into the water at the period of the first positive current pulse are estimated to be 75 kW and 0.255 J (7×10^{-8} kWh), respectively. Approximate 7 % of the stored energy of the capacitor in the PFN is deposited into the water during the first positive pulse.

3.2 Bubble production by pulsed power injection into water

Figure 4 shows the photographs of the bubbles produced by the pulsed power injection into the water. It is taken immediately after the pulsed power injection and just before the second pulse of pulsed power injection with the exposure time of 40 ms. Here, the time interval between the first and second pulse is 3 s. The expansion of bubbles into the water is seen as white fog in the water. The diameter of the bubbles is found to be around 50 μm [8]. The number density of bubble is estimated to be 10-20 bubbles / mm^2. The extent area of bubbles in the water is also estimated to be 300-500 mm^2. It is found from Fig. 4(b) that the babbles are widespread into the water just before the second pulsed power injection. We also found form Fig. 4(a) that the water surface undulates due to the shock wave generated by the instantaneous heating of water between the electrodes.

3.3 Inactivation of bacteria

a. Viable cell

Figure 5 shows the population of viable cell observed from the culture method. Since the water vessel is filled with the water of 48 ml, $(3\sim13)\times10^7$ CFU (Colony Forming Unit) of viable cells are discharged into the water. The pulsed power is continuously injected with 3 s in the time interval. The results of control experiment are also mentioned in Fig. 5(c), where the experiments are conducted without the pulsed power injection at room temperature. The viable cells are slightly inactivated or proliferate in the control experiment within 150 s which corresponds to a time for 50 shots of the pulsed power injection. Although some cells are inactivated within 300 s (correspond to 100 shots), some cells proliferate in the sterile purified water. We found from Fig. 5(b) that the population of viable cell decreases as increase the total number of pulsed power injection. At 50 and 100 shots of the pulsed power injection, in comparison to the results of the control experiment, Bacillus subtilis is successfully

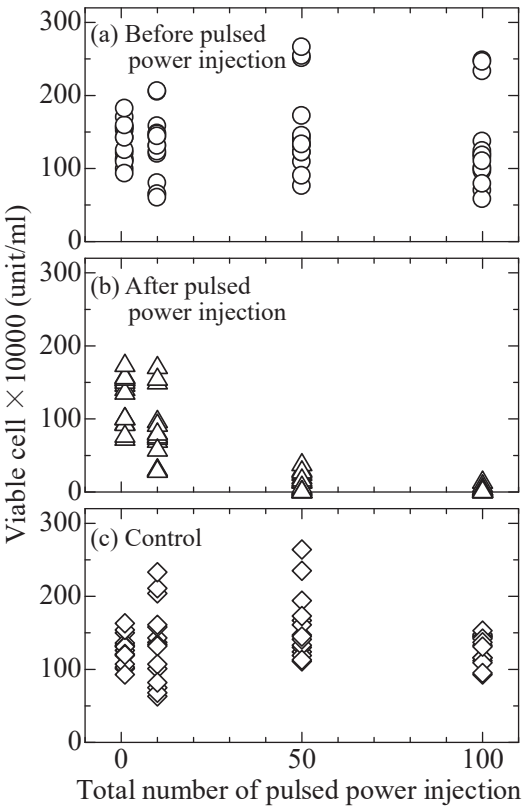

Fig. 5. Number of viable cell as a function of total number of pulsed power injection observed from culture method with LB agar medium.

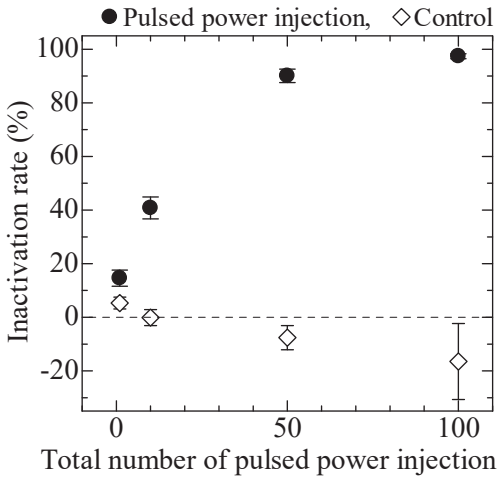

Fig. 6. Inactivation rate of Bacillus subtilis as a function of total number of pulsed power injection. Here, error bar indicates standard error of mean.

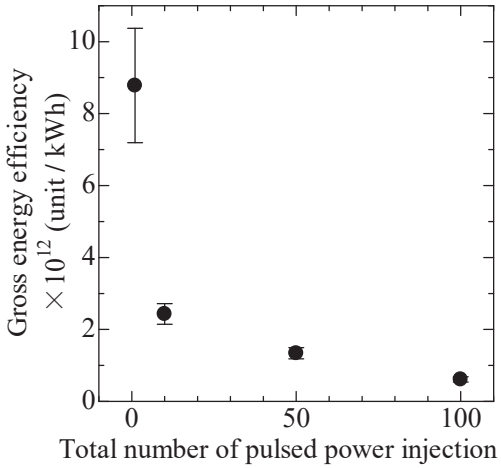

Fig. 7. Gross energy efficiency for inactivation of Bacillus subtilis as a function of total number of pulsed power injection. Here, error bar indicates standard error of mean.

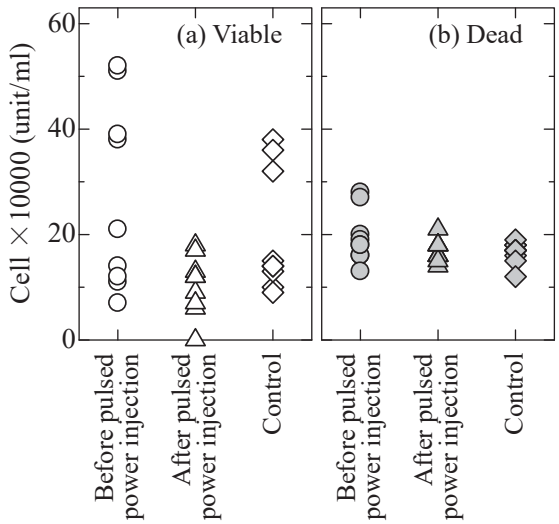

Fig. 8. Number of cell in pulsed power inactivation. Here, 800 shots of pulsed power is injected.

inactivated.

Figure 6 shows the inactivation rate of Bacillus subtilis as a function of total number of pulsed power injection into the water. The inactivation rate η is defined as

$$\eta = \frac{N_1 - N_0}{N_0}, \qquad (1)$$

where N_0 and N_1 are the population of viable cell before and after the pulsed power injection, respectively. The inactivation rates on the control experiment are also mentioned, where the negative value indicates the proliferation of bacteria. The inactivation rate rises as increase the total number of pulsed power injection. We found that 41 %, 90 % and 97 % of the bacteria are successfully inactivated by firing 10, 50 and 100 shots of the pulsed power injection, respectively. Since the proliferation of bacteria is confirmed in the control experiment, at 100 shots of the pulsed power injection, not only the discharged cells but also the proliferative cells are inactivated.

Figure 7 shows the gross energy efficiency for inactivation as a function of total number of pulsed power injection into the water. The gross energy efficiency β is defined as

$$\beta = \frac{N_1 - N_0}{n\varepsilon} \times v_{\mathrm{w}}, \qquad (2)$$

where n is the total number of pulsed power injection, ε is the stored energy at the capacitor of PFN, v_{w} is the volume of water in the vessel. Here, β includes the electric properties of the power supply, circuit and electrodes. Since almost all the cells are instantly inactivated by the pulsed power injection and then the population of viable cell decreases rapidly, the efficiency declines dramatically as increase the total number of pulsed power injection. The efficiency reaches $(0.6\sim8.8)\times10^{12}$ cells a kWh. In the regulation of the convention on ballast water management, the population of Escherichia coli in discharged ballast water should be controlled less than 250 CFU per 100 milliliters [1]. Assuming that a population of bacteria in seawater is of the order of 10^5 cells/ml [10], the electrical energy to treat 1-m^3 ballast water is estimated to be 0.01~0.17 kWh.

b. Viable and dead cells

Figure 8 shows the population of viable and dead cells observed from the fluorescent staining method. Here, $(1\sim5)\times10^6$ CFU of viable cells are discharged into the water. The pulsed power is continuously injected with 3 s in the time interval, and then the 800 shots of the pulsed power is injected into the water. The experiments are conducted at room temperature. The results of control experiment are also mentioned, where the experiments are conducted without the pulsed power injection at room temperature in retention time of 2400 s. We found that the viable cell is inactivated by the pulsed power injection similarly to the results observed

from the culture method. Since the discharged cell is few in number, many number of the pulsed power injection is necessary to inactivate the bacteria. We also found that the inactivation rate and energy efficiency are estimated to be low in comparison with those obtained from the culture method. After the pulsed power injection, on the other hand, the dead cell does not increase in number. The reliability of the fluorescent staining method for the dead cell is under consideration.

4. Conclusions

A large number of bubbles are produced by the pulsed power injection into the water. The inactivation of Bacillus subtilis is successfully demonstrated by the pulsed power injection into the water with a small amount of electric energy. The gross energy efficiency for inactivation reaches $(0.1\sim1.8)\times10^{11}$ cells a kWh.

Elucidation of the inactivation mechanism of the bacteria and the practical experiment are the subject for a future study.

Acknowledgement

The authors would like to thank R. Baba, Y. Hatano and T. Hasegawa of Niigata Institute of Technology for their help in the culture and the measurement of the bacteria.

This work was partly supported by JSPS KAKENHI Grant Number 26289079 and The Uchida Energy Science Promotion Foundation.

References

[1] GEF, UNDP and IMO, “GloBallast”, http://archive.iwlearn.net/globallast.imo.org/index.html (2017).

[2] M. Takahashi, K. Chiba and P. Li : “Free-Radical Generation from Collapsing Microbubbles in the Absence of a Dynamic Stimulus”, *J. Phys. Chem. B*, Vol. 111, pp. 1343-1347 (2007).

[3] S. Sawant, A. Anil, V. Krishnamurthy, C. Gaonkar, J. Kolwalker, L. Khandeparker, D. Desai, A. Mahulkar, V. Rande and A. Pandit : “Effect of Hydrodynamic Cavitation on Zooplankton: A Tool for Disinfection”, *Biochem. Eng. J.*, Vol. 42, pp. 320-328 (2008).

[4] T. Sakugawa, N. Aoki, H. Akiyama, K. Ishibashi, M. Watanabe, A. Kouda and K. Suematu : “A Method of Cyanobacteria Treatment Using Underwater Pulsed Streamer-Like Discharge”, *IEEE Trans. Plasma. Sci.*, Vol. 42, No. 3, pp. 794-798 (2014).

[5] K. Satoh, M. Onda, S. Sakai, and G. Imada: “Treatment of Zooplankton in Water by Pulsed Power − An Effect of $NaHCO_3$ Additive for Micro Bubble Production −”, *NIFS-PROC-90*, pp. 88-92 (2012).

[6] K. Shoji, K. Takahashi, T. Sasaki, T. Kikuchi, Nob. Harada and G. Imada: “Hatchability of Zooplankton Egg in Water after Irradiation with Pulsed Intense Relativistic Electron Beam”, *IEEJ Trans. Electric. & Electron. Eng.*, Vol. 12, No. S2, pp. S127-S128 (2017).

[7] I. V. Lisitsyn et al., "Streamer Discharge Reactor for Water Treatment by Pulsed Power", *Rev. Sci. Instrum.*, Vol. 70, No. 8, pp.3457-3462 (1999).

[8] G. Imada: “Generation of Micro Bubbles by Injection of Pulsed Power into Water and It's Application to Inactivation of Zooplankton”, *IEEJ Trans. Fundamentals & Materials*, Vol. 135-A, No. 6, pp. 334-340 (2015). (in Japanese)

[9] T. Shimakita, Y. Tashiro, A. Katsuya, M. Saito and H. Matuoka: “Rapid Separation and Counting of Viable Microbial Cells in Food by Nonculture Method with Bioplorer, a Focusing-Free Microscopic Apparatus with a Novel Cell Separation Unit”, *J. Food Protection*, Vol. 69, No. 1, pp. 170-176 (2006).

[10] K. Hamasaki, A. Taniguchi, Y. Tada, R. A. Long and F. Azam: “Actively Growing Bacteria in the Inland Sea of Japan, Identified by Combined Bromodeoxyuridine Immunocapture and Denaturing Gradient Gel Electrophoresis”, *Appl. Environ. Microbiol.*, Vol. 73, No. 9, pp. 2787-2798 (2007).

Dose dependence on inactivation of aquatic microorganism egg in water irradiated by pulsed intense relativistic electron beam

Naofumi Takeshita, Kazumasa Takahashi*, Toru Sasaki*, Takashi Kikuchi, and Go Imada**,***

Department of Nuclear System Safety Engineering, Nagaoka University of Technology

Department of Electrical, Electronics and Information Engineering, Nagaoka University of Technology

**Department of Information and Electronics Engineering, Niigata Institute of Technology*

***Extreme Energy Density Research Institute, Nagaoka University of Technology*

ABSTRACT Hatchability of *Artemia Salina* egg in water was investigated with irradiation of pulsed intense relativistic electron beams (PIREBs). An electron induction accelerator "ETIGO-III" was used as the PIREB generator. The irradiation results indicated that the hatchability of the eggs was decreased with the increase of the irradiation dose. Also the hatchability of the eggs in the water was reduced in comparison to one in the air with the PIREB irradiation.

Keywords

Zooplankton egg, Pulsed intense relativistic electron beam (PIREB), Hatchability

1 Introduction

Pulsed intense relativistic electron beams (PIREBs) were applied to a technology for environmental conservation, such as decrease of NOx concentration [1], reduction of volatile organic compounds contained in soil [2], and decomposition of congo red in water [3]. The PIREB has potential for various treatments due to electrons with higher kinetic energy, bremsstrahlung X-ray and radicals generated from the PIREB. It is considered that the PIREB has the advantage for brief treatments in comparison with a DC electron beam, because the beam current is of the order of kA with a short pulse duration.

The aquatic conservation is a pressing problem, recently [4]. Influence on aquatic ecosystems by microorganisms of alien species has been reported throughout the world [4]. The treatment of the aquatic microorganisms is a crucial issue to preserve the industry and the human health.

In our previous study, inactivation of zooplankton (*Artemia Salina*) by the PIREB irradiation has been reported [5]. Also, the hatchability of the eggs placed in the air by the PIREB irradiation has been investigated [6, 7]. In the water, the radiolysis products, such as OH radicals and aqueous electrons, are also one of main factors to inactivate the zooplanktons.

The purpose of this study is to investigate the dependence of the irradiation dose to the hatchability of the zooplankton (*Artemia Salina*) eggs. Also, the influence of the indirect effect to the eggs is studied in comparison with the various irradiation conditions.

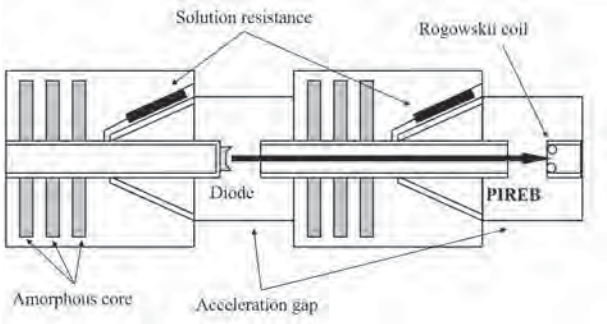

Figure 1: Experimental apparatus for PIREB generation using electron linear induction accelerator "ETIGO-III".

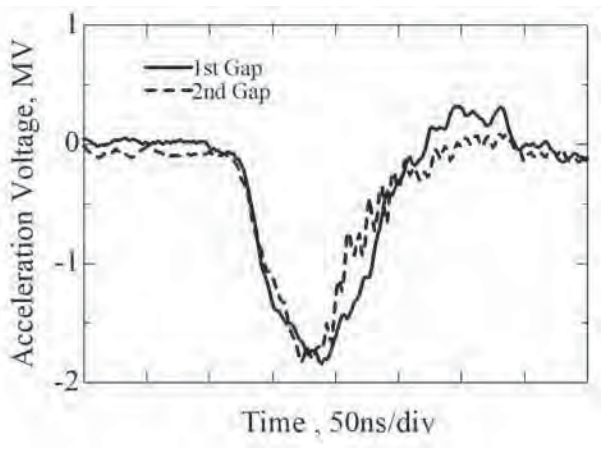

Figure 2: Typical acceleration voltage waveforms of PIREB at each acceleration cell.

2 Experimental Setup

We used two acceleration cells of the PIREB generator "ETIGO-III" (Extreme Energy Density Research Institute, Nagaoka University of Technology), which is an electron linear induction accelerator [8]. Figure 1 shows the experimental apparatus of PIREB generation. A field-emission foilless diode generates an electron beam with a hollow shape. Electrons emitted from a cathode ring of diode are accelerated by applied voltages in the 1st (diode) and the 2nd gaps. The maximum applied voltage is -2 MV at each gap in a vacuum. The electrons are extracted to the outside of a vacuum chamber as PIREB.

The voltage waveforms were measured by solution resistors, and the beam current was detected by a Rogowski coil, as shown in Fig. 1. Figures 2 and 3 show the typical waveforms of the applied voltage and the beam current in this apparatus. The accumulated voltage corresponds to the maximum extraction voltage (1.8 MV for the diode and 1.8 MV for the 2nd gap as shown in Fig. 2), and the maximum kinetic energy of PIREB reaches up to 3.6 MeV in this case. As shown in Fig. 3, the PIREB with a peak current of -2.4 kA in 70 ns (FWHM) was extracted to the air space after passing through a Ti foil.

Figure 4 shows the PIREB irradiation experimental setup for the eggs of *Artemia Salina*. The eggs were placed at the depths of 5.0 mm and 7.5 mm in the penetration direction of PIREB from the surface of the Ti foil, and the radial positions were 30 mm from the center. The eggs were put on three positions at each depth, and were set

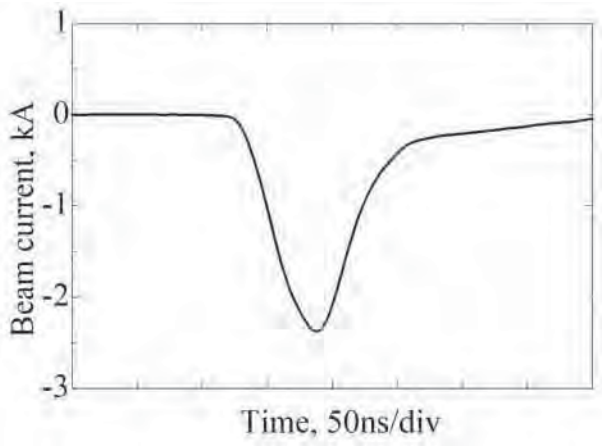

Figure 3: Typical waveform of PIREB current detected at Rogowski coil.

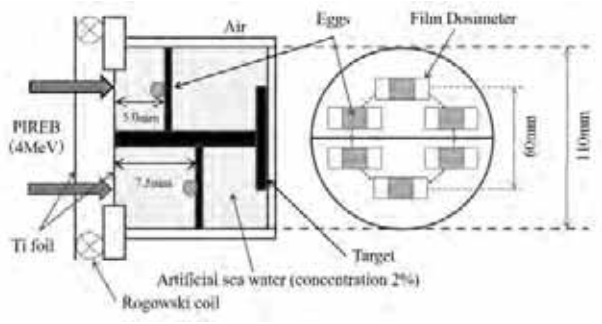

Figure 4: PIREB irradiation experimental setup for *Artemia Salina* egg in water.

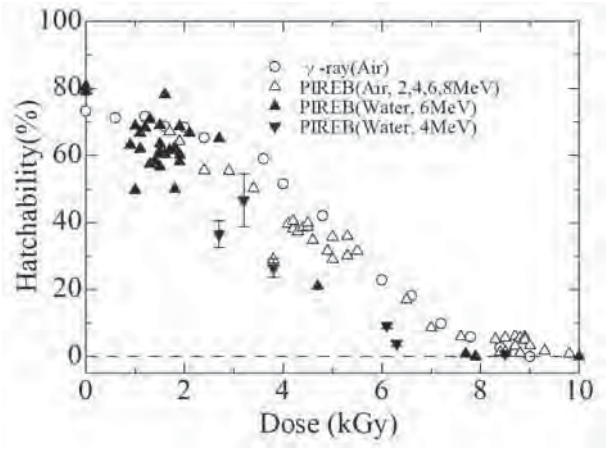

Figure 5: Hatchability of *Artemia Salina* egg with various experimental conditions for γ-ray irradiation in air [9] (open circle ○), PIREB irradiation in air [6, 7] (open triangle △), PIREB irradiation in water (full triangle ▲ [10] and full-inverted triangle ▼ for this experiment), respectively.

at about 100 at each position. The eggs were put into the artificial seawater after the PIREB irradiation.

The irradiation dose for the egg was controlled by the number of the irradiation shots of ETIGO-III and the depth of the egg in the water. Film dosimeters (FUJIFILM FTR-125) were placed behind the egg to simultaneously measure the dose.

3 Experimental Result

Figure 5 shows the hatchabilities of the *Artemia Salina* eggs with various experimental conditions. The dose was detected by the film dosimeter in the PIREB irradiation experiments as shown in Fig. 4.

The hatchability of the eggs was decreased with the increase of the dose in all of the cases. The hatchabilities for the γ-ray irradiation (open circle ○) [9] and the PIREB irradiation in the air (open triangle △) [6, 7] were almost same. The hatchabilities for the PIREB irradiation in the water (full triangle ▲ [10] and full-inverted triangle ▼ in this experiment) were lower than one for the irradiation in the air. It is considered that the indirect effect induced by the radical generation increased due to the interaction between the PIREB and the water for the irradiation results in the water.

4 Conclusion

In this study, the dose dependence of the inactivation of the zooplankton eggs was investigated with the irradiation of the PIREBs. The hatchability of *Artemia Salina* eggs in the water was studied in the various dose, and was compared to the case with the irradiation of γ-ray and the case for the PIREB irradiation in the air. The electron induction accelerator "ETIGO-III" was used as the PIREB generator.

The irradiation results indicated that the hatchability was decreased with the increase of the irradiation dose. The hatchability with the γ-ray irradiation was almost same as one with the PIREB irradiation in the air. On the other hand, the hatchability in the water was reduced in comparison to one in the air with the PIREB irradiation. It is considered that the indirect effect induced by the radical generation increased due to the interaction between the PIREB and the water.

References

[1] G. IMADA and K. YATSUI, *IEEE Trans. Plasma Sci.* 31, pp.295-296 (2003).

[2] G. IMADA, *IEEJ Trans. Elect. Electron. Eng.* 6, pp.88-90 (2011).

[3] T. KIKUCHI, H. MORIWAKI, H. NAKANISHI, H. KONDO, T. SASAKI, G. IMADA and Nob. HARADA, *Plasma Fusion Res.* 6, 1206021 (2011).

[4] GloBallast, http://globallast.imo.org (accessed on February 15, 2017).

[5] H. KONDO, H. TAKEHARA, T. KIKUCHI, T. SASAKI, G. IMADA and Nob. HARADA, *Plasma Fusion Res.* 5, 036 (2010).

[6] T. KAZETOH, K. TAKAHASHI, T. SASAKI, T. KIKUCHI, NOB. HARADA, and G. IMADA, *IEEJ Trans. FM* 135, pp.355-356 (2015).

[7] R. MYODO, K. SHOJI, H. SATAKE, K. TAKAHASHI, T. SASAKI, T. KIKUCHI, G. IMADA, AND NOB. HARADA, *4th International GIGAKU Conf. Nagaoka*, SP-15 (2015).

[8] A. TOKUCHI, N. NINOMIYA, K. YATSUI, G. IMADA, Q. ZHU, W. JIANG, and K. MASUGATA, *Proc. 12th Int'l Conf. High Power Particle Beams* 1, pp.175-178 (1998).

[9] T. IWASAKI, *J. Radiation Res.* 5-1, pp.69-75 (1964).

[10] K. SHOJI, K. TAKAHASHI, T. SASAKI, T. KIKUCHI, NOB. HARADA, and G. IMADA, *IEEJ Trans. Elect. Electron. Eng.* 12, pp.S127-S128 (2017).